



TECHNISCHE
UNIVERSITÄT
WIEN

DISSERTATION

Coupling in Quantum Solids: From Atoms Towards Molecules

ausgeführt zum Zwecke der Erlangung des akademischen Grades eines
Doktors der technischen Wissenschaften

unter der Leitung von

Univ.Prof. Dipl.-Ing. Dr.techn. Hannes-Jörg Schmiedmayer

eingereicht an der Technische Universität Wien
Fakultät für Physik

von

MSc. Andrew Niels Kanagin



Wien, May 2025

A.N. Kanagin

Gutachter:

H-J. Schmiedmayer

F. Jelezko

G. A. Briggs

*To my mother and father,
of course*

Abstract

Hybrid quantum systems provide a powerful framework for exploring quantum phenomena by leveraging the distinct advantages of their individual components. In this work, I demonstrate a novel hybrid platform that combines solid noble gas matrices doped with alkali atoms and superconducting resonators. These cryogenic solids, also known as quantum solids, serve as an inert, predominantly spin-free host environment, allowing for long coherence times of embedded spin impurities. Specifically, we use rubidium and sodium as dopants embedded in solid neon and parahydrogen, enabling addressable hyperfine transitions in the GHz regime that interact strongly with the superconducting resonator field.

We achieve strong coupling between the impurity ensemble (sodium) and the superconducting resonator, with a cooperativity of approximately 10—marking a key milestone in hybrid quantum architectures. Additionally, we characterize the coherence properties of the spin system, measuring a longitudinal relaxation time (T_1) of approximately 10 minutes. Hahn echo measurements yield a transverse relaxation time (T_2) of 0.93 ms, which extends to 1.38 ms using Carr-Purcell-Meiboom-Gill (CPMG) sequences. These results highlight the viability of noble gas solids as host materials for quantum systems and open new possibilities for engineered spin environments at millikelvin temperatures.

Beyond demonstrating strong coupling, this platform presents exciting opportunities for future research in quantum sensing, impurity-based quantum memories, and further exploration of novel dopant-host interactions. Notably, we also detect signatures of additional species interacting with our superconducting resonators, suggesting avenues for further investigation into unknown impurities and their effects in hybrid quantum systems. The combination of long-lived spin states with superconducting technology paves the way for new hybrid quantum devices, offering both fundamental insights and potential applications in quantum information science.

Zusammenfassung

Hybride Quantensysteme bieten einen leistungsstarken Rahmen zur Erforschung quantenmechanischer Phänomene, indem sie die individuellen Vorteile ihrer Komponenten kombinieren. In dieser Arbeit demonstrieren wir eine neuartige hybride Plattform, die aus festen Edelgasmatrizen mit dotierten Alkalimetallen und supraleitenden Resonatoren besteht. Diese kryogenen Festkörper, auch als Quantensolide bekannt, dienen als inertielle, überwiegend spinfreie Wirtsumgebung und ermöglichen lange Kohärenzzeiten der eingebetteten Spinverunreinigungen. Insbesondere verwenden wir Rubidium und Natrium als Dotierstoffe, die in festem Neon und Parawasserstoff (pH_2) eingebettet sind, wodurch adressierbare Hyperfeinübergänge im GHz-Bereich entstehen, die stark mit dem Feld des supraleitenden Resonators wechselwirken.

Wir erreichen das starke Kopplungsregime zwischen dem Ensemble der Verunreinigungen und dem supraleitenden Resonator mit einer Kooperativität von etwa 10 – ein wichtiger Meilenstein für hybride Quantensysteme. Darüber hinaus charakterisieren wir die Kohärenzeigenschaften des Spinsystems und messen eine longitudinale Relaxationszeit (T_1) von ungefähr 10 Minuten. Hahn-Echo-Messungen ergeben eine transversale Relaxationszeit (T_2) von etwa 0,93 ms, die mit Carr-Purcell-Meiboom-Gill (CPMG)-Sequenzen auf 1,38 ms verlängert werden kann. Diese Ergebnisse unterstreichen die Eignung von Edelgas-Festkörpern als Wirtsmaterialien für Quantensysteme und eröffnen neue Möglichkeiten für die Gestaltung von Spinumgebungen bei Millikelvin-Temperaturen.

Über die Demonstration der starken Kopplung hinaus bietet diese Plattform spannende Perspektiven für zukünftige Forschungen im Bereich der Quantensensorik, speicherbasierter Quantentechnologien und der weiteren Untersuchung neuartiger Dotierungs-Wirts-Interaktionen. Bemerkenswerterweise beobachten wir zudem Signaturen zusätzlicher Spezies, die mit unseren supraleitenden Resonatoren wechselwirken, was darauf hindeutet, dass unbekannte Verunreinigungen weiter untersucht werden sollten. Die Kombination langlebiger Spinzustände mit supraleitender Technologie ebnet den Weg für neue hybride Quantengeräte, die sowohl fundamentale Einblicke als auch potenzielle Anwendungen in der Quanteninformationswissenschaft ermöglichen.

Publications

Publications

Publications directly related to the thesis:

1. Kanagin, Andrew N., de Zordo, Nikolaus, Angerer, Andreas, Kersten, Wenzel, Lagos, Nikolaos, Redchenko, Elena S., Schmiedmayer, Jörg. (2024). "Impurities in cryogenic solids: a new platform for hybrid quantum systems." (In preparation).
2. Valenti, Francesco, Kanagin, Andrew N., Angerer, Andreas, Buimaga-Iarinca, Luiza, Morari, Cristian, Schmiedmayer, Jörg, Pop, Ioan M. (2024). "Hydrogen crystals reduce dissipation in superconducting resonators." *Physical Review B*, 109(5), 054503. DOI: 10.1103/PhysRevB.109.054503

Older Publications:

1. Upadhyay, Sunil, Kanagin, Andrew N., Hartzell, Chase, Christy, Tim, Arnott, W. Patrick, Momose, Takamasa, Patterson, David, Weinstein, Jonathan D. (2016). "Longitudinal Spin Relaxation of Optically Pumped Rubidium Atoms in Solid Parahydrogen." *Physical Review Letters*, 117(17), 175301. DOI: 10.1103/PhysRevLett.117.175301
2. Kanagin, Andrew, Regmi, Sameer, Pathak, Pawan, Weinstein, Jonathan. (2013). "Optical Pumping of Rubidium Atoms Frozen in Solid Argon." *Physical Review A*, 88(6), 063404. DOI: 10.1103/PhysRevA.88.063404

Publications not used in this thesis:

1. Kersten, W., de Zordo, N., Redchenko, E. S., Lagos, N., Kanagin, A. N., Angerer, A., Munro, W. J., Nemoto, K., Mazets, I. E., Schmiedmayer, J. (2024). "Self-induced superradiant masing." (Submitted).

2. Kersten, W., de Zordo, N., Diekmann, O., Reiter, T., Zens, M., Kanagin, A. N., Rotter, S., Schmiedmayer, J., Angerer, A. (2023). "Triggered superradiance and spin inversion storage in a hybrid quantum system." *Physical Review Letters*, 131, 043601. DOI: 10.1103/PhysRevLett.131.043601

Contents

1	Introduction	1
1.0.1	Thesis outline	3
2	Cryogenic Solids	5
2.1	Exploring the Parameters of Solid Materials	5
2.2	Bonding Energy Hierarchy	5
2.2.1	Type of bonds	6
2.3	Cryogenic gas solids	8
2.3.1	Lennard-Jones potential	8
2.4	Helium	10
2.5	Neon	11
2.6	Argon	11
2.7	Krypton	12
2.8	Xenon	12
2.9	Molecular hydrogen	13
2.9.1	Quantum solids	14
3	Impurities	17
3.1	Impurity Selection	17
3.1.1	Rubidium	17
3.1.2	Sodium	18
3.1.3	Hydrogen	18
3.1.4	Electrons	18
3.1.5	Impurity table	19
4	Cavity-QED	21
4.1	Photons in a cavity - Harmonic oscillators of a single mode	21
4.1.1	Light in a box	23

4.1.2	Quantized light-photons	25
4.2	Light-matter interaction	28
4.2.1	Jaynes-Cummings Hamiltonian	29
4.2.2	Tavis-Cummings Hamiltonian	32
4.2.3	Driven Tavis-Cummings Hamiltonian	33
4.2.4	Maxwell-Bloch Equations	35
4.2.5	Holstein-Primakoff approximation	36
5	Experimental Setup	39
5.1	Cryosystem	39
5.1.1	ADR	41
5.2	ADR modifications for the production of cryogenic crystals	41
5.2.1	Gas deposition setup	41
5.2.2	Additional modifications	44
5.2.3	Impurity upgrade	45
5.3	Optical setup modifications	46
5.3.1	Inside cryostat	46
5.3.2	Outside of cryostat	47
5.4	Superconducting magnet setup	49
5.5	Microwave setup	50
5.5.1	Frequency domain microwave equipment	51
5.5.2	Time domain microwave setup	51
5.6	Superconducting chip	53
5.6.1	Quantization of the superconducting circuit	53
5.6.2	Input-output theory of a LC circuit	55
5.6.3	Spiral resonator design	56
5.6.4	Input output to a coupled system	60
6	Crystal growth and characterization	63
6.1	Preparation	63
6.2	Deposition	65
6.3	Optical characterization	67
7	Microwave Spectroscopy and Time Resolved Measurements	73
7.1	Thermal photon occupation in the cavity	74
7.2	Zeeman splitting in an external magnetic field	75
7.3	Spin population of the hyperfine levels	76

7.3.1	Spin population of ^{85}Rb and ^{87}Rb	76
7.3.2	Spin population of ^{23}Na	79
7.4	Coupling of spins to a resonator	79
7.4.1	Preparation	79
7.4.2	Coupling of rubidium	80
7.4.3	Broadening of the spin ensemble	83
7.4.4	Coupling of sodium	85
7.5	Na atomic linewidth	87
7.6	Longitudinal and spin relaxation	90
8	Cryocrystals and the superconducting interface	99
8.0.1	Experimental modifications	100
8.0.2	Experimental results	104
8.0.3	Theoretical model	107
9	Outlook	111
9.1	Realization of a new type of hybrid quantum system	111
9.2	Cryogenic system upgrade	112
9.3	Impurities	112
9.3.1	Atoms	112
9.3.2	Sensing and metrology	113
9.3.3	Polar Molecules	116
9.4	Concluding remarks	119
	Appendix A Appendix	121
	References	127
	Curriculum Vitae	137

Chapter 1

Introduction

The interaction of light with matter forms the backbone of quantum optics [1]. Atoms, molecules, and solid-state systems can absorb, emit, and scatter photons, leading to quantum phenomena such as spontaneous and stimulated emission, Rabi oscillations, and electromagnetically induced transparency. The ability to coherently control these interactions has enabled the development of quantum memories, optical quantum gates [2], and high-precision atomic clocks [3]. A particularly important regime is cavity quantum electrodynamics, where single or multiple atoms are strongly coupled to optical [4] or superconducting cavities [5, 6], enabling efficient photon-matter interactions crucial for quantum technologies such as quantum networks and quantum computing.

The pursuit of such practical quantum technologies has driven researchers to explore hybrid quantum systems—architectures that combine different physical platforms to leverage their unique advantages [7]. Among these, superconducting circuits have emerged as leading candidates for quantum computation and microwave quantum optics due to their strong nonlinearities, flexible design, and scalability [8, 9]. In parallel, spin systems have been investigated extensively for their long coherence times and potential as quantum memories [10, 11]. The integration of these two systems—coupling spins to superconducting resonators—offers a promising route toward robust quantum information processing and sensing applications.

Historically, hybrid quantum systems have been explored in various physical settings. Early experiments with spin ensembles, such as nitrogen-vacancy (NV) centers in diamond [12] and rare-earth ions in solids [13, 14], demonstrated the feasibility of coupling spin degrees of freedom to electromagnetic fields. The advent of superconducting resonators further enhanced this prospect by providing high-quality-factor cavities capable of mediating interactions between disparate quantum systems [15, 16]. Despite

significant progress, existing solid-state implementations suffer from inhomogeneous broadening and decoherence mechanisms that limit their effectiveness.

A promising approach to overcoming these limitations is embedding spin systems in cryogenic solid matrices, such as noble gas solids and molecular hydrogen. These hosts could provide exceptionally clean environments, minimizing interactions that degrade coherence while simultaneously providing a 'soft' matrix, effectively reducing the broadening caused by local lattice stress. For instance, both solid and liquid helium are known for their weak spin-lattice interactions and low dielectric loss [17], making it an ideal host candidates for quantum storage and coherent manipulation [18, 19]. However, integration of helium with superconducting resonators presents both technical and fundamental challenges.

The first systematic investigations with noble gas solids emerged in the 1950s and 1960s, primarily driven by chemists and spectroscopists interested in their inertness. Low-temperature matrices of noble gases were used as host environments to study isolated atoms and molecules in a highly controlled setting. This technique, known as matrix isolation spectroscopy, allowed researchers to investigate reaction dynamics[20, 21] and electronic transitions [22] with minimal environmental perturbations. For instance, noble gas matrices were instrumental in stabilizing otherwise highly reactive species [23], such as free radicals and transient molecular intermediates, enabling precise spectroscopic analysis.

In parallel to their use in chemistry, physicists recognized the potential of noble gas solids as pristine quantum environments. The transition from chemical applications to atomic, molecular, and optical physics began in the 1990s [24–26], as atomic physicists explored alternative methods to attain high densities of their preferred atoms, such as alkali atoms. With their low nuclear spin densities and weak spin-lattice interactions, these solids made them ideal candidates for preserving coherence in embedded electronic and nuclear spin states [27–29].

Superconducting circuit technologies play a crucial role in enhancing these hybrid quantum platforms. Operating in the GHz regime, superconducting resonators and qubits provide a high-coherence interface for coupling to embedded spins, enabling efficient quantum state manipulation and readout. Furthermore, there exists already a wide range of mature technologies in the GHz range, which helps reduce the experimental complexity.

This leads to the central goal of my thesis: to investigate whether superconducting resonators can efficiently couple to spin ensembles in noble gas matrices, leveraging the spins' favorable coherence properties and the practicality of superconducting resonators.

1.0.1 Thesis outline

My thesis details the progression of my work, which initially began with coupling rubidium in solid hydrogen to superconducting resonators. This host-impurity system was chosen based on promising optical results which I performed in the group of J. Weinstein while completing my undergraduate and masters research in Reno, Nevada. However, I eventually transitioned from solid hydrogen to neon as a host matrix and, toward the final part of this thesis, to sodium as an impurity. Ultimately, I reached the strong coupling regime with sodium in neon, and begin characterizing their coherence properties.

I begin by providing a basic understanding of cryogenic solids, as their properties are not common. Additionally, I provide both old and current experiments which use them as host. This is followed by an introduction to the impurities I explored, as well as other systems that served as the basis for our experiment. I then lay out the theoretical framework for cavity quantum electrodynamics and extend it to the specific context of our experiment. Afterwards, I detail the experimental setup and modifications, providing sufficient information to highlight both the simplicity and modularity of the experiment we designed. Finally, I present the achievement of strong coupling between alkali atoms and a superconducting resonator, along with detailed measurements of the atomic ensemble's coherence properties. Ending the thesis will be an optimistic outlook for future experiments!

Chapter 2

Cryogenic Solids

2.1 Exploring the Parameters of Solid Materials

The experiment I describe here investigates the manipulation of spin impurities within a solid host material, an area that has become a particularly great platform for exploring a wide range of physical phenomena. Central to these studies is the relationship between the impurity or vacancy and the host crystal. Factors such as mechanical stress [30, 31] and or magnetic noise from nuclear spins [32, 33] can introduce unwanted perturbations to the impurity. While some studies have attempted to transform these 'bugs into features'—as in the case of tin vacancies in diamond [34]—it's generally preferable to minimize host-impurity interactions. Here, I introduce an uncommon material designed to reduce both the magnetic noise from unwanted nuclear spins as well as the local stress from the host matrix. This host material is known as a *cryogenic solids*. As these kinds of solids are somewhat atypical, a brief introduction into the types of allowed bonds and what makes them special is advantageous at this point.

2.2 Bonding Energy Hierarchy

To understand how I aim to reduce local stress from the host matrix, it is essential to first examine how solids form and the types of chemical bonds that govern their structure. In most cases, these bonds fall into four primary categories: covalent, ionic, metallic, and van der Waals. These interactions determine molecular formation, crystal structures, and key properties such as electrical and magnetic behavior. At the core of these interactions lies the concept of binding energy, which describes the strength of

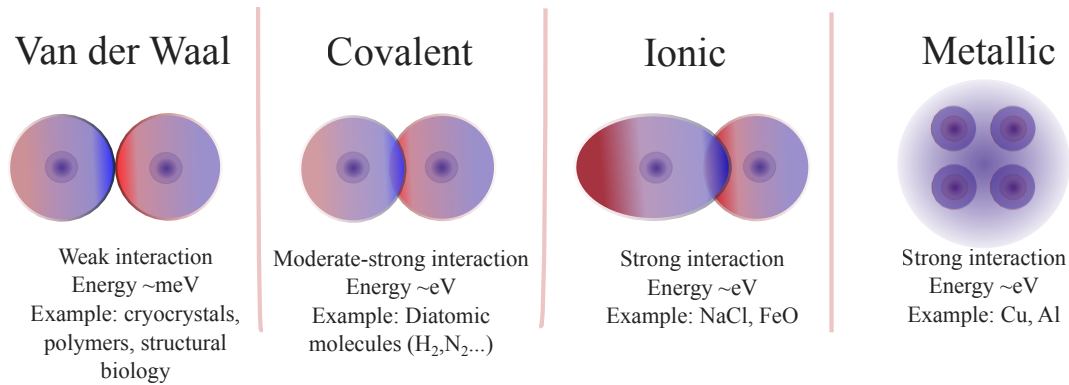


Figure 2.1 Different types of bonds found in nature from weakest to strongest.

atomic and molecular bonds. By understanding binding energy and its role in different atomic arrangements, we gain insight into cryogenic solids and their unique advantages as materials.

2.2.1 Type of bonds

Covalent and ionic bonds are generally well understood, as they are primarily governed by the electronic structure of atoms and arise from electrostatic forces. In covalent bonds, valence electrons are shared between two atoms with roughly equal contribution from each [35]. A simple example is the bond between two hydrogen atoms, where both nuclei exert an equal influence on the shared electrons, as illustrated in Figure 2.1. The typical bonding energy for covalent interactions is on the order of a few electron volts (eV). In contrast to covalent bonds, ionic bonds form when one atom readily donates its electrons while another atom eagerly accepts them to complete its electronic shell. This results in a transfer of electrons rather than shared ownership, leading to the formation of oppositely charged ions that are held together by electrostatic attraction. A common example is sodium chloride (NaCl), where sodium donates an electron to chlorine, creating a stable ionic compound.

Metallic bonds differ significantly from both ionic and covalent bonds, as the bonding does not originate from the atoms' nuclei. In metallic bonds, the valence electrons are not bound to individual atoms but instead are considered "free" to move among all neighboring atoms, creating a delocalized electron cloud. This unique bonding behavior allows metallic materials to conduct electricity and heat efficiently. Within metallic bonds, there are two main types: simple metallic bonds and transition metallic bonds.

Simple metallic bonds involve the sharing of valence electrons from the s or p orbitals, while transition metals interact with their partially filled d shell electrons. The strength of metallic bonds can vary, with simple metallic bonds having lower binding energies (e.g., mercury, which melts at 234 K), though they generally fall within the range of 1 eV.

The final type of bond we will discuss in this section is the van der Waals bond, which is by far the weakest of the four. Unlike the previous three types, van der Waals bonds typically arise between atoms or molecules with completely filled valence shells, making them dependent on specific conditions to form. These bonds are driven by small, fluctuating displacements of electric charges within atoms, often referred to as "instantaneously induced dipole moments." The van der Waals bonds contrast sharply to metallic bonds in that they do not involve free-moving electrons but instead result from weak, transient interactions. The interaction can be understood through dispersion forces [36–38]. For instance, when a positively charged sphere is brought close to a metallic sphere, the total number of electric charges remains constant on each, but the electronic density undergoes a subtle change. This difference in charge density induces a small polarization on the surface, which rapidly diminishes in strength. Interestingly, Johannes D. van der Waals introduces this model in his PhD thesis in 1873 [39], and in 1910 received the Nobel prize in physics for his work involving gases and liquids [40].

The attractive component of the van der Waals bond scales as $\frac{1}{r^6}$, while covalent and ionic bonds scale with $\frac{1}{r^2}$ (Coulomb's law). As a result, van der Waals forces are typically three orders of magnitude weaker (~ 1 -10 meV) than covalent and ionic bonds. Interestingly, the van der Waals force is not always static; it can be dynamically induced when a permanent polar molecule rotates and creates an induced dipole. Such interactions are more common in polar molecules, which exhibit greater polarizability (larger dispersion), though they can also occur, to a lesser extent with atoms.

Naturally, one might expect that if the host material weakly interacts with itself, it would behave similarly towards impurities introduced into the system. In this case, the host matrix would essentially provide an inert (non-chemically bonded), weakly interacting (van der Waals) environment in which the impurity is trapped. The trapped impurity would, hopefully, retain most of its vacuum properties, albeit with slight perturbations due to the matrix. Furthermore, because of the weak interactions within the host matrix, local stresses exerted on the impurity by the matrix would be minimized. This reduction in stress is crucial because it helps mitigate one of the primary challenges associated with spins in solids.

It is with this type of bond that the foundation of this thesis will be built, as we plan on creating and using cryogenic gas crystals as a host matrix to hold atomic impurities, in hopes that such a weak bond will preserve their favorable atomic properties. As mentioned earlier, typical van der Waals interactions are on the order of 0.01 meV, which corresponds to a $k_{\text{B}}T$ temperature of approximately 100 K. This means we must get *cold*!

2.3 Cryogenic gas solids

Due to their filled valence shells, cryogenic gases (such as He, Ne, H₂, Ar, N₂, CO₂, and others) are generally considered inert and non-interacting, meaning they do not form electronic bonds under typical conditions unless stripped of their electrons. However, when exposed to extremely low temperatures or high pressures, these gases can transition into various phases, including molecules, solids, and liquids. Helium, in particular, exhibits even more remarkable behaviors; it can become a superfluid [41, 42] and even form a Bose-Einstein Condensate (BEC) when prepared under the right conditions, as demonstrated in studies by Alan Aspect and others [43].

These unique states of matter are a direct consequence of the van der Waals interactions discussed previously, which allow these gases to condense into more complex structures under the right conditions. In this context, the weak but significant forces that govern these transformations play a crucial role. The following subsections will lay the groundwork for modeling cryogenic gas crystals, covering important properties such as their melting points, crystal structures, isotopes, and spin characteristics. Additionally, we will explore the quantum properties that make these crystals especially intriguing, building on the foundation of van der Waals bonding introduced earlier.

2.3.1 Lennard-Jones potential

A common method for modeling the van der Waals force is through the Lennard-Jones potential, named after John Lennard-Jones who first published his theoretical model on intermolecular forces and molecular structures in 1929 [44]. It is a pair potential, involving only two particles, and has a simple behavior: particles repel each other when they are too close, attract each other at intermediate distances, and reduce to zero at larger distances. As a side note, it's funny that if you didn't know his last name, you might assume this model of two interacting particles came from two scientists. Ironically, it was just one.

The Lennard-Jones potential is written as

$$V(r) = 4\epsilon \left[\left(\frac{\sigma}{r} \right)^{12} - \left(\frac{\sigma}{r} \right)^6 \right] \quad (2.1)$$

where,

$V(r)$ = Intermolecular potential

ϵ = Binding energy between particles

σ = Particle equilibrium distance of zero net force

r = Separation distance

The first constant in this equation, ϵ , gives insight into the degree of polarizability of the particles, commonly referred to as the dispersion energy, and sets the depth of the potential well. The second constant, σ , describes the smallest distance two non-bonding particles can exist. From this equation, two types of interactions strengths follow: one on the order of $\frac{1}{r^{12}}$ which is a repulsive force, and its counter part, $-\frac{1}{r^6}$ which is an attractive force. The first term in the Lennard-Jones potential accounts for the Pauli exclusion principle and short-range Coulomb repulsion, preventing atoms and molecules from approaching too closely. As such, it becomes extremely strong at short distances but rapidly diminishes with increasing separation. While there is no theoretical justification for choosing the exponent 12, it provides a good empirical fit and is mathematically convenient. The second term, which can be derived via second order perturbation theory, is a multipole expansion of the Coulomb potential and results in an attractive potential. A pictorial representation can be seen in Figure 2.2 (A). With some basic mathematics, one can see that the minimum potential is located when $r = 2^{\frac{1}{6}}\sigma$, which also happens to be where $V(r) = -\epsilon$.

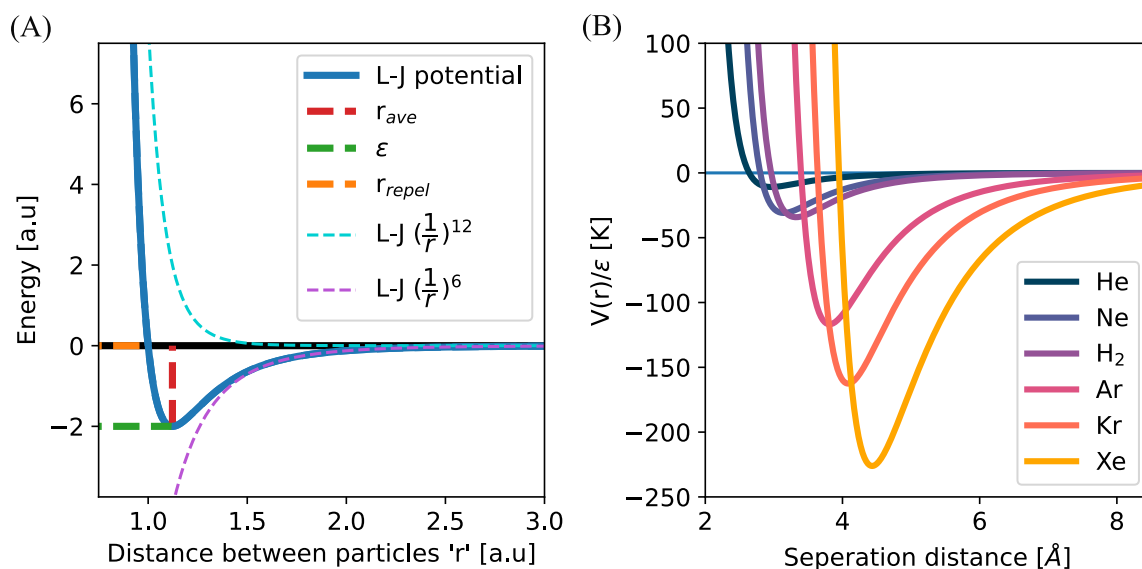


Figure 2.2 (A) Arbitrary Lennard-Jones potential with relevant parameters plotted. (B) Lennard-Jones potential for the noble gases as well as molecular hydrogen.

Equation 2.1 is commonly referred to as the 12-6 potential and other variations of this equation exist as well, however, this form is enough for our purposes. We can now look at the 12-6 potential for the noble gases as well as selected diatomic molecules which can be seen in Figure 2.2 (B). Additionally, a table with useful properties of the selected host matrix material is provided below.

2.4 Helium

Helium (He) is the second most abundant atom in the universe besides hydrogen, it is formed in the extreme temperatures of stars and can be used to cool objects down to near absolute zero, as it is the backbone of all modern cryogenic system — quite the remarkable atom. At first glance from Figure 2.2 (B), He appears to be the ideal host matrix as it has the weakest interaction of all of the species and has the possibility of isolating its zero nuclear spin isotope. The "unfortunate" drawback of using helium is that it requires large pressures to make a solid [45], as it does not freeze under any condition [45, 46]. Additionally, once in a solid it has been shown that diffusion of the impurities happens quickly, resulting in a net reduction of impurities due to clustering [26]. Let it be noted that though the impurities diffuse, the optical atomic linewidths are preserved and are the narrowest for the noble gas solids measured to date. Additionally, if one would like to transition the solid He between the BCC phase

to a HCP phase, they need only to change the pressure. Interestingly, He is still used as a weakly interacting host medium for molecular and atomic impurities; however, the He atoms are usually in clusters or droplets with 40-200 atoms and are sprayed into a vacuum together with the desired impurity. This technique effectively cools the impurities to below 1 K and allow scientists to perform spectroscopy in sub Kelvin temperatures [47].

2.5 Neon

Neon (Ne), located just below He on the periodic table, is not as "unique" in its properties. Unlike He, we do not need to worry about superfluidity or the need for increased pressure, which adds experimental complexity. In the simplest terms, Ne behaves more classically and exhibits the expected noble gas properties that persist down the periodic table.

Ne is a noble gas with two stable isotopes ^{20}Ne and ^{21}Ne , where ^{20}Ne zero nuclear spin and ^{21}Ne has spin of 1. The ratio of ^{20}Ne to ^{21}Ne is quite high, 99.8% and 0.02% respectively. The rather low abundance of ^{21}Ne happens to work in our favor, as one of our aims is to reduce the concentration unwanted nuclear spins in the host matrix. The concentration of ^{21}Ne could be further reduced by isotopic purification, and this can even purchased commercially. Ne has a relatively low melting point, which requires temperatures below 30 K to solidify and is easily done with current state-of-the-art cryostats. As a host matrix, Ne has shown the ability to preserve the atomic impurities of alkali atoms [48] as well as Yb [49], while essentially removing the ability for the impurities to diffuse. There have been successful experiments using optically addressed ensembles of embedded alkali atoms which exhibit long coherence times, as well as the ability to optically read out a single impurity [50–52]. Solid Ne has also been used in the same manner as He in creating a buffer for electrons coupled to superconducting circuits [53], as well as a medium for searching for physics beyond the standard model [54, 55]. The majority of this thesis project was done with solid Ne crystals.

2.6 Argon

After Ne in the periodic table is Argon (Ar), which, depending on the experiment has more favorable properties than neon. The bonding potential of Ar is much larger, resulting in a melting point of ~ 80 K. As experiments can get more complicated and require more equipment inside of a cryostat, having a "high" melting point can be

advantageous. This larger interaction potentially results in an increased interaction with the impurity, as the polarizability of Ar is higher than the previous noble gases. Similar to Ne, Ar has the possibility to obtain purified spin-zero nuclear spin isotopes (^{36}Ar , ^{38}Ar , and ^{40}Ar are spin-0) providing a host matrix with no additional nuclear spins. Historically, one of the first experiments which demonstrated the preservation of the atomic properties inside of the cryogenic solids was done using Ar. In the 1960's, Frank Pipkin and associates trapped rubidium (Rb) atoms in a solid Ar matrix and demonstrated that the Rb was able to absorb circularly polarized light [56, 57]. This was replicated and expanded on decades later using lasers [27]. Although Ar offers a potentially nuclear spin-free environment, other cryogenic gas solids have shown an increase in relaxation times and coherence times [26, 58]. This suggests that the host matrix itself is interacting more than the lighter noble gases. Currently, there are some promising experiments using Ar as a host matrix which aim to search for physics beyond the standard model [59].

2.7 Krypton

Despite krypton (Kr) sharing similar properties to other noble gases, such as low melting points, weak bonding potentials, and the possibility of having zero nuclear spin isotopes, it has not been as widely studied for use as a host matrix for atomic impurities. While its characteristics make it a suitable candidate for such applications, there has been relatively limited research exploring its potential in this context. However, recent studies have begun to investigate Kr as a host for impurities, indicating that it still holds promise for specific experimental setups despite the lack of extensive exploration [60, 61].

2.8 Xenon

Xenon (Xe) is another noble gas that plays an important role in cutting-edge experiments, particularly in the search for physics beyond the Standard Model. Xe has several stable isotopes, with ^{132}Xe being the most abundant, and it is often used in solid form for its unique properties in low-temperature physics and particle detection.

Xe's large atomic mass and relatively low ionization potential make it an attractive material for use in experiments requiring high sensitivity to individual atoms. One prominent example of Xe's utility is in the detection of individual barium (Ba) atoms for Ba tagging in experiments such as nEXO [62]. The ability to image and identify

individual Ba atoms deposited in solid Xe is crucial for the success of nEXO, which aims to detect neutrinoless double-beta decay—a key process in the search for physics beyond the Standard Model. These advancements in single-atom imaging were demonstrated in other studies, see References [62–64]

2.9 Molecular hydrogen

Similar to noble gases, diatomic molecules can also serve as inert matrix materials. The simplest example is molecular hydrogen (H_2), consisting of two hydrogen atoms. H_2 crystals have the weakest bonding potential among solid matrices (besides He), which results in the lowest solidification temperature of approximately 14 K. This weak interaction can be advantageous, as it minimizes the impact on impurities, as demonstrated in experiments comparing Ar [27] to H_2 [58], where the polarization lifetime of impurities was increased by over two orders of magnitude.

Due to the identical nature of the two hydrogen atoms, the molecule can exist in only two possible states: ortho- (o-H_2) and para-hydrogen (p-H_2), determined by the symmetry of the total molecular wavefunction [65]; p-H_2 , with nuclear spins in a singlet state, has no net nuclear spin ($I = 0$) and occupies the rotational ground state. At room temperature, the ortho-hydrogen state (with nuclear spin $I = 1$) predominates because it has three degenerate spin states (a triplet), giving it a higher statistical weight than the para-hydrogen singlet state ($I = 0$), making it thermodynamically favored. However, by employing a catalytic method, o-H_2 can be converted to p-H_2 at low temperatures, achieving purities greater than 99.9% [66]. This thesis will explore the use of molecular hydrogen matrices, particularly p-H_2 , for hosting atomic impurities as it gave the *"best"* results during my bachelors and masters research [58].

Species	Melting Point [K]	Spin 0 Isotopes	Crystal Structure	Lattice Constant [Å]
He	N/A	Yes	HCP BCC	2.64
p-H ₂	13.80	Yes	HCP FCC	3.78
Ne	24.56	Yes 0.2% non zero	FCC	3.16
Ar	83.81	Yes	FCC	3.77
Kr	115.78	Yes 20% non zero	FCC	5.59
Xe	161.36	Yes 40% non zero	HCP FCC	6.30

Table 2.1 Melting points, crystal structures, and lattice constants of various species.

2.9.1 Quantum solids

In addition to the relatively uncommon bonding mechanisms discussed earlier, cryogenic crystals also exhibit quantum phenomena, which is part of the reason they are sometimes referred to as *quantum solids*—a term I’ve chosen for my thesis title. But what exactly defines a quantum solid? Broadly speaking, it refers to a solid where the quantum effects of the constituent particles significantly influence its physical properties [67].

Classically, a crystal can be described as a periodic arrangement of atoms, with the atoms stationary at their lattice sites, which means they possess zero, or extremely small, kinetic energy in those positions. However, this classical picture does not fully hold, especially for atoms with low mass. A prime example of this is solid He. When He is compressed into a solid, the zero-point kinetic energy of a single atom becomes comparable to the lattice spacing. A pictorial representation can be seen in Figure 2.3 (A). In fact, to form a crystalline structure, He must be compressed to nearly 30 atmospheres, largely due to the uncertainty in atomic position caused by zero-point motion. This behavior stems from quantum mechanics, as, classically, one would expect atoms to become more localized as they are cooled and squeezed.

A rough explanation can be made through the Heisenberg uncertainty principle, where light atoms (small M) in the solid have an increased momentum uncertainty, $\Delta p \approx \hbar/\Delta x$, resulting in a large zero-point energy on the order of $E_{\text{zp}} \sim \hbar^2/M(\Delta x)^2$. This interplay between uncertainty in position and momentum is a hallmark of quantum behavior and plays a critical role in the properties of quantum solids. One can further

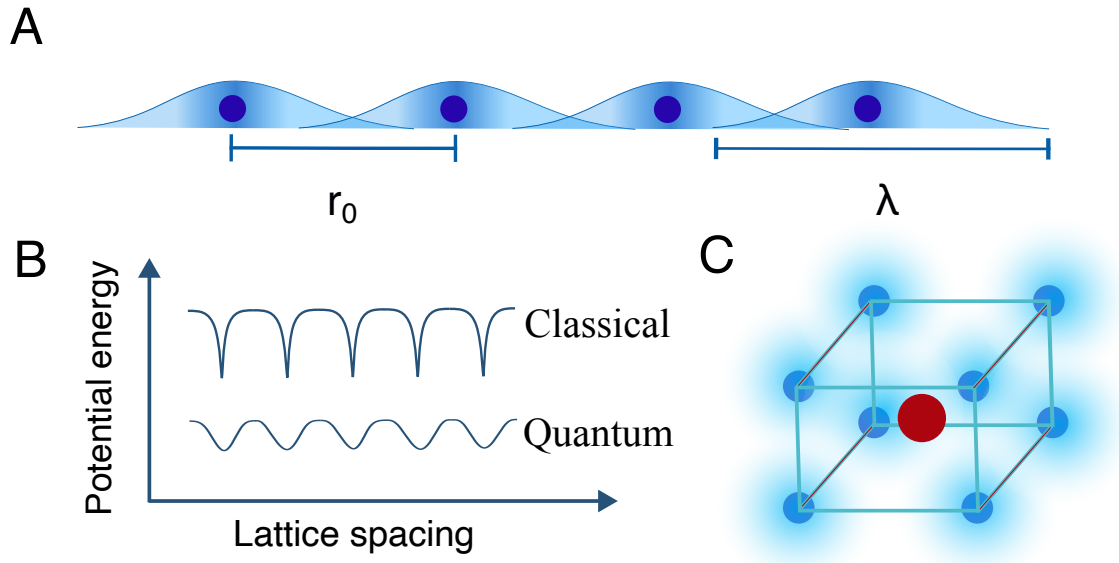


Figure 2.3 (A) Pictorial representation of the overlap of de Broglie wavelengths (λ) in a periodic structure. At such low temperatures and low masses, the quantum nature of wave-particle duality dominates. (B) Visual comparison between the potential energy of a "classical" crystal and a quantum crystals, where the classical potential has sharp, narrow, dips while its quantum counterpart offers a softened potential. (C) Mock crystal structure showing the spreading of the radial wavefunction of the host crystal and a centered impurity.

quantify the "quantumness" of these crystals via the *de Boer parameter*, which compares the zero-point kinetic energy to the depth of the interatomic potential well. Estimating the kinetic energy as $E_{\text{kin}} \sim \hbar^2/(2mr_0^2)$ and taking the potential energy scale to be ϵ , their ratio yields a dimensionless quantity $\Lambda^{*2} \sim \hbar^2/(2mr_0^2\epsilon)$, or equivalently,

$$\Lambda^* = \frac{\lambda(\epsilon)}{r_o} = \frac{\hbar}{r_o\sqrt{m\epsilon}} \quad (2.2)$$

where,

λ = de Broglie wavelength

r_o = classical interatomic distance

\hbar = Planck's constant

m = mass of the particle

ϵ = energy scale of the interaction

This parameter can be interpreted as the ratio between the particle's de Broglie wavelength and the interatomic spacing. As both the interaction energy ϵ and mass m decrease, Λ^* increases, indicating stronger quantum delocalization due to larger zero-point motion. Helium has the highest known value of $\Lambda^* \approx 0.4$, while the next noble gas, neon, has a much smaller value of approximately 0.08. Molecular solids such as p-H₂, N₂, and O₂ have values of approximately 0.27, 0.23, and 0.2, respectively. A more detailed analysis can be found in Reference [67]. I expect this phenomenon will create a "softer" environment than, for example, carbon, where the delocalization reduces the local stress on the impurity, as illustrated in Figure 2.3 (C).

Chapter 3

Impurities

3.1 Impurity Selection

As outlined in the introduction, our goal is to utilize a novel material that can host our spins, which ultimately couple to superconducting resonators. In the previous section, we introduced the concept of our host matrix, which consists of solidified cryogenic gases. I will do the same for the impurities in this chapter. The selection of impurities for these matrices was driven by practical considerations: they need to be relatively easy to introduce, as they would be produced within the cryostat, and they should also exhibit transitions in the GHz frequency range to couple to our superconducting resonators.

As an atomic physicist, my natural inclination is to consider alkali atoms, and, fortuitously, these turned out to be a good impurities of choice. In this section, I will introduce the two specific alkali impurities that we intentionally incorporated into the crystal. In addition, I will discuss two other impurities that have been potentially observed experimentally in our resonators. Interestingly, all of these impurities reside on the left side of the periodic table, whereas our host matrices are typically composed of elements from the right side—this contrast feels almost serendipitous, making it a beautiful aspect of my PhD thesis.

3.1.1 Rubidium

The first impurity introduced into our system was rubidium (Rb), an alkali metal widely used in atomic physics experiments over the last two decades. Whether in a Bose-Einstein condensate (BEC) or trapped in optical tweezers, Rb has played a pivotal role in advancing our understanding of quantum systems. With nice optically accessible

transitions and well-suited hyperfine transitions for microwave technologies [68], Rb was a natural choice for our first impurity. Moreover, Rb vapor is easily produced, as its melting point is around room temperature ($\sim 40^\circ\text{C}$). Both isotopes of Rb (^{85}Rb and ^{87}Rb) possess hyperfine transitions (3.0 GHz and 6.8 GHz, respectively) that can serve as two-level systems, ideal for coupling to our resonators. For more detailed information on atomic Rb, I recommend referring to Dan Steck's Alkali data [69, 70].

3.1.2 Sodium

The second impurity introduced into our system was atomic sodium (Na), a species that has been used frequently due to its characteristic orange D1/D2 transition lines, which are visible in street lamps. Na was also a contender in the race to create the first BEC, though Rb ultimately took the lead by just a few months. Na shares many similarities with Rb, including a low melting point and GHz-range hyperfine transitions. However, Na stands out as an alternative impurity due to fewer stable isotopes and a simpler hyperfine structure, which will be important later in the thesis. Similar to Rb, one can look up information on Na from Dan Steck's Alkali data [71].

3.1.3 Hydrogen

Hydrogen (H), the lightest and most abundant element, presents itself as a promising impurity choice. Its small atomic radius allows it to incorporate into lattices with minimal disturbance, making it less intrusive than heavier elements. Hydrogen exhibits a well-defined hyperfine transition at approximately 1.420 GHz [72], ideal for coherent manipulation in quantum systems. Similar transitions are observed in tritium (1.516 GHz [72]) and deuterium (0.327 GHz [72]), albeit to a lesser extent. While producing atomic H in controlled environments is challenging, it remains feasible. Moreover, its simple hyperfine structure allows for easy isolation of two levels under a magnetic field. Interestingly, preliminary measurements suggest a coupling to our resonators, indicating the presence of atomic hydrogen on or in our superconducting resonators, both with and without our crystals. This will be explained in Chapter 9.

3.1.4 Electrons

Electrons, as fundamental particles, present an interesting choice for integration as impurities. They are point-like with no substructure, enabling them to embed smoothly into various material systems without causing significant lattice strain. Electrons also

have a well-characterized magnetic moment, giving rise to hyperfine interactions and enabling electron spin resonance in the GHz regime, typically in the range of 9–10 GHz under typical magnetic fields. Moreover, the electron’s spin-1/2 nature simplifies the energy structure—splitting into just two distinct Zeeman levels in the presence of an external magnetic field. The purpose for introducing electrons as an impurity is similar to that of H, we believe we are seeing signatures of coupling to electrons with our resonators both with and without our crystals. This will be explained in Chapter 9.

3.1.5 Impurity table

Species	Melting Point [K]	Hyperfine Transitions [GHz]	Hyperfine Ground States ($F = I \pm \frac{1}{2}$)
H	–	1.42	0, 1
Li	453	0.228	$\frac{1}{2}, \frac{3}{2}$
^{39}K	336.5	0.461	1, 2
^{40}K	336.5	1.285	3, 4
^{41}K	336.5	0.254	1, 2
Na	370.7	1.771	1, 2
^{85}Rb	312.3	3.035	2, 3
^{87}Rb	312.3	6.834	1, 2
Cs	301.44	9.192	3, 4

Table 3.1 Melting points, hyperfine transitions, and ground state hyperfine numbers of stable alkali atom isotopes.

Chapter 4

Cavity-QED

Here I will introduce how we describe the interaction between our spins and light. This is the basis for our hybrid quantum system and remains an introduction to the techniques used in the field. I will begin by quantizing a classical electromagnetic field, and then begin transforming it into a quantum mechanical description. Afterwards, I will introduce the coupling between light and matter through the interaction between light and a single dipole (both electric and magnetic). From there I transition from one to many dipoles. At the end I introduce the framework to describe the dynamics of the spins with the cavity.

4.1 Photons in a cavity - Harmonic oscillators of a single mode

Over the past half-century, quantum electrodynamics (QED) has enabled some of the most precise measurements in human history. At its core, QED describes the fundamental interaction between light and matter. A quantized electromagnetic wave—a photon—can interact with electrons, protons, and even macroscopic objects like dielectric beads. As physicists, one of our most powerful tools is the ability to generate light and use it to control matter, and vice versa. By shining a laser at the right frequency, we can excite an electron to a higher energy state. However, on a fundamental level, the interaction probability between a single photon and a single electron—or any charged particle—is quite low ($1/\alpha$).

Using a laser, in relative terms, is a brute-force approach, sending $\sim 10^{16}$ photons per second in hopes of a successful interaction. This method has revolutionized physics, but what if we want to mediate an interaction between a single photon and a single

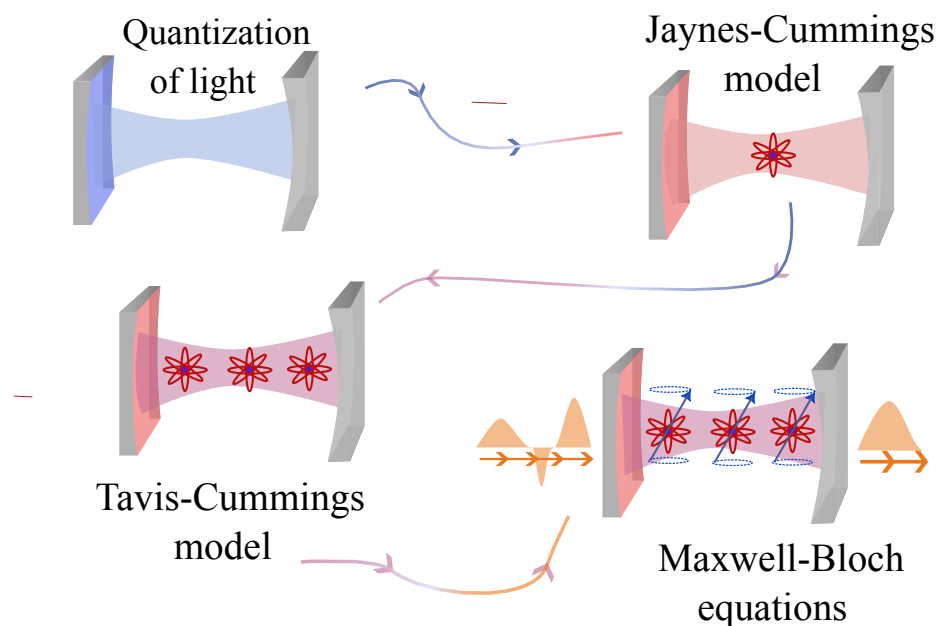


Figure 4.1 Pictorial representation of the theoretical models used in cavity QED. Starting with the quantization of light in a cavity, then adding a single (Jaynes-Cummings) to eventually many atoms (Tavis-Cummings), and eventually describing the combined dynamics (Maxwell-Bloch).

atom? The solution lies in cavity quantum electrodynamics (cavity-QED), where a photon is confined between two mirrors. Inside such a cavity, an atom "sees" the same photon potentially millions of times before the light escapes, dramatically enhancing the interaction. The field of cavity-QED has led to groundbreaking discoveries and is a crucial ingredient in building a quantum computer.

For a deeper dive into this field, I highly recommend Jean-Michel Raimond and Serge Haroche's book, *Exploring the Quantum: Atoms, Cavities, and Photons* [1], which should be on every incoming graduate student's desk.

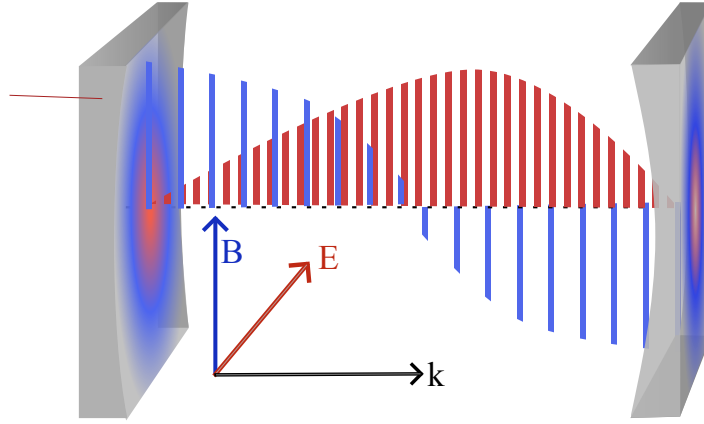


Figure 4.2 Visualization of the electric and magnetic field components created by two mirrors of a $\lambda/2$ cavity.

4.1.1 Light in a box

Here we begin with Maxwell's equations in a vacuum free of charges.

$$\begin{aligned}
 \nabla \cdot \vec{B} &= 0, \\
 \nabla \cdot \vec{E} &= 0, \\
 \nabla \times \vec{B} &= \frac{1}{c^2} \frac{\partial \vec{E}}{\partial t}, \\
 \nabla \times \vec{E} &= -\frac{\partial \vec{B}}{\partial t},
 \end{aligned} \tag{4.1}$$

where $c = \frac{1}{\sqrt{\mu_0 \epsilon_0}}$, and is the speed of light in a vacuum. Taking the curl of last two equations results in the following equations

$$\begin{aligned}
 \nabla \times (\nabla \times \vec{B}) &= \nabla \times \left(\frac{1}{c^2} \frac{\partial \vec{E}}{\partial t} \right) = -\frac{1}{c^2} \frac{\partial^2 \vec{B}}{\partial t^2}, \\
 \nabla \times (\nabla \times \vec{E}) &= \nabla \times \left(-\frac{\partial \vec{B}}{\partial t} \right) = -\frac{1}{c^2} \frac{\partial^2 \vec{E}}{\partial t^2}
 \end{aligned} \tag{4.2}$$

The clever student will notice that these equations are wave equations in free space. To bring these equations into a more relevant physical space, we can subject them to boundary conditions, i.e. between two mirrors. From here we will simplify both \vec{E} and

\vec{B} by assuming the light is traveling in one dimension along the cavity. If we assume that the mirrors are perfect conductors and the electric field polarization vector is in the x-direction (our choice), we can solve Maxwell's equations for an electromagnetic field inside of a cavity.

Solutions to the Maxwell equation's in a cavity take the form

$$E_x(z, t) = \sum_i \sqrt{\frac{2\omega_i^2}{V\epsilon_0}} E_0 \sin(k_i z + \omega t) \quad (4.3)$$

and

$$B_y(z, t) = \sum_i \left(\frac{\mu_0 \epsilon_0}{k_i} \right) \sqrt{\frac{2\omega_i^2}{V\epsilon_0}} B_0 \cos(k_i z + \omega t). \quad (4.4)$$

The prefactors μ_0 and ϵ_0 are the permeability and permittivity of the vacuum, V is the mode volume of the cavity, the angular frequency is ω_i , and the wave vector k_i both of the mode i . The wave vector is defined as $k = \frac{n\pi}{L}$ and sets the geometric boundary conditions of the cavity to the waves. Interestingly, due to the boundary conditions set by the cavity, the electric field and magnetic field are $\pi/2$ out of phase for the first mode (index $i = 1$). Within the cavity all modes exist, however, we will focus on the first fundamental mode unless explicitly mentioned otherwise. The Hamiltonian of the system which describes the energy density inside the cavity is then given by

$$H = \frac{1}{2} \int dV \left[\epsilon_0 \vec{E}^2(\vec{r}, t) + \frac{1}{\mu_0} \vec{B}^2(\vec{r}, t) \right] \quad (4.5)$$

By simple inspection, the Hamiltonian (4.5) is analogous to the equation which describes a simple harmonic oscillator. Recall that the Hamiltonian of a simple harmonic oscillator is

$$H = \frac{1}{2} \left(\frac{p^2}{2m} + kx^2 \right) \quad (4.6)$$

where x is the position, p the momentum, k the spring constant and m is the mass of the object. As a reminder, the classical equations of motion for a spring are

$$m \frac{d^2 x}{dt^2} = -kx \quad (4.7)$$

$$p = m \frac{dx}{dt} \quad (4.8)$$

with the following solutions

$$x(t) = x_0 \sin \left(\sqrt{\frac{k}{m}} t \right), \quad (4.9)$$

$$p(t) = p_0 \cos \left(\sqrt{\frac{k}{m}} t \right). \quad (4.10)$$

We can now rewrite our time dependent electric field and magnetic components as the following,

$$q(t) = \sqrt{\frac{\epsilon_0 V}{2\omega^2}} E_0 \sin(\omega t) \quad (4.11)$$

and

$$p(t) = \sqrt{\frac{V}{2\mu_0}} B_0 \cos(\omega t) \quad (4.12)$$

(as a reminder, $B_0 = E_0/c$). The Hamiltonian of the electromagnetic field in a cavity can now be written as

$$H = \frac{1}{2}(p^2 + \omega^2 q^2). \quad (4.13)$$

This is a fully classical description of light. However, one can already get the sense that quantum mechanics is starting to poke its head into our system. We will now begin quantizing the light modes and introduce a quantum mechanical description of light through operators.

4.1.2 Quantized light-photons

To transition from the classical treatment of light to the quantum mechanical, we begin by changing q and $p \rightarrow$ to \hat{q} and \hat{p} , where the hat above the variable signifies that these are quantum mechanical operators. These operators are commonly referred to as *observables*, meaning these are the quantities we will read on a detector, they are Hermitian, and they obey the commutation relationship

$$[\hat{q}, \hat{p}] = i\hbar. \quad (4.14)$$

Reworking the operator versions of 4.11 and 4.12 into the time dependent electric and magnetic field, our new description for the fields are

$$\hat{E}_x(z, t) = \sqrt{\frac{2\omega_i^2}{V\epsilon_0}} \hat{q}(t) \sin(k_i z) \quad (4.15)$$

and

$$\hat{B}_y(z, t) = \sqrt{\frac{2\omega_i^2 \mu_0}{V k_i}} \hat{p}(t) \cos(k_i z) . \quad (4.16)$$

Our new quantized Hamiltonian with operators is

$$\hat{H} = \frac{1}{2} (\hat{p}^2 + \omega^2 \hat{q}^2) . \quad (4.17)$$

It is now useful to introduce the dimensionless operators \hat{a}^\dagger and \hat{a} , which are commonly referred to as the creation and annihilation operators, respectively. They are defined as

$$\hat{a}^\dagger = \frac{1}{\sqrt{2\hbar\omega}} (\omega \hat{q} - i\hat{p}) \quad (4.18)$$

and

$$\hat{a} = \frac{1}{\sqrt{2\hbar\omega}} (\omega \hat{q} + i\hat{p}) . \quad (4.19)$$

With some substitution, we can describe the operators \hat{p} and \hat{q} with both the creation and annihilation operators,

$$\hat{p} = -i\sqrt{\frac{\hbar\omega}{2}} (\hat{a} - \hat{a}^\dagger) \quad (4.20)$$

and

$$\hat{q} = i\sqrt{\frac{\hbar\omega}{2}} (\hat{a} + \hat{a}^\dagger) . \quad (4.21)$$

Insert these operators into the electric and magnetic fields from equations (4.15) and (4.16) results in

$$\begin{aligned} \hat{E}_x(z, t) &= i\sqrt{\frac{\hbar\omega}{\epsilon_0 V}} (\hat{a} + \hat{a}^\dagger) \sin(kz) \\ &= \mathcal{E}_0 (\hat{a} + \hat{a}^\dagger) \sin(kz) \end{aligned} \quad (4.22)$$

and

$$\begin{aligned} \hat{B}_y(z, t) &= -i\sqrt{\frac{\hbar\omega\mu_0}{V}} (\hat{a} - \hat{a}^\dagger) \sin(kz) \\ &= \mathcal{B}_0 (\hat{a} - \hat{a}^\dagger) \cos(kz) . \end{aligned} \quad (4.23)$$

The constants \mathcal{E}_0 and \mathcal{B}_0 can be understood as the electric and magnetic field per photon. We can now plug in equations (4.20) and (4.21) directly into equation (4.17), resulting in the well known equation

$$\hat{H} = \hbar\omega \left(\hat{a}^\dagger \hat{a} + \frac{1}{2} \right) \quad (4.24)$$

where $\hat{a}^\dagger \hat{a}$ is our number operator, equaling the number of photons in the cavity with energy $\hbar\omega$, and the additional $1/2$ is the ground state energy. The eigenvalues of the Hamiltonian are $\hbar\omega(n + 1/2)$ where $n = (0, 1, 2, \dots)$ with integer steps and the eigenstates are the number states, $|n\rangle =$ photon number. The operators act on the number state accordingly,

$$a^\dagger |n\rangle = \sqrt{n+1} |n+1\rangle \quad (4.25)$$

$$a |n\rangle = \sqrt{n} |n-1\rangle \quad (4.26)$$

4.2 Light-matter interaction

Having quantized the electromagnetic field, it is instructive to show how light and matter can interact within a cavity. Beginning with a single photonic mode inside of a cavity, we place a single dipole inside. This dipole can be magnetic, such as the spin of an electron, or electric, such as the charge distribution in a polar molecule. However, it is useful to make some approximations before we go any further. The first is that the dipole is a two-level system, i.e. it has a single ground and excited state. Working within a single two-level system is the most simplistic yet important toy model in our wheel house. Understanding how a two-level system works will naturally lead to multilevel systems, however, that is outside the framework of this thesis. Typically, the dipole is a vector represented as \vec{d} , and the dipole operator is

$$\hat{d} = \sum_{n,m} \bar{d}_{n,m} |n\rangle\langle m| \quad (4.27)$$

where $|n\rangle\langle m|$ is the atom's basis, i.e. our two-level system, and $\hat{d}_{n,m} = \langle n|\vec{d}|m\rangle$. Our atomic Hamiltonian is defined as

$$H_{atom} = \sum_n E_n |n\rangle\langle n| \quad (4.28)$$

with eigenstates $|n\rangle$ and energies E_n . The second assumption we make is known as the ‘dipole approximation’. The dipole approximation stems from the fact that the dipole, let’s say an atom, is orders of magnitude smaller than the wavelength of light. An atom is approximately the size of one Bohr radius, $a_B \sim 10^{-10}$ m, while an optical photon has a wavelength of $\sim 500 \times 10^{-9}$ m (3 orders of magnitude larger). Microwave photons, which this experiment is based on typically have wavelengths of 10’s of centimeters. As such, the electric field can now be approximated as

$$\vec{E}(\vec{r}, t) = \vec{E}(R_{atom}, t) \equiv E(t). \quad (4.29)$$

The interaction energy between the dipole and the electromagnetic field [1] is then

$$H_{int} = -\hat{d} \cdot \hat{E}(t). \quad (4.30)$$

We now have all of the resources to describe the interaction between light and dipole in a cavity. From here, the $(\hat{})$ notation on the operators will be dropped, and the

Hamiltonian nomenclature will be the following:

H_c = Hamiltonian of the cavity

H_a = Hamiltonian of the atom

H_i = Hamiltonian of the interaction.

The Hamiltonian of the total system is now $H = H_c + H_a + H_i$, more specifically,

$$H = \hbar\omega_{eg} |e\rangle\langle g| + \hbar\omega_c a^\dagger a + i\frac{\hbar g}{2}(\sigma_+ + \sigma_-)(a - a^\dagger) \quad (4.31)$$

where ω_{eg} is the transition frequency of our two-level system, ω_c is the fundamental frequency of the cavity, g is the vacuum Rabi-frequency, and σ_+ and σ_- are the Pauli spin operators. They are a short hand notation of the following:

$$\sigma_+ = |e\rangle\langle g| \quad (4.32)$$

$$\sigma_- = |g\rangle\langle e|. \quad (4.33)$$

The vacuum Rabi-frequency is defined as

$$g = 2\frac{\bar{d}_{e,g} \cdot \bar{\mathcal{E}}}{\hbar} \sqrt{\frac{\hbar\omega_c}{\epsilon_0 V}} \sin(k_c z_a), \quad (4.34)$$

and gives the rate at which the cavity photon and dipole interact. In general, it is nice to maximize the coupling between the cavity and the dipole. This can be done by selecting a dipole with a large $\bar{d}_{e,g}$, increasing ω_c , or manipulating the dimensions of the cavity and reducing V . An analogous argument can be made for magnetic fields.

4.2.1 Jaynes-Cummings Hamiltonian

Now that we have the total Hamiltonian of a photon in a cavity, a dipole, and the interaction between them, we can now start to unravel the properties of cavity QED.

Interaction between spin and a photon

Above, we discussed coupling to the electric field, but to align more closely with our experiment—where we couple electron magnetic dipoles to the magnetic component of the electromagnetic field in our GHz superconducting resonator—we will now focus on

magnetic dipole interactions. Fundamentally, the interaction follows the same principles as electric dipole coupling, as both involve a dipole interacting with its corresponding field. In analogy to the electric dipole interaction from equation 4.30, the magnetic dipole interaction with an external magnetic field is described by

$$H_{\text{int}} = -\mu \cdot B, \quad (4.35)$$

where μ is the magnetic dipole operator and B is the magnetic field operator. The magnetic dipole of a single electron is

$$\begin{aligned} \vec{\mu} &= -\frac{g_e \mu_B \vec{S}}{\hbar} \\ &= -\frac{g_e \mu_B}{\hbar} (|e\rangle\langle g| + |g\rangle\langle e|) \\ &= -\frac{g_e \mu_B}{\hbar} (\sigma_+ + \sigma_-) \end{aligned} \quad (4.36)$$

where \vec{S} is the spin projected along the magnetic field, which gives $\vec{S} = \hbar \sigma_x / 2$, σ_+ and σ_- represent the dipole transition operators that brings the spin either from the ground state to the excited, or vice versa. The total interaction Hamiltonian between the spin of an electron and the magnetic field can now be written as

$$\begin{aligned} H_{\text{int}} &= -\frac{g_e \mu_B}{\hbar} \vec{S} \cdot \vec{B} \\ &= i \frac{g_e \mu_B \mathcal{B}_0 \cos(kz)}{2} (\sigma_+ + \sigma_-)(a - a^\dagger) \end{aligned} \quad (4.37)$$

We can combine the constants in the front into a new term $g = -g_e \mu_B \mathcal{B}_0 \cos(kz) / \hbar$ which tells us the coupling strength between a single photon and a magnetic dipole of spin 1/2 (take note that we defined it as negative). The condensed version of the interaction Hamiltonian is

$$\begin{aligned} H_{\text{int}} &= i\hbar g (\sigma_+ + \sigma_-)(a - a^\dagger) \\ &\approx i\hbar g (\sigma_- a^\dagger - \sigma_+ a). \end{aligned} \quad (4.38)$$

The first term $\sigma_- a^\dagger$ creates a photon by lowering our spin while the second term removes a photon from the cavity in order to raise the spin. The two terms which have been left out are considered two photon processes and operate at much higher frequencies than the main interaction, specifically the $\sigma_+ a^\dagger$ term and $\sigma_- a$. Ignoring these terms is done so by the rotating wave approximation (RWA), where the coupling strength of the dipole to the field is much smaller than the field's frequency and larmor

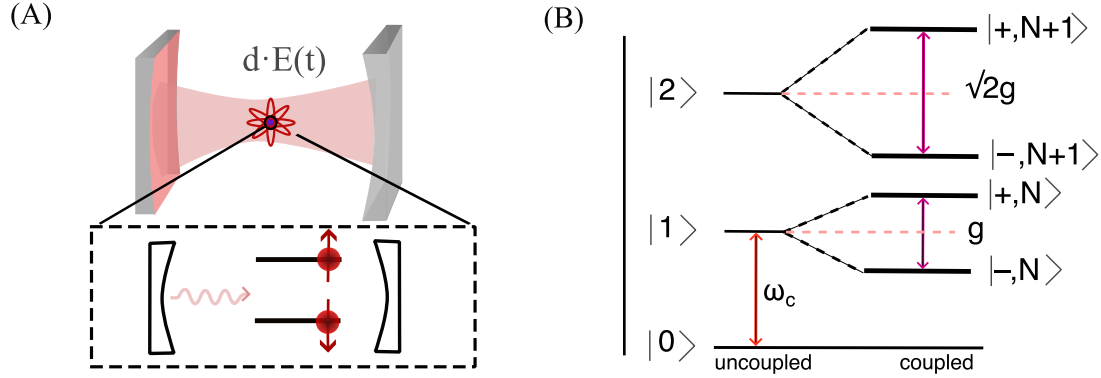


Figure 4.3 (A) Visualization of a single spin in a Fabre-Perot cavity which is the basic model behind the Jaynes-Cummings Hamiltonian. A single spin's dipole couples to the electromagnetic field confined between the cavity. The system is hybridized between the two states of 'photon and spin down' (in picture's model) and 'absorbed and spin up'. (B) Jaynes-Cummings ladder, where the hybridized energy levels are increasingly split by \sqrt{N} , where N is the number of photons.

frequency of the dipole ($g \ll \omega_c, \omega_{e,g}$). And there we have it, the total Hamiltonian which includes the atom/spin, the cavity, and their interaction, also known as the Jaynes-Cummings (J.C.) Hamiltonian.

$$H = \hbar\omega_{eg}\frac{\sigma_z}{2} + \hbar\omega_c a^\dagger a + i\hbar g(\sigma_- a^\dagger - \sigma_+ a) \quad (4.39)$$

From here, we are able to remove the vacuum energy of the cavity and diagonalize the Hamiltonian [73] resulting in the exact eigenenergies

$$E_{\pm}^{(n)} = n\hbar\omega_c - \frac{\hbar\Delta}{2} \pm \frac{\hbar}{2}\sqrt{\Delta^2 + g^2n} \quad (4.40)$$

where $\Delta = \omega_{eg} - \omega_c$, and n is the total number of photons. They have eigenstates

$$\begin{aligned} |-\rangle_n &= \frac{1}{\sqrt{2}}(|g, n+1\rangle - |e, n\rangle) \\ |+\rangle_n &= \frac{1}{\sqrt{2}}(|g, n+1\rangle + |e, n\rangle), \end{aligned} \quad (4.41)$$

where the angle θ is defined as

$$\theta = \tan^{-1} \left(\frac{2g\sqrt{n+1}}{\Delta} \right) \quad (4.42)$$

These states are commonly referred to as "dressed states". One can view the system as being in a superposition of spin up with a bare cavity or spin down with a photon in the cavity. The Jaynes-Cummings model's interaction Hamiltonian explicitly couples the atomic states with discrete photon numbers, naturally leading to a description in terms of Fock states $|n\rangle$. Each eigenstate $|\pm, n\rangle$ represents a coherent superposition of atomic excitation and cavity photon number, where the quantization of light manifests as discrete vacuum Rabi oscillations. The \sqrt{n} scaling in the energy splitting highlights the nonlinear nature of light-matter interaction at the quantum level, distinguishing it from classical harmonic oscillations. This can be seen in Figure 4.3.

4.2.2 Tavis-Cummings Hamiltonian

The J.C. model describes a situation with a single emitter, cavity, and N photons. One may wonder, what happens to the dipole-cavity interaction if more than one emitter coupled to the field. For *many* systems, this scenario becomes relevant, and or a necessity. As it turns out, experimentally it can be quite difficult to measure the interaction between a dipole and photons inside a cavity, in particular when dealing with magnetic dipoles as their interaction is much weaker than their electric counterpart. Here we will give the general framework that will allow us to extend the J.C. model into the so called Tavis-Cummings model, where in addition to an arbitrary number of photons inside the cavity, we will also have $N > 1$ dipoles interacting with the electromagnetic field.

From Single Particle to Ensemble: Insights into the Tavis-Cummings Hamiltonian

Extending the Jaynes-Cummings model to the Tavis-Cummings model requires relatively little additional effort, which is not always the case for such generalizations. Here, the number of spins increases from 1 to N , and, in general, their interaction with the photonic field can vary due to differences in their positions within the cavity. These additional features lead to the following Hamiltonian,

$$H = \hbar\omega_c a^\dagger a + \sum_{j=1}^N \frac{\hbar\omega_{eg}^j \sigma_z^j}{2} + i\hbar \sum_{j=1}^N g_j (\sigma_-^j a^\dagger - \sigma_+^j a). \quad (4.43)$$

Here, we have modified the spin operator to include the addition of N spins and the coupling interaction for each spin, g_j . We can assume that the transition energy $\hbar\omega_{\text{eg}}$ is the same for each spin. However, this is not always the case experimentally, so summing over ω_{eg}^j for each j may also be required.

We can rewrite the spin operators as the following sums

$$\begin{aligned} S_z &= \sum_j^N \sigma_z^j \\ S_{\pm} &= \sum_j^N \sigma_{\pm}^j. \end{aligned} \quad (4.44)$$

The photonic field inside the cavity perceives the collective spin ensemble as a single "giant" dipole. The coupling strength of this "giant" dipole contributes to the photonic field interaction term in a manner similar to that in the Jaynes-Cummings model (4.39). To extend the Jaynes-Cummings model to the Tavis-Cummings model, the interaction term involves a sum over the individual coupling constants g_j for each spin. However, when the spins couple collectively to the photonic field, we introduce an effective collective coupling constant g_{eff} , which scales as \sqrt{N} for N spins. Specifically, the sum over g_j can be rewritten as

$$g_{\text{eff}} = \sqrt{\sum_{j=1}^N g_j^2}. \quad (4.45)$$

For identical couplings $g_j = g$, this simplifies to

$$g_{\text{eff}} = g\sqrt{N}. \quad (4.46)$$

The Tavis-Cumming Hamiltonian can now be written as

$$H = \hbar\omega_c a^\dagger a + \frac{\hbar\omega_{\text{eg}} S_z}{2} + i\hbar g_{\text{eff}} (S_- a^\dagger - S_+ a), \quad (4.47)$$

with eigenenergies

$$E_{\pm} = \hbar\omega_c \pm \sqrt{N}\hbar g. \quad (4.48)$$

4.2.3 Driven Tavis-Cummings Hamiltonian

Manipulating our spins is typically done by introducing an external coherent drive. As such, the interaction Hamiltonian must now be adjusted. First, we derive the

interaction Hamiltonian that governs the coupling between a quantized magnetic field and the external classical drive, and then apply the rotating wave approximation (RWA) to simplify the expression. Finally, we present the complete driven Tavis-Cummings Hamiltonian, incorporating the necessary transformations to remove time dependence, and accounting for detuning effects in individual spins due to the drive.

The interaction Hamiltonian describing the coupling between a quantized magnetic field and a classical drive field, characterized by a drive frequency ω_p and a time-dependent amplitude A_0 , is given by:

$$H_{\text{dr}} = -i\hbar B_0 \left(a e^{-i\omega t} - a^\dagger e^{i\omega t} \right) A_0 \cos(kz) \cos(\omega_p t). \quad (4.49)$$

This expression can be rewritten as:

$$H_{\text{dr}} = -i\hbar B_0 \left(a e^{-i\omega t} - a^\dagger e^{i\omega t} \right) \cos(kz) \frac{A_0}{2} \left(e^{i\omega_p t} + e^{-i\omega_p t} \right). \quad (4.50)$$

By applying the RWA and discarding the rapidly oscillating terms of the form $\pm(\omega + \omega_p)$, we arrive at the simplified drive term:

$$H_{\text{dr}} = i\hbar\eta \left(a^\dagger e^{-i\omega_p t} - a e^{i\omega_p t} \right), \quad (4.51)$$

where η represents the effective amplitude of the external drive, which may vary with time and is averaged over half the period of the cosine.

When combining all contributions, the full driven Tavis-Cummings Hamiltonian becomes

$$H = \hbar\omega_c a^\dagger a + \sum_{i=1}^N \frac{\hbar\omega_i}{2} \sigma_i^z + i\hbar \sum_{i=1}^N g_i \left(\sigma_i^- a^\dagger - \sigma_i^+ a \right) + i\hbar\eta \left(a^\dagger e^{-i\omega_p t} - a e^{i\omega_p t} \right). \quad (4.52)$$

To eliminate the explicit time dependence in the drive term, we perform a unitary transformation into the rotating frame with respect to the drive frequency. The detuning of each spin from the external drive is given by $\Delta_i = \omega_i - \omega_p$. This Hamiltonian incorporates both the inhomogeneous broadening of the spins and any variations in the individual coupling strengths between the spins and the field.

$$H_u = \hbar\Delta_c a^\dagger a + s_z + i\hbar g_i \left(\sigma_i^- a^\dagger - \sigma_i^+ a \right) + i\hbar\eta \left(a^\dagger - a \right) \quad (4.53)$$

4.2.4 Maxwell-Bloch Equations

The system described above is extremely useful, but a rather incomplete description of a real system. The model which we used does not include any dephasing terms, such as dissipation or decoherence. Both of these effects are incredibly useful, as we use the photons exiting the system as a method to measure the system, i.e. through a transmission line. Luckily, these mechanisms can be taken into account by assuming an open quantum system, where the system is coupled the environment and using the Lindblad Master equation.

The new Hamiltonian, includes the original system, the environment, and the interaction between the two

$$H_{tot} = H_{sys} + H_{env} + H_{int} . \quad (4.54)$$

We can trace over the environmental degree of freedom and obtain the following master equation:

$$\frac{d\hat{\rho}_{tot}(t)}{dt} = -i[\hat{H}(t), \hat{\rho}(t)] + \sum_n \frac{1}{2} \left(\hat{L}_n \hat{\rho}(t) \hat{L}_n^\dagger - \hat{\rho}(t) \hat{L}_n^\dagger \hat{L}_n - \hat{L}_n^\dagger \hat{L}_n \hat{\rho}(t) \right) \quad (4.55)$$

The collapse operators, $\hat{L}_n = \sqrt{\gamma_n} \hat{A}_n$, describe the interaction of the system with the environment, where \hat{A}_n represents the operator responsible for the coupling, and γ_n is the corresponding coupling rate. The second term in the equation is referred to as the Liouvillian (\hat{L}) of the system.

Bringing everything together, we obtain a Liouvillian of the following form (for simplicity, we omit the operator notation from here on):

$$L = \kappa \left(\frac{1}{2} a \rho a^\dagger - a^\dagger a \rho - \rho a^\dagger a \right) + \gamma_{\parallel} \sum_j \left(\frac{1}{2} \sigma_j^- \rho \sigma_j^+ - \sigma_j^+ \sigma_j^- \rho - \rho \sigma_j^+ \sigma_j^- \right) + \gamma_{\perp} \sum_j \left(\frac{1}{2} \sigma_j^z \rho \sigma_j^z - \rho \right) \quad (4.56)$$

Using $\langle o \rangle = \text{Tr}(\rho o)$, we arrive at a set of coupled differential equations that describe the dynamics of our system:

$$\begin{aligned}
\langle \dot{a} \rangle &= -(\kappa + i\Delta_{\text{eg}})\langle a \rangle + \sum_{j=1}^N g_j \langle \sigma_-^j \rangle + \eta \\
\langle \dot{\sigma}_-^j \rangle &= -(\gamma_{\perp} + \frac{\gamma_{\parallel}}{2} + i\Delta_s^j)\langle \sigma_-^j \rangle + g_j \langle a \sigma_z^j \rangle \\
\langle \dot{\sigma}_z^j \rangle &= -\gamma_{\parallel}(1 + \langle \sigma_z^j \rangle) - 2g_j (\langle a^{\dagger} \sigma_-^j \rangle + \langle a \sigma_+^j \rangle)
\end{aligned} \tag{4.57}$$

From here, it is worth going into further details regarding the system. First, the system dissipates energy via photons (\hat{a}) leaving the cavity at a rate κ . The loss of information involving the spins, noted by γ can be separated into two different rates. The first can be understood as the decay of an excited spin, which could be triggered by spontaneous emission, phononic interactions in the solid, or diffusion of spins to other local emitters. This decay occurs at a rate $\gamma_{\parallel} = 1/T_1$. The second mechanism is to be understood as the loss rate of coherence of the spins at a rate $\gamma_{\perp} = 1/T_2$, more commonly referred to as the decoherence rate. These coupled equations are known as the Maxwell-Bloch equations, and are extremely useful when one wants to understand the dynamics of a photons, atoms, and cavities.

4.2.5 Holstein-Primakoff approximation

Spin operators are inherently nonlinear and difficult to analyze directly, especially in systems involving large numbers of interacting spins. Here, we introduce the Holstein-Primakoff approximation, which is used to simplify the study of spin systems by providing a more manageable description of spin operators. The approximation addresses this by transforming spin operators into bosonic creation and annihilation operators b and b^{\dagger} .

The spin operators can now be transformed to produce

$$\begin{aligned}
S_+ &= b^{\dagger} \sqrt{2S - b^{\dagger}b} \\
S_- &= \sqrt{2S - b^{\dagger}b} b \\
S_z &= (b^{\dagger}b - S)
\end{aligned} \tag{4.58}$$

which follow the same rules as the creation and annihilation operators a and a^{\dagger} . The approximation comes into play by assuming that the boson occupation number $\langle b^{\dagger}b \rangle$

is smaller than the number of spins $2S$. Under this assumption, the square root terms can be expanded into a Taylor series, and higher-order terms can be neglected, leading to a linearized or simplified description of the spin dynamics.

$$\begin{aligned} S_+ &\approx b^\dagger \sqrt{2S} \approx \sqrt{N} b^\dagger \\ S_- &\approx \sqrt{2S} b \approx \sqrt{N} b. \end{aligned} \quad (4.59)$$

We can now incorporate this approximation to the Tavis-Cummings Hamiltonian from Eq. 4.47. The new Hamiltonian, including the Holstein-Primakoff approximation is

$$H = \hbar\omega_c a^\dagger a + \hbar\omega_{eg}(b^\dagger b - S) + \hbar g \sqrt{N}(ab^\dagger + a^\dagger b). \quad (4.60)$$

This approximation begins to break down as the number of photons in the cavity reach \sqrt{N} , as the higher terms must now be included.

Chapter 5

Experimental Setup

This chapter introduces the experimental setup, along with the modifications to both the cryogenic system and its external components from my master's thesis. However, I do introduce the necessary information to begin a cryocrystal experiment.

A key goal of this setup was to ensure modularity, particularly in terms of impurities and host matrices, allowing for quick switching between them or both. Additionally, this chapter details the optical setups used both inside and outside the cryogenic system for crystal growth and characterization. I will also introduce the superconducting magnet system used to tune atoms into resonance with the cavity, as well as the microwave cavity and measurement scheme employed to manipulate and measure our atoms.

5.1 Cryosystem

This section explains the rationale behind choosing the adiabatic demagnetization refrigerator (ADR) over a typical dilution refrigerator. A detailed design, including thermal calculations of the experimental setup, can be found in my master's thesis [74]. In this section, I will outline the modifications made to the original design, along with essential information for clarity. Below is a simplified schematic of the cryogenic setup.

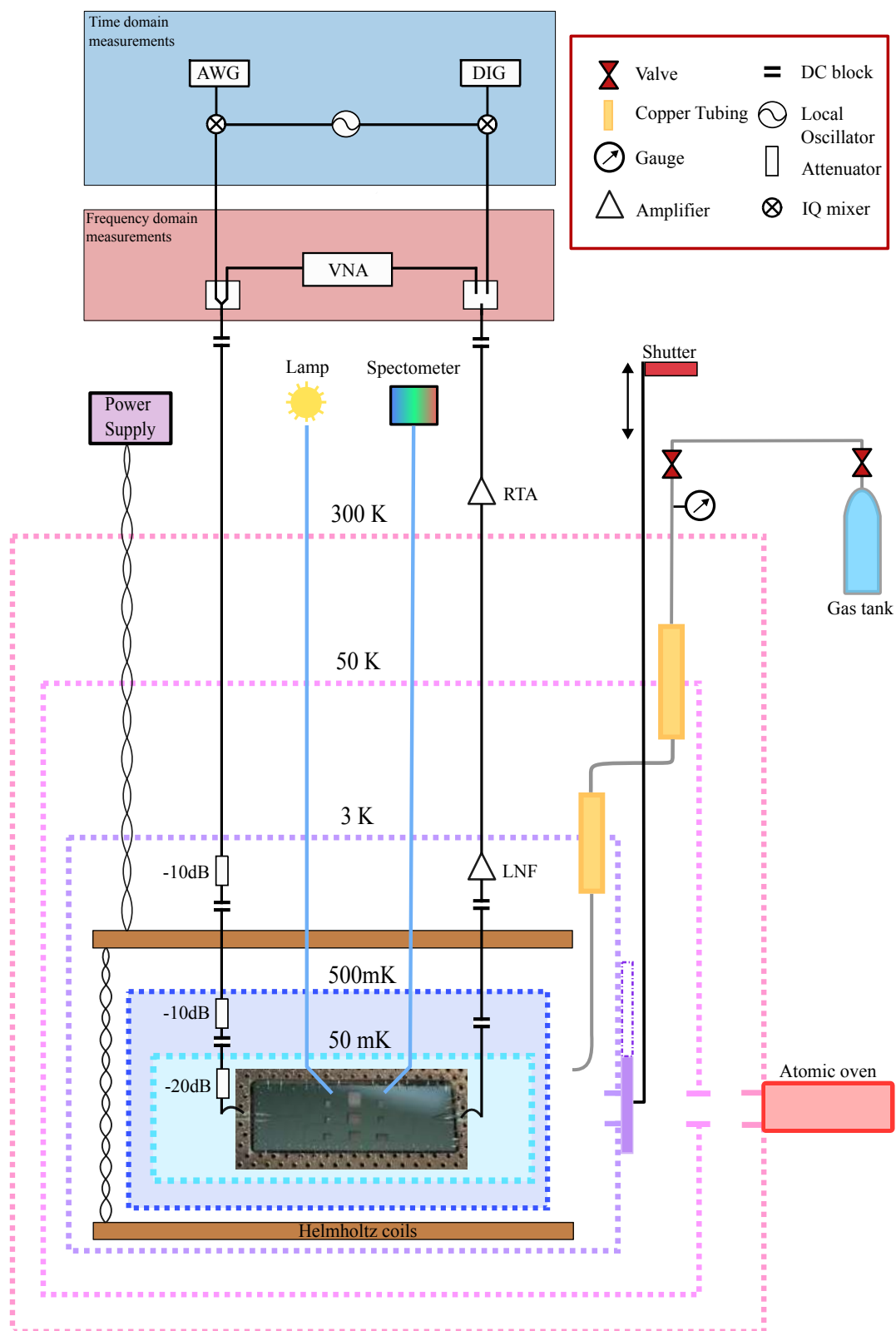


Figure 5.1 Pictorial representation of the experimental setup, both inner and outer equipment. The dashed boxes represent the thermal shielding at their base temperatures (300 K, 50 K, and 3 K).

5.1.1 ADR

The ADR offers several advantages over a conventional dilution refrigerator, primarily its flexibility in modifying the system and its ability to reach base temperature in under 24 hours. Additionally, it provides high cooling power and allows for variable substrate temperature during deposition. However, it does have limitations, including a finite hold time below 50 mK and a base temperature of approximately 40 mK.

For applications requiring long-term stability at ultra-low temperatures—such as coupling to a single spin or impurity for quantum memory—a dilution refrigerator is the preferred choice, as it can maintain temperatures below 20 mK indefinitely. Nevertheless, the ADR provided significant flexibility for our initial experiments on hybrid quantum systems.

The cryogenic system used in this experiment was the STARCRYO ADR Model DRC-100, operated with a Sumitomo SRP-082B pulse tube cooler, which provides 0.9 W of cooling power on the second stage.

5.2 ADR modifications for the production of cryogenic crystals

5.2.1 Gas deposition setup

The creation of these crystals begins by connecting a scientific-grade gas tank, maintained at room temperature, to our cryostat. The gas is first regulated by a precision needle valve located just before the 300 K shield. After passing through the needle valve, the gas enters the cryosystem via a gas feedthrough, which is initially pumped down to a pressure below 1×10^{-5} mbar. Once inside the cryosystem, the gas passes through a long, thin, stainless steel tube until reaching the first copper tube (shown in Figure 5.2 (A)) that is thermally anchored to the first cooling stage of the cryostat. The tube is typically held at a base temperature of approximately 30 K. For gases such as p-H₂ and Ne, this temperature is above their freezing points. The copper tubing attached to the first cooling stage reduces the temperature of the incoming gas from 300 K to around 40 K. For gases heavier than neon, this thermal clamp should be removed to prevent freezing, which could otherwise inhibit the growth of the crystals.

After passing through the first thermal cooling section, the gas flows through another thin stainless steel tube which acts as a thermal break and channels the gas to the final copper tubing. This can be seen in Figure 5.2 (B). Upon entering the final

cooling stage, the gas is once again cooled by the copper tubing. In this copper section, the tubing is filled with a material that enhances thermal contact without hindering the gas flow. Currently, for experiments using parahydrogen, the gas flows through the iron oxide, as detailed in Reference [66].

This section is given particular attention, as the second stage of the cryosystem has a base temperature of 2.6 K, which is far too low for any noble gases or molecules, except He. The base temperature of the copper tube is approximately 6 K. The final cooling stage of the gas is located both above and below the second stage and is thermally coupled via a thin, threaded, stainless-steel screw that is connected to both the second stage and the copper tubing. The length of the screw between the two sets the base temperature. If you want the tube colder, reduce the length.

To raise the temperature of the tube, we have built a two-point PID system that controls the temperature of the final stage when growing. The PID system is composed of two low-temperature diodes and a 100-Ohm resistor positioned above the second stage. Both of them can be seen in Figures 5.2 (B and C). From here, the gas flows through the copper tubing and enters the final stage of its journey before becoming a crystal: the nozzle. The nozzle, a thin stainless steel tube, is directed towards the opening of the superconducting circuit, as seen in Figure 5.2 (C), where the crystal is grown.

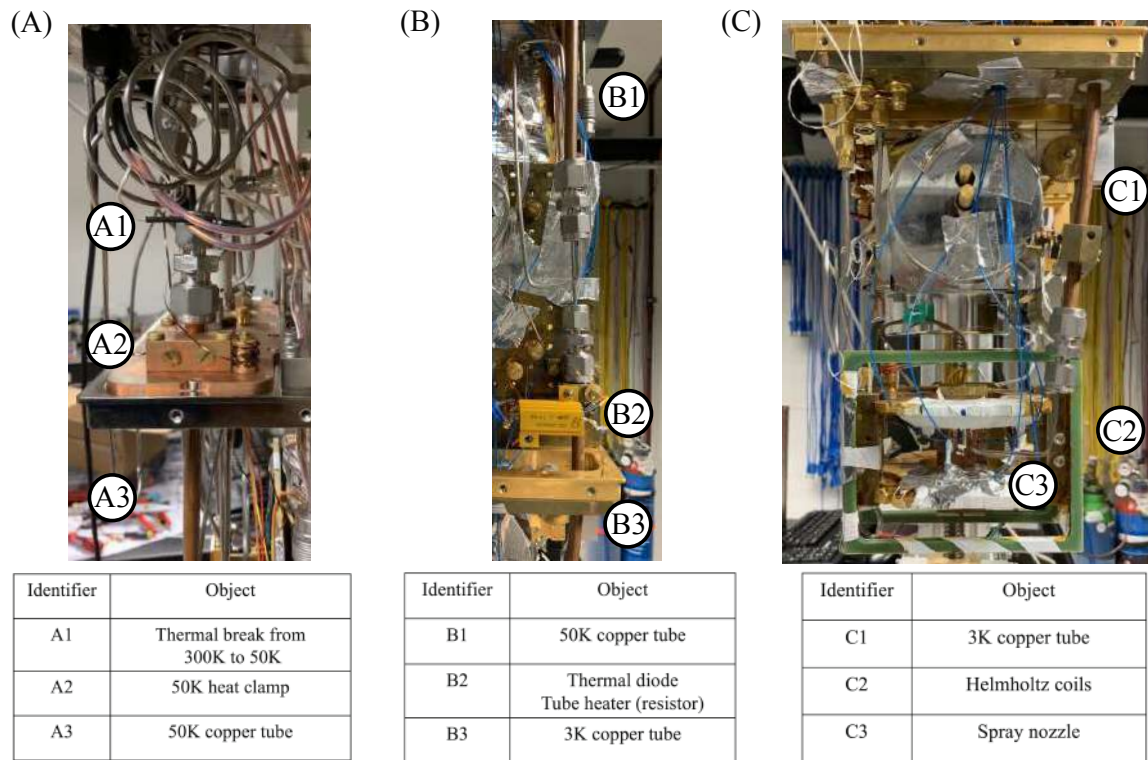


Figure 5.2 (A) 1st cooling state of the cryosystem. Marked in the figure are the key components to the integration of the cryogenic gases into the ADR. A1 is a thin stainless steel tube which acts as a thermal break between the 300 K stage and the 50 K stage. The looped tube is sufficiently long as to not create a thermal "short" between the two stages. A2 is the thermal clamp, which thermalizes the copper tube and effectively the cryogenic gases. This is considered a precooling stage as the first stage of the cryostat has a large cooling power and can effectively cool gases from 300 K to roughly 40 K. A3 is the copper tube which is thermalized to the 50 K stage. It is filled with the iron oxide catalyst used to convert $o\text{-H}_2$ to $p\text{-H}_2$. It also acts as a large surface area which the gas can deposit its thermal energy. (B) B1 is the same copper tube identified as A3, including now the thermal break (thin stainless steel tube) between the 50 K and 3 K stage. B2 is the thermal heater used to regulate the temperature of the exiting gas. B3 is the 3 K copper tube, and it is also filled with the iron oxide catalyst. (C) C1 shows the copper tubing, B3 from previous image, below the 3 K stage. C2 represents the Helmholtz coils used to Zeeman tune the atoms onto resonance. C3 is the stainless steel nozzle that the cryogenic gases exit. The nozzle is aimed towards the superconducting chip and is approximately 6 cm away.

For future experiments, it would advantageous to put limit the blackbody radiation from the copper tube connected to the 4 K stage. This could be done by either moving it outside of the thermal shield while still thermally coupled, or by simply putting a

thermalized shutter in front of it. The shutter would also offer the ability to create a deterministic method to control the deposition of the gas.

5.2.2 Additional modifications

In addition to many of the necessary equipment used for growing the crystal, we also have an additional heater located directly on the 2nd stage for annealing as well as melting of the crystal. Rapid melting of the crystal while the cryosystem remains cold and under vacuum allows for fast crystal creation and characterization. This is a basic 25 Ohm resistor which is mounted on the 2nd stage plate.

We also placed a thermal shutter which is mounted on the 3 K stage, and thermally anchored to the 50 K stage. The shutter was 3D printed and has aluminum tape on both sides to reflect the black-body radiation (BBR) from the deposition hole as well as emit only 70 K BBR on 4 K shield . It is manually operated outside of the cryostat, and when we are ready for crystal growth we open the shutter. Reducing the blackbody radiation leakage helps maximize the lifetime of the 50 mK stage, as the light emitting hole is directly in plane with the superconducting resonator. The shutter can be seen in Figure 5.3.

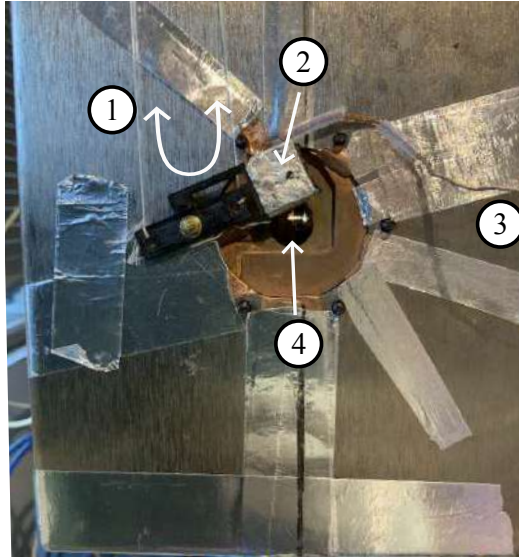


Figure 5.3 Image of the 4 K heat shield with the thermal shutter attached. The shutter's position (open/closed) is mechanically changed by pushing and pulling (1) on thin strings attached to a rotor outside of the 300 K shield. The shutter's face (2) is cooled in order to reduce the 300 K blackbody radiation inside the 70 K shield. A thin copper braid (3) is thermally anchored to the 70 K shield which cools the wrapped aluminum tape. The deposition hole (4) with the superconducting chip centered. "Star" taping help thermally couple copper braids used to cool shutter mounting piece.

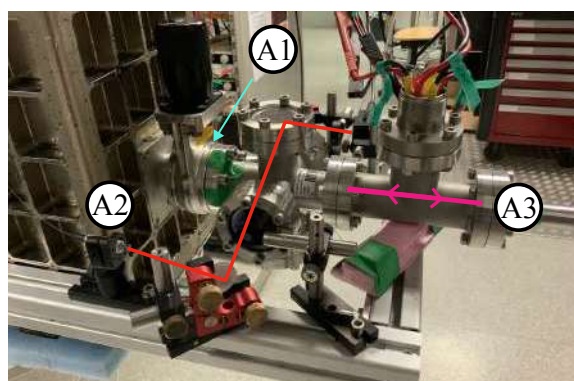
5.2.3 Impurity upgrade

Reference [74] provides minimal details about the design of the atomic oven, stating only that it was attached to the shield. This experimental setup has undergone several iterations of atomic ovens to improve usability and modularity. When designing and building the experiment, we anticipated frequent openings and closings of the fridge, which would make replacing the impurity reservoir both tedious and wasteful if it was always in contact with air. For these reasons, we aimed to isolate the oven from the interior of the cryosystem until it was under vacuum. This was achieved by placing the oven in a separate chamber that could remain under vacuum between fridge openings. Furthermore, if impurities need to be changed, we can, in principle, simply warm up the cryostat and swap out oven sections, allowing us to start cooling down the same day. This was accomplished using a high-vacuum seal valve attached to the cryostat's vacuum shield, with the oven chamber on the opposite side, as shown in Figure 5.4 (A).

The oven chamber is equipped with optical windows to perform absorption spectroscopy of the atomic flux exiting the nozzle. Additionally, the oven is connected to a

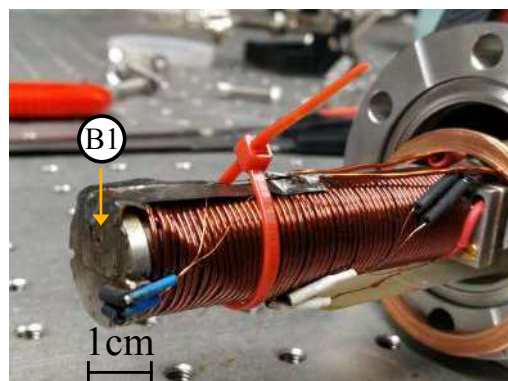
linear actuator that pushes the oven forward when we are ready to grow the crystal. Atoms are heated with an inductive coil wrapped around the hollowed stainless steel oven. Monitoring the atomic flux while the oven is warm and away from the shields has been invaluable in reproducing our crystals.

(A)



Identifier	Object
A1	Ultra-high vacuum seal
A2	Optical path for impurity absorption spectroscopy
A3	Linear actuator (arrows represent degree of freedom)

(B)



Identifier	Object
B1	Impurity nozzle

Figure 5.4 (A) Optical and mechanical setup for the atomic oven. A1 represents the ultra-high vacuum valve used to seal the oven chamber when opening the cryostat to atmosphere. A2 indicates the optical beam path for absorption spectroscopy, primarily for rubidium. A3 is the linear actuator to which the oven is attached. The actuator pushes the oven forward when ready for crystal growth and retracts it once the growth is completed. (B) Atomic oven, which is inductively heated. B1 denotes the nozzle, which is maintained at a higher temperature than the oven body. *The zip tie was used to stabilize the wires during the curing of the epoxy.*

5.3 Optical setup modifications

5.3.1 Inside cryostat

In addition to the optical setup for the oven, optical fibers are routed into the cryosystem to probe the crystal. When using $p\text{-H}_2$ as a host matrix, the fibers are also employed to perform FTIR spectroscopy on the solid, which provides the ratio of $o\text{-H}_2$ to $p\text{-H}_2$; the data can be found in the Appendix 1. Moreover, the fibers can serve as a method to measure the crystal's thickness during growth through thin-film interference. Their

primary functions include enabling absorption spectroscopy on the doped crystal and, as will be discussed later, facilitating the bleaching of the crystal. The fibers travel through the cryosystem until they are mounted directly above the superconducting resonator at a 45° angle relative to the chip's plane. The chip is quite reflective, and we perform absorption spectroscopy by shining the light through one fiber and picking up the reflection with another.

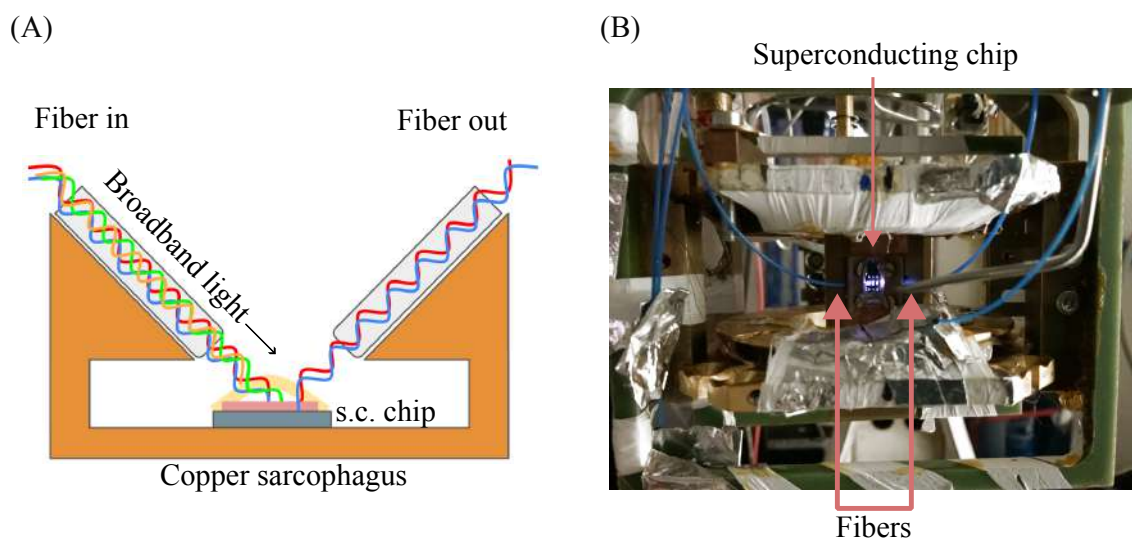


Figure 5.5 (A) Pictorial representation of the optical fiber setup on the superconducting chip's copper box. The fibers, both in and out, are clamped to the copper sarcophagus for stability. The broadband light used for absorption spectroscopy reflects off of the superconducting chip into the outgoing fiber. (B). Picture of the actual fiber optics setup. The fibers (thin blue lines) come down and shine white light onto the superconducting chip. Light is on in the picture.

5.3.2 Outside of cryostat

We have three main optical setups located outside of our cryosystem: one for the oven which is completely outside of the fridge, one for absorption spectroscopy of the impurities in the crystal, one for measuring the atomic flux outside of the oven, and finally one for measuring the purity of $o\text{-H}_2$ to $p\text{-H}_2$. Below is a schematic depicting of our setup. We use the absorption spectroscopy light for bleaching as well, which will be discussed in its own section.

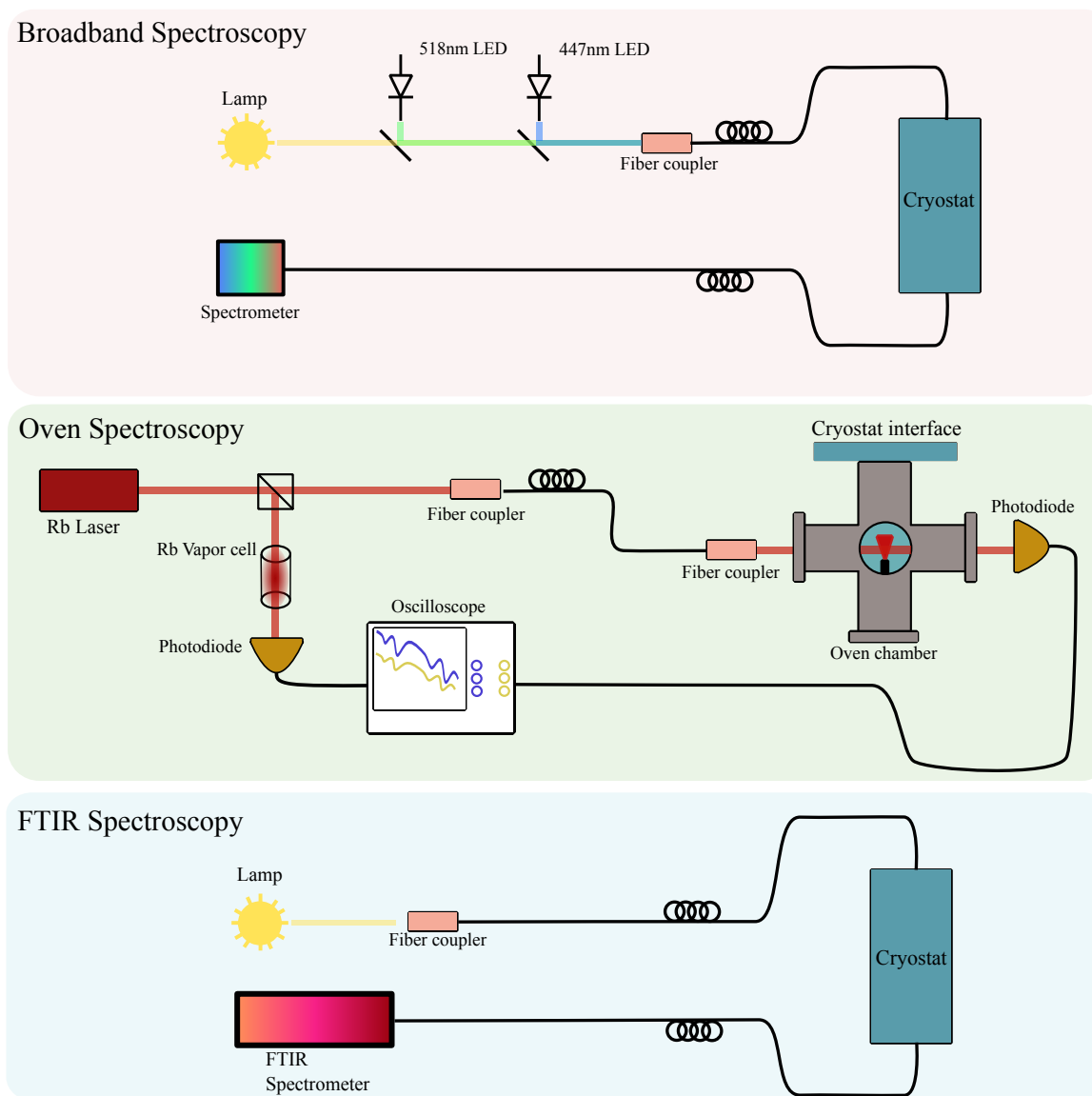


Figure 5.6 Optical setups outside of the cryosystem.

Absorption in the crystal: atomic impurities

The optical setup which is used for verifying that the atoms indeed are trapped in the crystal is composed of two LEDs and one broadband lamp. Though the majority of the D1/D2 transitions are covered within the broadband lamp, it became important to include two higher wavelength LEDs for Na. The three sources of light are then coupled directly into an optical fiber that enter the cryostat. After the light is reflected off the chip and picked up by the out going fiber, it then enters an optical spectrometer.

Absorption of the crystal: FTIR

In order to measure the purity of the p-H₂ crystal, we can measure certain rotational and vibrational transitions which is explained in detail in Reference [66]. Our current setup is similar as we have a broadband thermal light source, however, differ as we couple the light directly to a fiber and have purchased a Thorlabs FTIR with resolution of 0.25 cm⁻¹ for analysis.

Absorption of the atomic beam

The absorption of light on resonance immediately after the atoms leave the oven is one method to create a reproducible crystal. Though we did not use this method with Na as we did not have a laser, this setup was used extensively with Rb. The absorption spectroscopy is the typical setup involving a laser which is sent through a reference cell as well as the vapor leaving the oven.

5.4 Superconducting magnet setup

There are two sets of Helmholtz coils in the experiment. The first, and strongest is used for tuning our atoms in resonance with our superconducting resonator via the Zeeman interaction. It is in the z-direction, which is in plane with the chip. This coil, as seen in figure 5.2 (C) is thermally anchored to the 2nd stage of the cryosystem and can reach fields of 0.100 mT and is aligned to be (in plane) with the superconducting resonator. The second coil, commonly referred to as the off axis coil is used for minor corrections of the magnetic field from the main coil. The off axis coil's magnetic field is aligned to be perpendicular to the superconducting resonator and produces fields around 0.05 mT. It is also thermally anchored to the second stage.

Helmholtz (HH) Coils		
Coil info (units)	HH1	HH2
Inner radius [mm]	24	24
Outer radius [mm]	35	35
Total windings	3000	3000
Resistance at 300 K [Ω]	2064	2142
Inductance [mH]	829	829
Off-axis coil		
Coil info (units)	Off-axis coils 1 & 2	
Width [mm]	62	
Height [mm]	53	
Total windings	462	
Resistance at 300 K [Ω]	793	
Inductance per coil [mH]	61.5	
Field constant [mT/A]	0.0055	

Table 5.1 Parameters for the Helmholtz (HH) and off-axis coils. The resistance for the rectangular off-axis coil set is for the full pair, while the inductance is for an individual coil. Both pairs of coils were repurposed from a previous experiment.

5.5 Microwave setup

The microwave equipment can be split into two types of measurements: frequency and time. The microwave setup has both equipment inside and outside of the cryostat.

5.5.1 Frequency domain microwave equipment

The setup is shown in Figure 5.1. The equipment used for the time domain is centered around a Vector Network Analyzer (VNA). A VNA is able to measure electrical signals at high frequencies, and is able to help us characterize equipment such as cables, amplifiers, and most importantly our coupled resonator and atoms. A typical VNA measurement, which is explained in the input-output section below, measures the signal that passes through the sample and compares it to the signal sent into it. Furthermore, a VNA has the ability to measure both the phase and amplitude of a signal, unlike a scalar network analyzer. This allows us to have a complete characterization of the sample's behavior. We use a P9373A Keysight Streamline Series USB Vector Network Analyzer 14 GHz. The output port, or down-line, has a -30 dB (-20 dB + -10 dB) attached to reduce the microwave power. The VNA ports are connected to the cryosystem via standard microwave cables. The down-line is heat anchored to all stages of the cryostat. A -20 dB attenuator is attached on the 3 K stage to reduce thermal photons from the upper stages, similarly, a -10 dB and -20 dB attenuators are attached to the 500 mK and 50 mK stage, respectively. DC blocks are placed between the 3 K and 500 mK, as well as between the 500 mK and 50 mK to further reduce thermal noise and to thermally decouple the stages.

After the superconducting chip, the microwave now travels upward (up-line) towards the second port of the VNA. DC blocks are used to decouple the same stages similar to before. The microwave signal travels to a high electron mobility transistor (HEMT) amplifier provided by Low Noise Factory (LNF – LNC0.3_14A). The amplifier receives the small signal exiting the chip and amplifies it by 34 dB, which is measurable with the VNA. Once the up-line exits the 300 K stage, a room temperature amplifier (PAMTECH AFS3-02000400-06-10-4) again amplifies the signal to the VNA with +30 dB.

Both the down-line and up-line have microwave switches that allow the swapping between the time domain equipment and frequency equipment. The switch results in roughly 4 dB loss of signal.

5.5.2 Time domain microwave setup

IQ Mixing

Microwave IQ mixing is a technique used to modulate or demodulate microwave signals by mixing them with two components of a local oscillator: an in-phase (I) component and a quadrature (Q) component. These components are typically sine

and cosine waves at the same frequency but 90 degrees out of phase with each other. When a microwave signal, such as one at 3.7 GHz (which is the frequency we will use), is mixed with these components, the output consists of two frequencies: the sum and the difference of the input and local oscillator frequencies. The input signal $x(t) = A_x \cos(2\pi f_{\text{in}} t)$ is multiplied with the I and Q components $I(t) = A_I \cos(2\pi f_{\text{LO}} t)$ and $Q(t) = A_Q \sin(2\pi f_{\text{LO}} t)$, resulting in two output terms:

$$Y_I(t) = \frac{A_x A_I}{2} [\cos(2\pi(f_{\text{in}} - f_{\text{LO}})t) + \cos(2\pi(f_{\text{in}} + f_{\text{LO}})t)] \quad (5.1)$$

$$Y_Q(t) = \frac{A_x A_Q}{2} [\cos(2\pi(f_{\text{in}} - f_{\text{LO}})t) - \cos(2\pi(f_{\text{in}} + f_{\text{LO}})t)] \quad (5.2)$$

This produces the sum frequency $f_{\text{in}} + f_{\text{LO}}$ and the difference frequency $f_{\text{in}} - f_{\text{LO}}$, where the difference frequency is typically used for further analysis.

In hybrid quantum systems, we use microwave IQ mixing to control and manipulate quantum states, particularly for tasks like qubit initialization, state transitions, and measurement. The ability to mix signals allows precise control over the energy levels of the quantum system, enabling operations such as the generation of coherent superpositions and the coupling between qubits and resonators. For example, if the local oscillator frequency f_{LO} is set to 3.7 GHz, the difference frequency $f_{\text{IF}} = f_{\text{in}} - f_{\text{LO}}$ gives an intermediate frequency that can be used for easier detection and processing. This technique is vital in systems where precision control and manipulation of quantum states are required, such as in quantum information processing and quantum communication systems. A pictorial representation of the setup is seen below.

The experiment utilizes an arbitrary waveform generator (AWG, Tabor Electronics WX2182B model) to generate the I/Q signals, while a frequency source (Anritsu MG3692C) is used to generate the high-frequency signal. The mixing process itself is carried out using an IQ mixer (Marki IQ1545LMP).

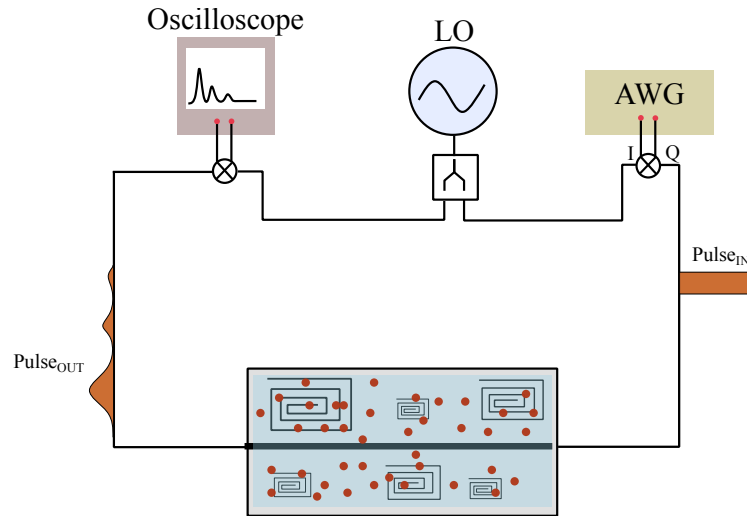


Figure 5.7 Schematic showing the microwave equipment used to perform the time domain measurements.

5.6 Superconducting chip

In earlier chapters, I developed an understanding of the atomic physics involved in the system, I will now dive into its complimentary counterpart of our hybrid quantum systems; the superconducting resonators. Over the past two decades, superconducting circuits and their technologies have made tremendous advancements in hopes of making a quantum computer [75, 76]. Fortunately, the push for their technological capabilities have also resulted in advancements in fundamental physics. Circuit QED (cQED) have proven to be a fruitful playground for exploring quantum information sciences, quantum optics, and have recently been proposed to search for physics beyond the standard model [77]. Here however, we use the most basic of their technologies; a resonator. The superconducting resonator is analogous to the classical harmonic oscillator which we will now go into.

5.6.1 Quantization of the superconducting circuit

Quantizing a superconducting circuit is conceptually similar to the electromagnetic field and a spring, where the energy of the system oscillates between the electric and magnetic fields. The capacitor stores charge, and as it discharges, it creates a current that in turn stores magnetic energy as flux. As the polarity between the capacitor

plates reverses, the magnetic flux draws the charge back. This process continues until the system dissipates its energy. In this system, the electric energy is contained in the capacitor (C), and the magnetic energy is stored in the inductance (L) of the material.

The energy stored in the capacitor is:

$$E_C = \frac{1}{2}CV^2 = \frac{Q^2}{2C} \quad (5.3)$$

where C is the capacitance, V is the voltage, and Q is the total charge. The energy stored in the inductor is

$$E_L = \frac{1}{2}LI^2 = \frac{\Phi^2}{2L} \quad (5.4)$$

where L is the inductance, I is the current, and Φ is the total magnetic flux. This can be expressed as

$$H = \frac{Q^2}{2C} + \frac{\Phi^2}{2L}. \quad (5.5)$$

This is similar to the Hamiltonian for a mass on a spring. The fundamental frequency of the system is:

$$\omega = \frac{1}{\sqrt{LC}}. \quad (5.6)$$

At this point, the charge Q and flux Φ can be treated as canonical variables (\hat{Q} and $\hat{\Phi}$), leading to the commutation relation:

$$[\hat{Q}, \hat{\Phi}] = i\hbar.$$

From here, we can define the creation and annihilation operators for the circuit, which follow similarly from equations (4.19) and (4.18):

$$\hat{Q} = \sqrt{\frac{\hbar C}{2L}}(a + a^\dagger) \quad (5.7)$$

and

$$\hat{\Phi} = -i\sqrt{\frac{\hbar L}{2C}}(a - a^\dagger). \quad (5.8)$$

Combining these, we arrive at the harmonic oscillator Hamiltonian:

$$H = \hbar\omega_{LC} \left(a^\dagger a + \frac{1}{2} \right). \quad (5.9)$$

In a sense, this result is expected, as an LC circuit is fundamentally a harmonic oscillator. However, it highlights how different systems can be described by the same

underlying physics. Using superconducting resonators as our cavity is akin to the physics of two mirrors, with the primary difference being the dimensionality of the system: the resonator is 2D, while the mirrors are 3D.

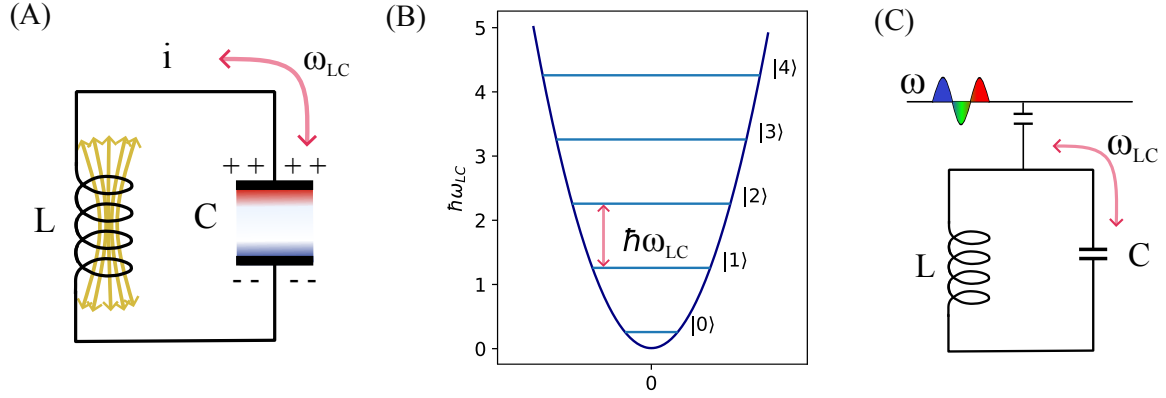


Figure 5.8 (A) Pictorial representation of a LC circuit. The oscillation (ω_{LC}) of the current (i) fluctuating back and forth between the capacitor pads (C) and the inductor (L). (B) Harmonic oscillator with discrete energy levels proportional to $n\omega_{LC}$

where n is the number of photons in the system. (C) The pictorial representation of our resonators. They couple to a through line which allows all frequencies to pass, however, the resonator only allows frequencies proportional to integer numbers of ω_{LC} into the LC circuit.

5.6.2 Input-output theory of a LC circuit

In the previous section, we described an idealized circuit, assuming no external driving forces or losses due to dissipation. In this section, we extend the analysis using the generalized master equation, which describes the time evolution of the system. This approach is similar to the one derived in Section 4.55. We begin with the equations of motion, in the Heisenberg picture, of the cavity field operator a .

$$\dot{a} = \frac{i}{\hbar}[a, H_c] - (\kappa_{ext} + \kappa_{int})a + \sqrt{\kappa_{ext}}c_{in} \quad (5.10)$$

where κ_{ext} is the external coupling between the through-line and the LC circuit and vice versa, κ_{int} is the internal dissipation rate of the LC circuit to the environment, c_{in} is an external probe tone with the form $c_{in} = c_0 e^{i\omega t}$, with a drive frequency ω . This type of system is considered to be Markovian, which requires the permanent loss of the dissipated energy to the system. We will assume once the photons have left either the resonator or through-line, they never return. The power output after the resonator

is then given by

$$c_{out} = c_{in} - \sqrt{\kappa_{ext}}a. \quad (5.11)$$

From here, we can now derive the steady state solution in the rotating frame of our drive frequency, ω , which reads as

$$\dot{a} = -(i\Delta + \kappa_{tot})a + \sqrt{\kappa_{ext}}c_0. \quad (5.12)$$

where $\Delta = \omega - \omega_c$ and the total dissipation rate, $\kappa_{tot} = \kappa_{ext} + \kappa_{int}$. The average field amplitude of the system is then

$$\langle a \rangle = \frac{\sqrt{\kappa_{ext}}}{\kappa_{tot} + i\Delta} c_0. \quad (5.13)$$

Due to the nature of our experiment, we are able to measure both the input and output signal, which we can use to determine the transmission parameter S_{21} as a function of frequency, resulting in

$$S_{21}(\omega) = \frac{\langle c_{out} \rangle}{\langle c_{in} \rangle} = 1 - \frac{\kappa_{ext}}{\kappa_{tot} + i\Delta} \quad (5.14)$$

However, what we measure with the VNA is $|S_{21}|^2$, which then results in

$$|S_{21}(\omega)|^2 = \left| \frac{\langle c_{out} \rangle}{\langle c_{in} \rangle} \right|^2 = 1 - \frac{\kappa_{ext}^2}{\kappa_{tot}^2 + \Delta^2} \quad (5.15)$$

5.6.3 Spiral resonator design

Initially, we used a coplanar waveguide resonator design for this experiment. This is a strip-line design where each end capacitively couples to the input and output microwave line. However, this design proved inefficient at coupling to the spins, as it was difficult to grow a densely doped crystal at small thicknesses. The problem arises because most of the electromagnetic field in a strip-line resonator extends roughly $2\mu\text{m}$ from the surface of the coplanar waveguide. This is also known as the mode volume of the electromagnetic circuit. However, there are numerous resonator designs that can effectively mitigate this issue. In particular, the spiral resonator design from Reference [78] demonstrated relatively homogeneous magnetic fields up to around $200\mu\text{m}$ extending from the surface of the chip. This, however, means we need to grow a relatively thick crystal to cover the entire mode volume of the resonator. We based our superconducting chips on this design.

As a reminder, the electromagnetic field inside the resonator, subject to boundary conditions, is given by

$$B_x(z, t) = B_0(a + a^\dagger) \sin(kz),$$

with $k = \frac{n\pi}{L}$. The fundamental mode, corresponding to $n = 1$ (also known as $\lambda/2$, as the cavity contains half a wavelength of radiation), is the primary resonance used in the experiments, while higher-order harmonics ($n > 1$) are neglected.

A quick and useful number to determine how 'good' a resonator is can be done by calculating the quality factor, which is defined as

$$Q = \frac{\omega}{\kappa} \quad (5.16)$$

where ω is the frequency of the fundamental resonance and κ represents the rate at which energy is lost. This factor quantifies the balance between stored and dissipated energy per cycle, characterizing how under damped or overdamped the resonator is. In a two-dimensional cavity design, the quality factor is primarily limited by radiation losses inherent to the geometry and dissipation at the conductor-substrate interface. In general there are two κ s, one describes the internal loss rate of the cavity (κ_{int}), and another that describes the loss with other external factors, (κ_{ext}), such as the environment.

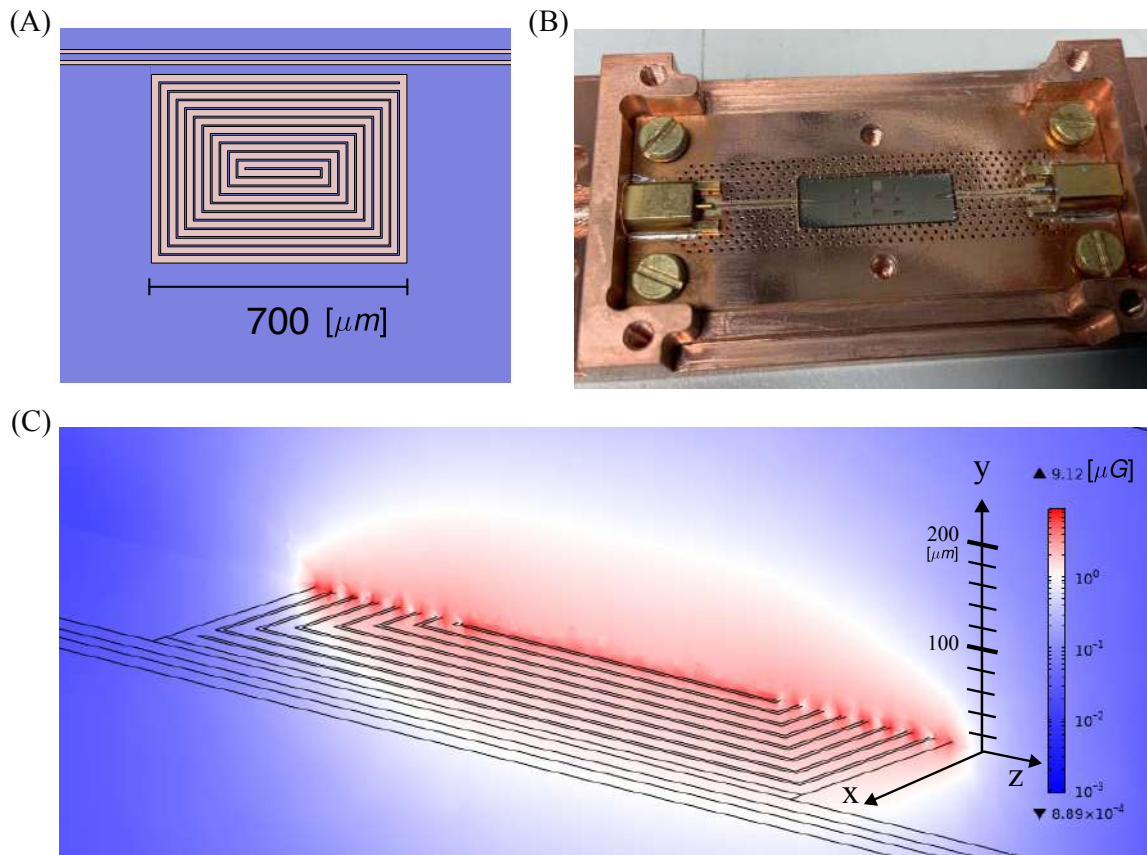


Figure 5.9 (A) Schematic of the 3.7 GHz resonator and through line. (B) Picture of the resonators (silver rectangle), microwave input and output couplers (horizontal lines connecting to the chip), and the copper sarcophagus. (C) Magnetic field distribution out of plane of the resonator. The average magnetic field the atoms see is approximately $3 \mu\text{G}$.

Our superconducting material is niobium (Nb), with a critical temperature $T_c = 9.3 \text{ K}$. The chip features a total of 9 physical resonators, each spaced roughly 1 GHz apart, within the frequency range of 1.7 GHz to 11 GHz. The resonator design is commonly referred to as a distributed-element resonator, meaning that both the capacitance and inductance are spread across the entire resonator, rather than being located at specific points. It is important to note that while these properties are distributed, the maximum electric field occurs at the ends of the resonator, while the maximum magnetic field is located at the center of the strip. We can simulate the magnetic field extension with the finite element simulation program COMSOL. As seen

in Figure 5.9 (C), the relatively homogeneous magnetic field extends approximately $150\text{ }\mu\text{m}$ out, with an average magnetic field strength on the order of $5\text{ }\mu\text{G}$.

The resonators capacitively couple to the through-line as seen in Figure 5.8 (C). With this setup, we expect to see a dip in the transmission spectrum as only the frequencies that fit the boundary conditions of the resonator couple to the through line. This design allows for efficient measurement of multiple resonators simultaneously so long as the frequencies do not overlap. This would be impossible with a coplanar waveguide. Each resonator was designed with a total coupling κ_T in the range of 200 kHz and Q close to 20,000. The primary resonator used in the experiment is fitted below.

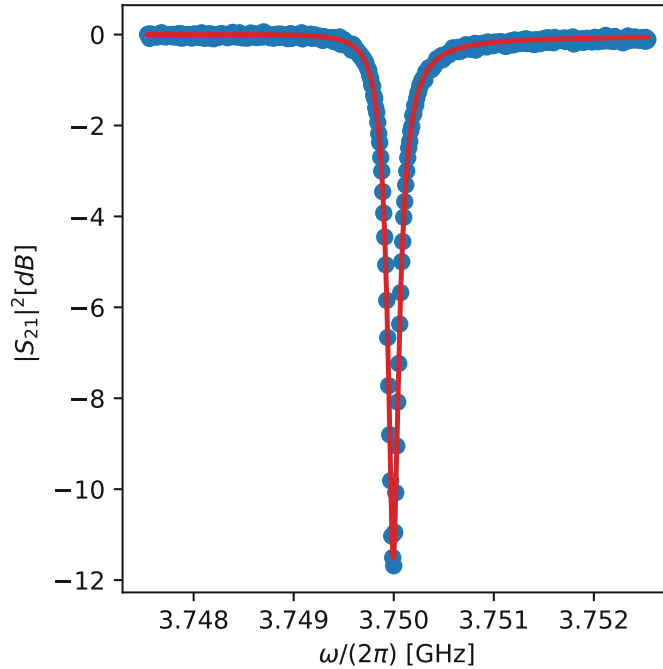


Figure 5.10 (A) Transmission spectrum of the 3.75 GHz resonator with no crystal. The bare resonator at $\omega_c/(2\pi) = 3.75\text{ GHz}$, $\kappa_{\text{ext}}/(2\pi) = 195\text{ kHz}$, $\kappa_{\text{int}}/(2\pi) = 70\text{ kHz}$, $Q \sim 14,000$.

If we place a single magnetic dipole in the center of the field, it couples at a rate of $\sim 5\text{ Hz}$, which is not possible to measure. As a solution, we couple to more spins!

5.6.4 Input output to a coupled system

We can extend Equation 5.17 to a coupled system, i.e. coupling to spins, requiring only a slight modification resulting in the following equation

$$|S_{21}(\omega)|^2 = \left| \frac{\langle c_{\text{out}} \rangle}{\langle c_{\text{in}} \rangle} \right|^2 = 1 - \frac{\kappa_{\text{ext}}^2}{i\Delta - \kappa_c + \frac{g_{\text{eff}}^2}{i(\omega_s - \omega_{\text{probe}}) - \gamma_{\text{spin}}}} \quad (5.17)$$

where ω_s is the frequency of the spin ensemble, γ_{spin} is the ensemble's linewidth, and of course g_{eff} is the effective coupling of the ensemble.

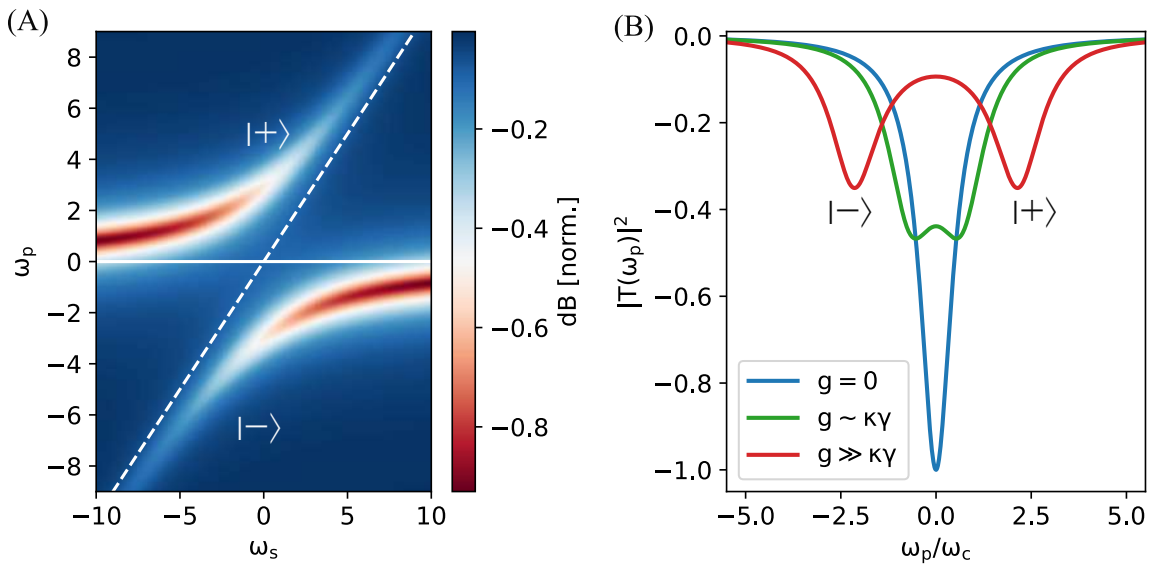


Figure 5.11 (A) Cavity transmission spectroscopy simulation of a strongly coupled cavity to a spin ensemble. The horizontal solid white line is the frequency of the resonator with zero coupling. The dashed vertical white line is the center frequency of the spins as a function of magnetic field. (B) Transmission spectrum with three different couplings illustrating no coupling, weak coupling, and strong coupling of spins to the cavity.

As a point of interest, we can characterize the coupling regime between the spins and the resonator:

- **Weak coupling:** $g_{\text{eff}} < \kappa + \gamma$. The interaction rate between the spin and the cavity is smaller than the dissipation rate of the cavity as well as the atomic linewidth. As a result, photons leave the cavity at a rate higher than the spin-photon interaction rate. In this regime, the cavity broadens but still maintains a single peak or dip in transmission.

- **Strong coupling:** $g_{\text{eff}} \geq \kappa + \gamma$. The interaction rate between the spin and the photon is larger than the dissipation rate of the cavity as well as the atomic linewidth. This means that the spin-photon interaction occurs faster than dissipation out of the cavity. In this regime, one observes two peaks or dips in transmission, with a splitting larger than the full width at half maximum (FWHM) of the cavity. These two peaks correspond to the $|+\rangle$ and $|-\rangle$ hybridized spin-photon states.

In Figure 5.11 (A), we see a transmission scan as the spin transition is crossed over the resonator. A clear signal that one is in the strong coupling regime is an avoided crossing ($\omega_s = \omega_c = 0$) where the spins and the cavity are on resonance. In Figure 5.11 (B), we can see two distinct regimes, strongly coupled in red, weakly in green, and the bare resonator in blue.

Chapter 6

Crystal growth and characterization

This chapter discusses the process of growing the doped cryogenic crystal and characterizing its growth optically and through microwave resonator measurements. I will show crystals of both Rb and Na as impurities, and both p-H₂ and Ne as the host matrices. Additionally, I will also highlight the difference in absorption between 3 K and 100 mK.

6.1 Preparation

Before the crystal growing process, the cryosystem is cooled to its base temperature and all gas tubes have been pumped down to vacuum pressure. We then begin by raising the temperature of second copper tube, as shown in Figure 5.2 (C), which is connected to the second stage of the cryostat and has a base temperature of 6 K. The elevated temperature is regulated to just above the melting point of the gas being used. For p-H₂, the temperature is maintained at 13.8 K, while for Ne, it is held at 27 K. Once the gas tank is opened, the needle valve is gradually opened to a pressure range of 5-10 mbar, which is monitored by the pressure gauge located immediately after the needle valve. The gas quickly percolates through the first copper tube and reaches the second one. A schematic representation of this setup is shown in Figure 6.1 (A).

The time it takes for the gas to enter and exit the nozzle of the second tube varies, typically ranging from 1-2 hours at the specified pressures and temperatures. This duration can change depending on the desired growth rate. The exit time of the gas can be predicted by monitoring the temperature change of the second copper tube. Initially, the gas enters the tube at around 30 K, and as it flows through, it dissipates heat to the oxide. A gradual increase in temperature is observed as more gas enters the tube. At a certain point, the temperature increase levels off, even though the gas

continues to fill the tube. After a brief waiting period, the temperature drops rapidly, signaling the exit of the gas. This flattening of the temperature followed by a sharp decrease is characteristic of a phase transition, likely from liquid to gas, which was observed for both p-H₂ and Ne. The temperature as a function of time is shown in Figure 6.1 (B).

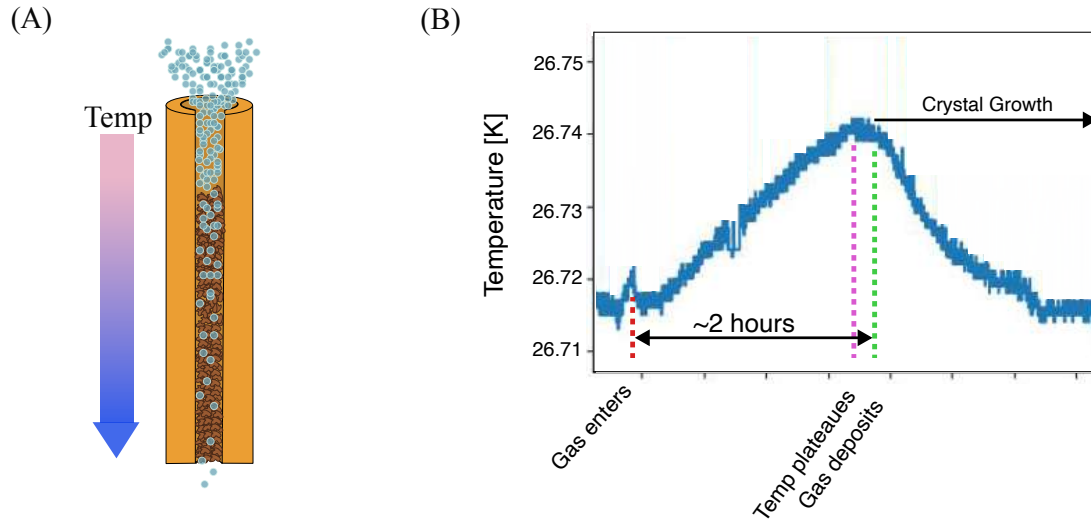


Figure 6.1 (A) Pictorial representation of the cryogenic gas percolating through the iron oxide. As the gas migrates through the copper tube, it reduces in temperature. (B) Temperature as a function of time of the second copper tube as the gas migrates from the top to the nozzle. There is an increase in temperature as the gas enters the second tube due to the difference in the temperatures between the gas and the tube. After the temperature plateaus, the crystal begins to deposit.

It takes approximately 2 hour for the gas to start condensing on the resonator, so we simultaneously begin heating the atomic oven to ensure the impurities are thermalized to their required temperatures, resulting in a constant atomic flux. For Rb, we set up atomic absorption spectroscopy to determine the atomic flux leaving the oven. A similar setup could have been used for Na, but we did not have a suitable laser for this, but the procedure would be identical. Once the oven reaches the desired temperature, we perform absorption spectroscopy on the Rb exiting the nozzle. We found that after 30 min, the flux reached equilibrium and remained constant. The typical Rb flux was determined to be approximately $10^{18} \frac{\text{atoms}}{\text{sec}}$ at the nozzle which would translate to approximately $10^{15} \frac{\text{atoms}}{\text{sec}}$ at the surface of the resonator. The atomic flux exhibits a natural divergence as the atoms propagate outward within a defined solid angle. Consequently, the flux density decreases with distance from the source, following a

$1/r^2$ dependence. This reduction arises because the emitted atoms distribute over an expanding area as they travel. The degree of divergence is determined by the initial emission conditions, including factors such as collimation and the presence of apertures, which can constrain the solid angle of propagation. Similar fluxes are expected for Na.

Additional preparations are done in regards to the superconducting chip's base temperature. Due to the flexibility of the ADR, crystal growth can be done at temperatures ranging from 50 mK to ~ 3 K. There are limitations though, as growing at 50 mK can only support an extremely thin crystal as the cooling power is almost zero, while for example 2.5 K can be maintained for hours. Typical cooldown times of the ADR from 3 K to 50 mK is 1.5 hours, and depending on the regulation temperature, an additional 30 minutes can be added. The ADR ramps its temperature up or down at a rate of 100 mK/min.

6.2 Deposition

When we reach the final stages of gas preparation, i.e., the plateauing of the copper tube's temperature, we push our oven forward towards the shutter and wait. Once the gas (Ne or p-H₂ for example) begins condensing on the superconducting resonator, a shift in its frequency can be observed. This *downward* shift is caused by the introduction of an additional dielectric material that the electromagnetic field interacts with. The original frequency of the resonator $\omega = \frac{1}{\sqrt{LC}}$ is now modified as the inductance and capacitance include contributions from the host matrix. We can simulate this total shift using Sonnet Software by incrementally increasing a layer of Ne on top of the circuit. It is assumed that the entire circuit is covered with neon. The dielectric constants of p-H₂ and Ne are 1.25 [79] and 1.244 [80], respectively. Figure 6.2 (A) shows a simulation of a neon crystal as a function of thickness.

In general, it is advantageous to create a thin layer of the host matrix before adding the impurities. If the impurities were introduced before the gas had time to condense, the quality factor of the cavity would decrease dramatically as metallic clusters would begin to form on the surface. Typically, crystals were grown after approximately a 150 kHz shift in the resonator's frequency. This shift corresponds to an approximately 200 nm thick crystal.

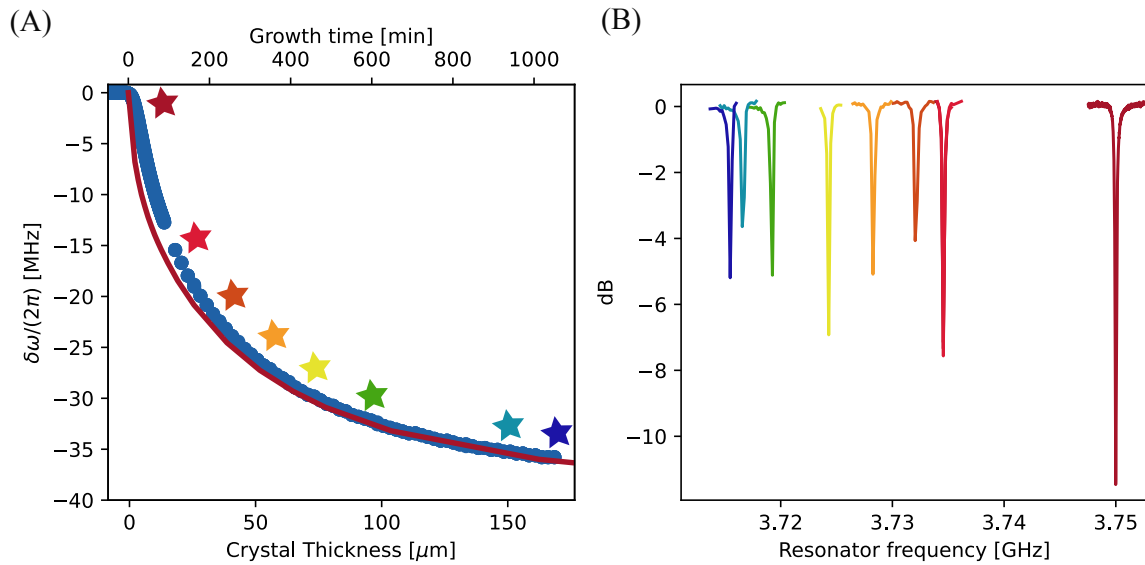


Figure 6.2 (A) Shifting of the resonator's fundamental frequency (blue dots) as the gas solidifies on the surface as a function of time. Red line is the expected shift from the Sonnet simulations as a function of matrix thickness. (B) Shifting of the resonator frequency while the deposition of the matrix. Difference in amplitude is due to the limited number of points while scanning the transmission.

Depending on the desired crystal thickness, the lifetime at the regulated ADR temperature might not be sufficient for the entire crystal to cover the electromagnetic field of the resonator, which was typically the case in our experiments. The crystals typically had 2 hours at the regulated temperature (2.5 K), and the remaining growth was done at the base temperature of the pulse tube (2.9 K). Once the crystal filled the mode volume of the resonator, we pulled the oven back, closed the shutter, and grew an additional 2-5 μm thick layer of the pure cryogenic gas crystal, effectively "sandwiching" our doped crystal. This additional layer allows for the evaporation of the crystal without the loss of any impurities and acts as a buffer for unwanted contaminants that could otherwise affect the doped section.

Completing the growth then requires the shutdown of all heaters (tube and oven) and bringing the system into thermal equilibrium with the cryosystem. Maintaining the cryostat at the lowest possible temperatures was done to limit the possibility of diffusion or sublimation.

6.3 Optical characterization

Once the doped crystal is grown, it is advantageous to optically characterize the sample. By performing broadband absorption spectroscopy on the doped crystal, we can determine the number of impurities by calculating the optical depth (OD).

$$\text{OD} = n \cdot l \cdot \sigma \quad (6.1)$$

Where OD is the optical depth, n is the density of atoms, l is the length of the atomic medium, and σ is the absorption cross-section. The calculation was done similarly to Reference [81]. The cross-sections for Rb and Na using in this thesis are $\sigma_{\text{Rb}} = 2.3 \times 10^{-19} \text{m}^2$ and $\sigma_{\text{Na}} = 1.98 \times 10^{-19} \text{m}^2$. Moreover, applying white light to the crystal has shown to cause a dramatic alteration in the OD. Colloquially, it is called *bleaching*, but one can also think of it as optically annealing. To bleach, we use white light, which is composed of two LEDs (447 nm and 517 nm peak wavelength) and a tungsten lamp, coupled into an optical fiber that enters the cryostat. The end of the fiber is attached to the copper box at a 45° angle to the substrate. Bleaching is observed in our system at temperatures below 2 K, where the power emitted from the end of the fiber is $\sim 90 \mu\text{W}$ and illuminates the crystal for roughly 15 seconds. Reducing the substrate temperature from 3 K to 50 mK alone did not change the optical spectrum of the doped crystal, only after we apply white light a dramatic change in the OD occurs and we observe an increase in OD. We noticed no significant changes in the OD after bleaching at 50 mK for up to 12 hours, which is the limit of our ADR capabilities. Once the substrate temperature reaches 3 K, the system returns to the original 3 K spectrum. The effect of bleaching on our microwave spectrum will be addressed in the Appendix. Below are optical spectra of both Rb and Na in different host matrices and at different temperatures.

Rubidium in solid p-H₂ and Ne

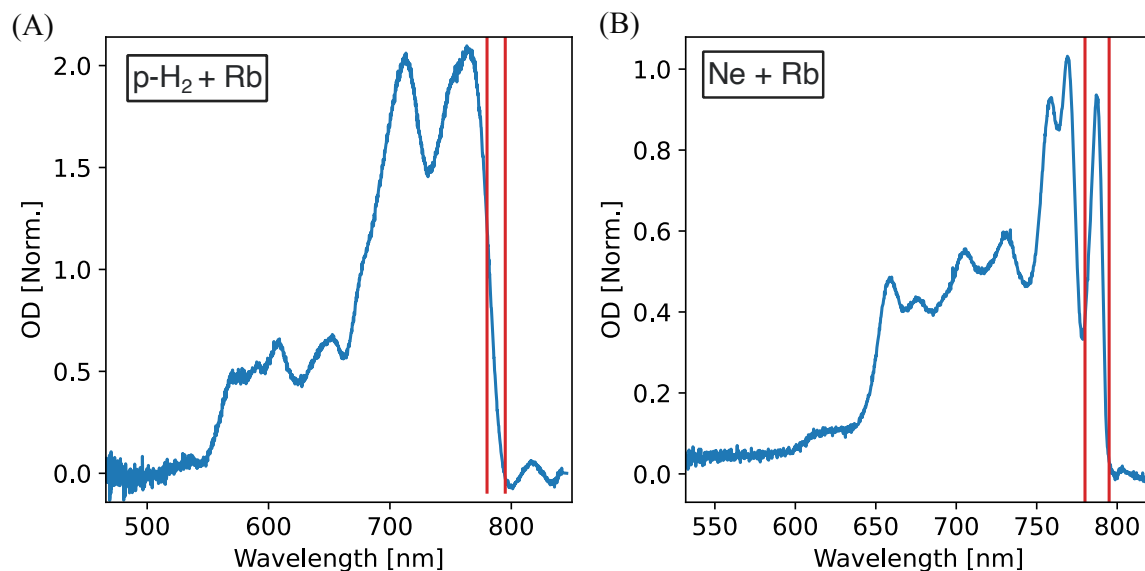


Figure 6.3 (A) Optical spectra of Rb in a p-H₂ crystal. Both crystals are approximately 100 μm thick. Solid red vertical lines indicate the D1 and D2 transitions of the free atom. (B) Similar to the first plot, however the Rb is in a solid Ne matrix. Solid red lines are the D1 and D2 lines.

Unfortunately, Rb in p-H₂ was not optically inspected at 100 mK and Na was not deposited in p-H₂. Both of these would be interesting for future experiments. The figures regarding the purity of p-H₂ can be found in the Appendix 1.

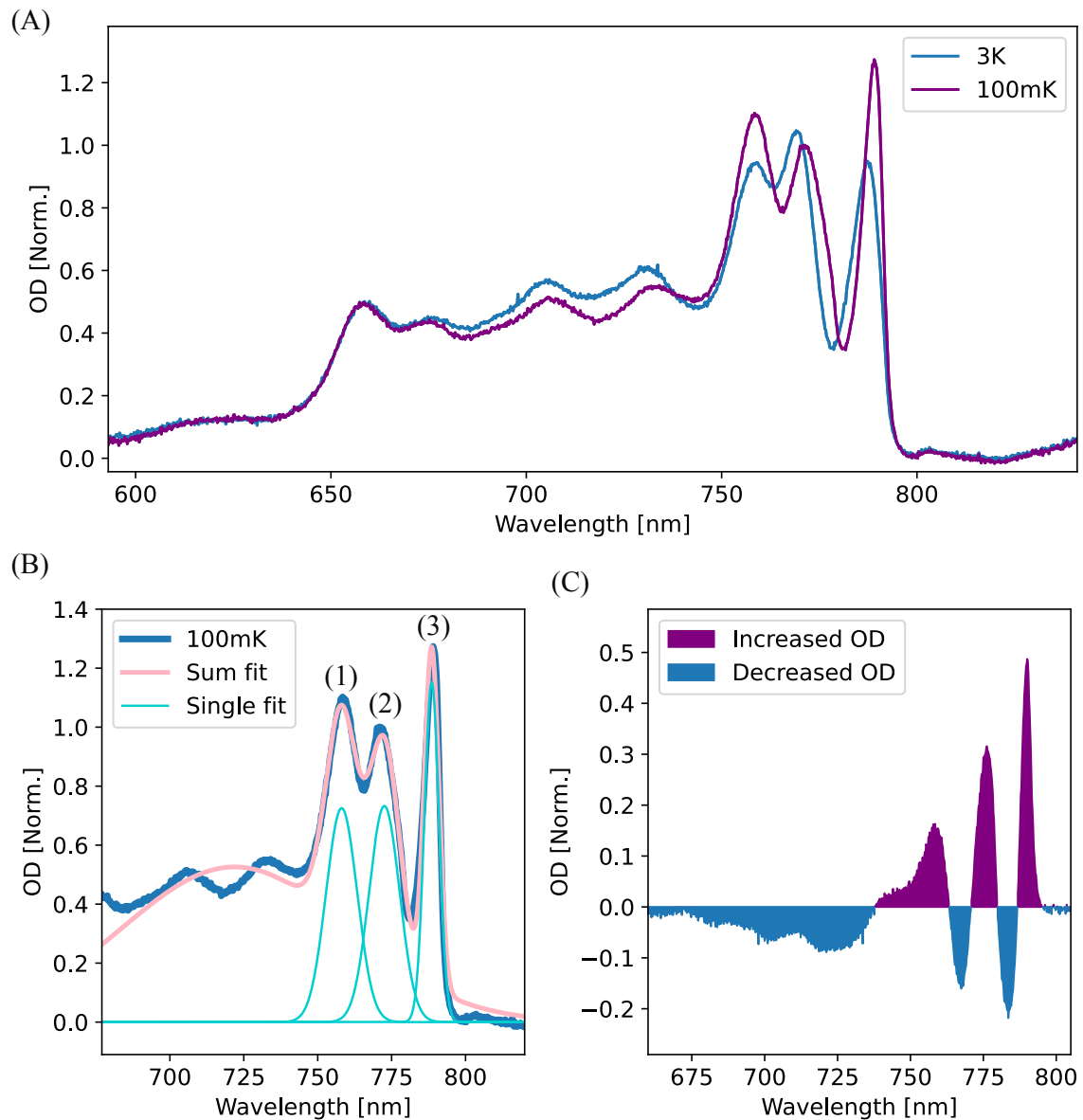


Figure 6.4 (A) OD of a Ne crystal doped with Rb. Crystal is approximately $100\ \mu\text{m}$ thick. Plotted are ODs taken at two different temperatures, 3 K and at 100 mK. (B) Fitting of the Rb peaks at 100 mK. The solid pink line is the combination of the three peaks as well as a wide gaussian "background" attributed from the left hand side peaks. (C) The difference of the total OD as a function of wavelength between the 3 K and 100 mK spectrum.

Parameter	Temperature	Peak 1	Peak 2	Peak 3
Position	3K	758.0	769.9	786.7
	100mK	758.0	772.5	788.5
Linewidth FWHM	3K	10.32	8.88	6.98
	100mK	10.51	10.28	4.92
OD	3K	0.58	0.85	0.73
	100mK	0.732	0.73	1.15

Table 6.1 Summary of positions, linewidth (FWHM), and optical density (OD) for three peaks at 3 K and 100 mK.

Sodium in solid Ne

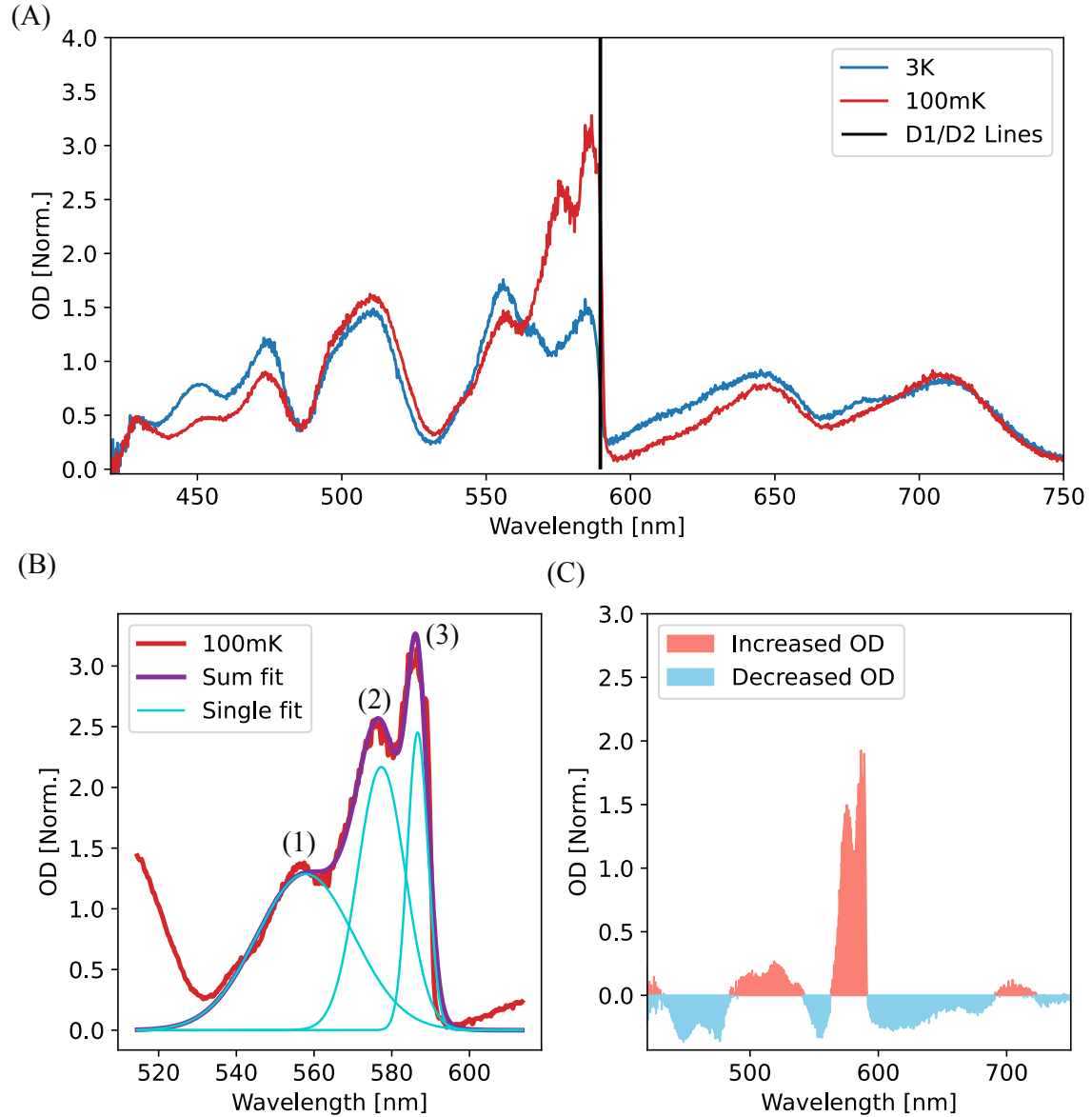


Figure 6.5 (A) OD of a Ne crystal doped with Na. Plotted are ODs taken at two different temperatures, 3 K and at 100 mK. Crystal is approximately $200\ \mu\text{m}$ thick. (B) Fitting of the Na peaks at 100 mK. The solid purple line is the combination of the three peaks. (C) The difference of the total OD as a function of wavelength between the 3 K and 100 mK spectrum.

Parameter	Temperature	Peak 1	Peak 2	Peak 3
Position	3K	556.34	-	582.45
	100mK	557.90	577.44	586.77
Linewidth FWHM	3K	10.29	-	6.46
	100mK	12.50	6.10	2.63
OD	3K	1.54	-	1.34
	100mK	1.29	2.17	2.45

Table 6.2 Summary of positions, linewidth (FWHM), and optical density (OD) for three peaks at 3 K and 100 mK. Missing values ('-') indicate that the second peak at 3 K could not be properly fitted.

Chapter 7

Microwave Spectroscopy and Time Resolved Measurements

To achieve coherent coupling between atomic spins and a superconducting microwave cavity, it is essential to prepare the atomic ensemble in a well-defined quantum state. At room temperature, thermal energy vastly exceeds the hyperfine splitting of alkali atoms, resulting in an effectively unpolarized distribution of spin states.

Cooling the system to 3 K using a pulse tube cryostat ensures that our alkali dopants are trapped in a solid noble gas matrix, but it does not fully polarize their spin states. At this temperature, the hyperfine states are nearly equally populated, with sodium (^{23}Na) atoms, for example, having an approximately 50/50 distribution between $|F = 1\rangle$ and $|F = 2\rangle$. To achieve a well-defined initial state, we further cool the system using the ADR, which lowers the temperature to 50 mK. At this temperature, the atomic ensemble thermalizes to the lower hyperfine ground state $|F = 1\rangle$, as the energy splitting between hyperfine levels becomes large compared to the available thermal energy.

Following this initialization, we apply a static magnetic field to lift the degeneracy of the hyperfine sublevels via the Zeeman effect. This field not only defines a tunable two-level system but also enhances the polarization of the ensemble by energetically favoring the lowest-energy m_F sublevel. As a result, we obtain a well-defined spin state that is suitable for coherent coupling to the superconducting cavity.

In addition to cooling the atomic ensemble, we also cool the superconducting resonator to reduce thermal photon occupation. At temperatures around 3 K, the resonator is populated due to black body radiation, leading to an undesirable thermal photon population at the resonator's frequency. This photon occupation can interfere with the desired spin-photon interactions and our readout. However, when the

temperature is lowered to 50 mK using, the thermal photon occupation number in the resonator drops significantly, and the photon number becomes much smaller than one. For GHz frequency resonators, this corresponds to a situation where the thermal photon occupation is effectively near zero, minimizing unwanted excitations and allowing the system to enter a regime where quantum effects dominate the spin-photon interactions. This low photon occupation is crucial for maintaining the coherence of the system and enabling strong coupling between the atomic ensemble and the superconducting resonator.

In the following sections, we discuss the effects of temperature and magnetic fields on the hyperfine structure, which enable the formation of a controllable spin-photon interaction. We then demonstrate the strong coupling of an alkali spin ensemble to a superconducting resonator, followed by the characterization of the system's coherence properties through measurements of T_1 and T_2 times.

7.1 Thermal photon occupation in the cavity

To minimize the thermal occupation of microwave photons in the resonator, we lower the temperature well below its characteristic frequency. Essentially, this reduces the bath temperature beneath the resonator's frequency, corresponding to the energy

$$E = hf = \frac{hc}{\lambda}. \quad (7.1)$$

We can calculate the thermal occupation for each of our resonators with the Bose-Einstein statistics, where the average occupation number n for a frequency f of a degeneracy g at a given temperature T is

$$\bar{n}_i = \frac{g_i}{e^{\frac{hf_i}{k_B T}} - 1}. \quad (7.2)$$

For our resonators, the degeneracy is 1, and k_B and \hbar represent the Boltzmann constant and Planck's constant, respectively. The superconducting chip has 9 fundamental frequencies, ranging from 1.77 GHz to 11.9 GHz. At a temperature of 50 mK, the photon occupation number for the 1.77 GHz resonator is approximately 0.224, while for the 11.9 GHz resonator, it is 1.10×10^{-5} . The resonator which is primarily used below, operating at 3.75 GHz, has an occupation number of 0.029.

7.2 Zeeman splitting in an external magnetic field

The hyperfine interaction arises from the coupling between the nuclear spin I and the electron spin S , described by the Hamiltonian

$$H_{\text{hf}} = A \mathbf{I} \cdot \mathbf{S}, \quad (7.3)$$

where A is the hyperfine coupling constant. This interaction splits the ground state into two levels characterized by the total angular momentum quantum number $F = I \pm 1/2$. However, at zero magnetic field, the m_F sublevels within each hyperfine manifold remain degenerate. To define a tunable two-level system, we apply an external magnetic field to lift this degeneracy via the Zeeman effect.

In the presence of a magnetic field B , the total Hamiltonian includes the Zeeman interaction,

$$H = A \mathbf{I} \cdot \mathbf{S} + g_S \mu_B B S_z + g_I \mu_N B I_z. \quad (7.4)$$

In the weak-field regime, the Zeeman shift is linear, given by

$$\Delta E \approx m_F g_F \mu_B B, \quad (7.5)$$

where g_F is the Landé g-factor. However, in the intermediate-field regime, where the Zeeman energy is comparable to the hyperfine interaction, the energy levels are given by the Breit-Rabi formula:

$$E(F = I \pm 1/2, m_F) = -\frac{A}{2(2I + 1)} + g_I \mu_N B m_F \pm \frac{A}{2} \sqrt{1 + \frac{4m_F x}{(2I + 1)} + x^2}, \quad (7.6)$$

where

$$x = \frac{(g_S \mu_B - g_I \mu_N) B}{A}. \quad (7.7)$$

By selecting specific transitions within this level structure, we define a two-level system whose transition frequency is tunable with the applied magnetic field. Zeeman splittings of the ground state hyperfine levels of both Rb and Na are shown below in Figure 7.1 and Figure 7.2.

7.3 Spin population of the hyperfine levels

Now that we have achieved the desired temperature and applied a magnetic field, we can calculate the population distribution of the atomic ensemble across the hyperfine levels. As mentioned earlier, cooling the system to 50 mK thermally populates the hyperfine ground state of the atoms, with nearly 95% of the population residing in the lower F -state for isotopes such as ^{85}Rb , ^{87}Rb , and ^{23}Na . The magnetic field further splits the degenerate hyperfine levels and helps polarize the atomic ensemble.

To determine the population of atoms in each hyperfine level, we use the Maxwell-Boltzmann distribution, which describes the statistical distribution of particles over available energy states at a given temperature. For each hyperfine level i , the population $\langle N_i \rangle$ can be written as:

$$\langle N_i \rangle = \frac{g_i}{e^{E_i/k_b T}} = \frac{N}{Z} g_i e^{E_i/k_b T}, \quad (7.8)$$

where g_i is the degeneracy factor, which accounts for the number of available sublevels in each hyperfine manifold, E_i is the energy of the i -th hyperfine level, and T is the temperature. The partition function Z is the sum over all possible energy states:

$$Z = \sum_i g_i e^{-E_i/k_b T}. \quad (7.9)$$

In the case of alkali atoms, the degeneracy g_i corresponds to the number of accessible m_F states within each hyperfine manifold. At zero magnetic field, the population is evenly distributed among these states. Upon applying a magnetic field, the degeneracy is modified, and the population distribution shifts accordingly, with higher energy states being less populated.

The resulting population distribution, as a function of temperature and magnetic field, determines the number of atoms in each hyperfine level, which in turn affects the effective coupling of the atomic ensemble to the superconducting resonator. The populations can be seen in Figure 7.1 and Figure 7.2 for Rb and Na, respectively.

7.3.1 Spin population of ^{85}Rb and ^{87}Rb

Our initial attempt to couple atoms to a superconducting resonator included both isotopes of Rb. Naturally, ^{85}Rb is more abundant, comprising approximately 70% of a typical rubidium sample, while ^{87}Rb accounts for the remaining 30%. At 50 mK and under a reasonable applied magnetic field, this abundance difference results in roughly

30% more ^{85}Rb atoms compared to ^{87}Rb , making it the more prevalent species in our system.

However, as shown in Figure 7.1, ^{85}Rb has a larger ground state hyperfine manifold, which distributes the atomic population across more states. This broader distribution reduces the number of atoms in the $|F, m_F\rangle = |2, 2\rangle$ state, effectively decreasing the population available for coupling. In contrast, ^{87}Rb has a smaller hyperfine manifold, concentrating more atoms into a given state, but its lower natural abundance ultimately limits the total number of spins that can participate in the interaction.

Considering both the natural abundance and the hyperfine state distribution, we estimate that ^{85}Rb should provide a factor of approximately 1.38 times spins in the $|F, m_F\rangle = |2, 2\rangle$ state compared to ^{87}Rb $|F, m_F\rangle = |1, 1\rangle$.

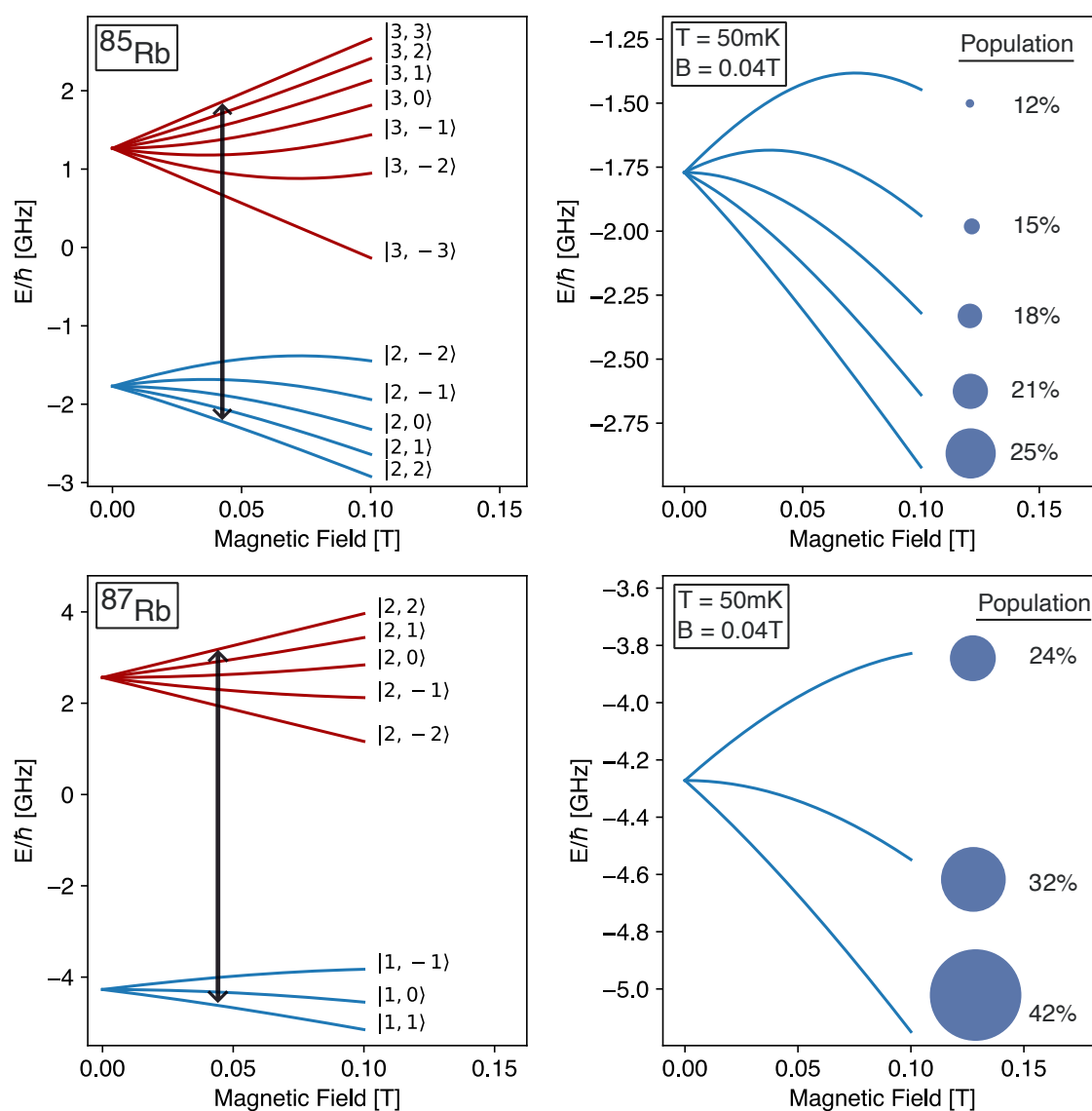


Figure 7.1 (LHS) Zeeman splittings of the ground state hyperfine manifolds of both ^{85}Rb and ^{87}Rb and the transition coupled to the superconducting resonator (black arrow). (RHS) Population percentage of a thermally and magnetically polarized atom at our operating fields and temperatures.

7.3.2 Spin population of ^{23}Na

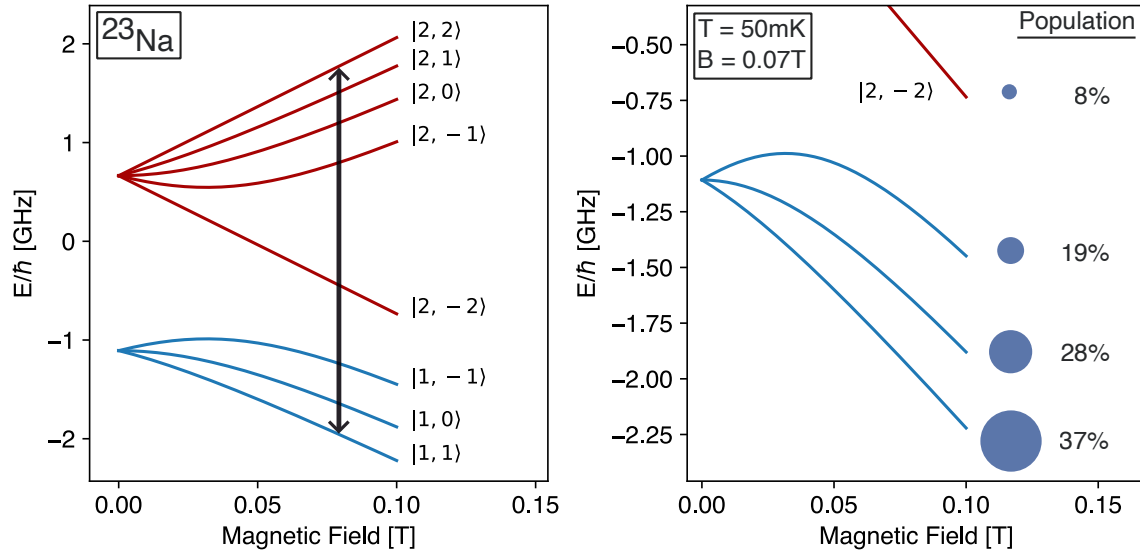


Figure 7.2 (A) Zeeman splittings of the ground state hyperfine manifolds ^{23}Na and the transition coupled to the superconducting resonator (black arrow). (B) Population percentage of a thermally and magnetically polarized atom at our operating fields and temperatures.

Due to the presence of two naturally occurring species of rubidium and the "large" hyperfine manifold of ^{85}Rb , we began exploring alternative atoms, which led us to Na. Atomic sodium has a single stable isotope and a reduced hyperfine ground state manifold, both of which contribute to an improved coupling to the superconducting resonator. The hyperfine levels and polarization of Na are shown in Figure 7.2.

Once our spins have had sufficient time to thermalize, a process that will be discussed in more detail later in this chapter, we are then ready to perform microwave measurements on the spins.

7.4 Coupling of spins to a resonator

7.4.1 Preparation

This section presents a detailed discussion of coupling both Rb species and Na to a superconducting resonator. As will be shown, we were only able to achieve strong coupling with Na. Although Rb did not reach strong coupling, we were still able to

observe weak interactions between the spin ensemble and the cavity, which is noteworthy. The "unsuccessful" Rb measurements ultimately guided us to the "successful" Na results. Additionally, I will discuss the importance of optical bleaching at 50 mK with respect to microwave coupling. The reason why bleaching at mK temperatures is required remains unclear, but I will propose some possible explanations in the conclusion. For both the Rb and Na, the following procedure was used to measure the coupling of the spins.

1. Tune atoms magnetically to resonator frequency
2. Begin ADR cool down procedure
3. Optically bleach
4. Turn on microwave amplifier
5. Begin measurement

The steps outlined above serve two main objectives: reducing the temperature increase of the cryostat's second stage during the cool down process and maximizing the lifetime of the ADR while at low temperatures. An increased temperature can lead to the annealing or possible melting of the crystal, while maximizing the ADR lifetime allows for extended measurement times at mK temperatures. Taking proper care to manage thermal heating is crucial, which is why I have emphasized the attention to detail in this section. Tuning the atoms before cooling the ADR (step 1) minimizes heating and extends the lifetime of the 50 mK stage due to the reduction of Eddy currents generated by ramping the coils. Following this, the ADR cool down procedure begins (step 2). This process causes an unavoidable temperature increase of around 0.2 K in the second stage as the 4 T magnet reduces its current. Once the system reaches its base temperature of 50 mK, we bleach the crystal for an appropriate amount of time (step 3), simultaneously taking spectra. To perform the microwave measurements, we turn on the microwave amplifier (step 4), which causes an additional increase of approximately 0.3 K in the second stage. Finally, we begin the microwave experiments by tuning the magnetic field causing the atoms to interact with the resonator (step 5). Since the majority of the magnetic field tuning was performed earlier in step 1, the heat generated is negligible. Typical VNA powers are -35 dB before any attenuation.

7.4.2 Coupling of rubidium

Once the crystal has been cooled and optically bleached, we perform microwave spectroscopy by sweeping the magnetic field to tune the atomic transition frequency across the resonator frequency. As a reminder, when the ensemble's transition energy approaches that of the resonator ($\omega_a \sim \omega_c$), hybridization between the spin ensemble

and the cavity results in a broadening of the transmission spectrum, and if strong enough, a splitting, as discussed in Chapter 5 and shown in Figure 5.11.

With this in mind, we now characterize the spin ensemble, focusing on the crystal from Figure 7.3. Based on optical spectroscopy, the estimated rubidium atom density (including both ^{85}Rb and ^{87}Rb) in this crystal is approximately $6 \times 10^{17} \text{cm}^{-3}$. Considering the relative isotope abundance, the number of hyperfine levels, and the resonator's mode volume, we expect an effective coupling strength (g_{eff}) of approximately 4 MHz for the ^{85}Rb $|F, m_f\rangle = |2, 2\rangle \rightarrow |3, 3\rangle$ transition.

In Figure 7.3 (B), we observe clear coupling of ^{85}Rb to the superconducting resonator. Unexpectedly, the measured coupling strength is vastly lower than expected, with $g_{\text{eff}} \approx 150 \text{ kHz}$. This discrepancy may be attributed to three factors: the actual atomic density could be lower than estimated, the impurity distribution within the crystal may be less uniform than assumed, or the dipole-dipole broadening is too large, which will be discussed below. We made efforts to reduce the density in order to reduce the linewidth but unfortunately we were not able to reach strong coupling. At 405 G, the Zeeman-tuned hyperfine transition frequency of ^{85}Rb in the crystal is shifted by approximately 7.38% from its free-atom value.

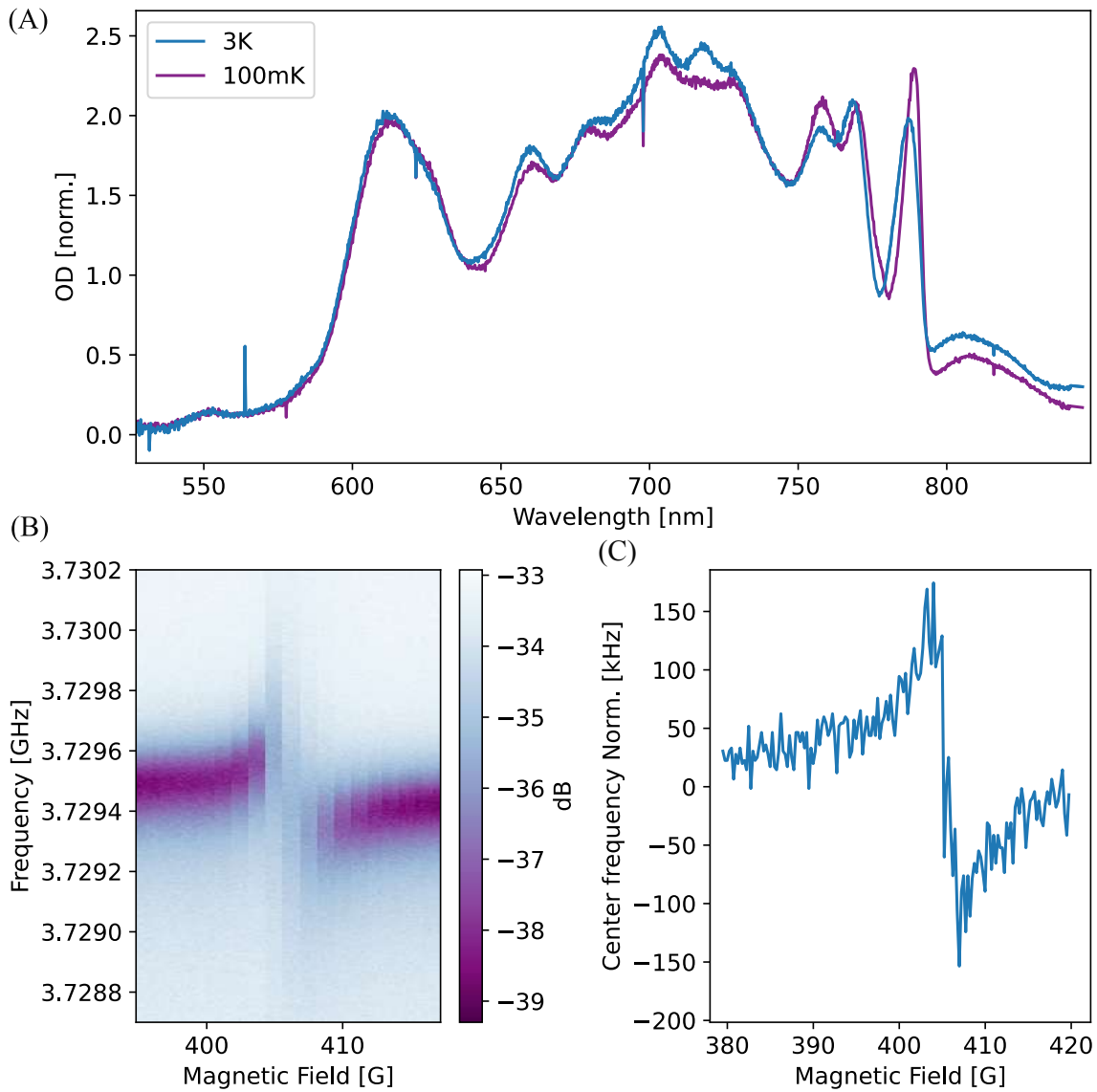


Figure 7.3 (A) Optical spectroscopy of a Rb doped Ne crystal at both 3 and 100 mK. Crystal is approximately $100\ \mu\text{m}$ thick. (B) Microwave spectroscopy of crystal from optical plot above. The resonator couples is coupling to the $|F, m_f\rangle = |2, 2\rangle \rightarrow |3, 3\rangle$ transition. (C) Normalized fit of the resonator's center frequency as the magnetic field sweeps the atomic transition across the resonator.

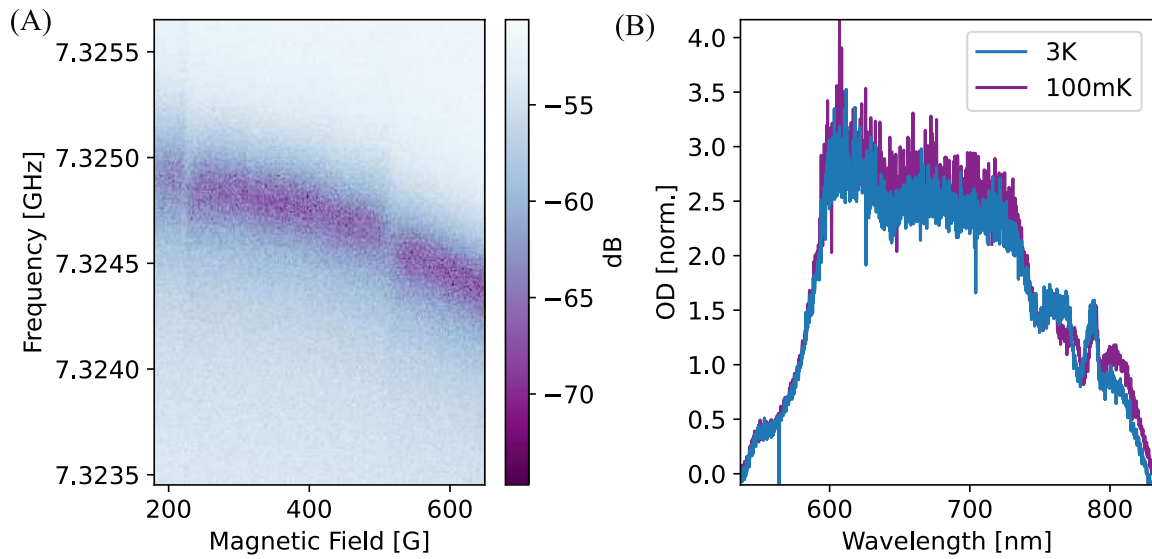


Figure 7.4 (A) Microwave spectroscopy as a function of applied magnetic field. We notice two lines at 200 G and 515 G, these are attributed to the hyperfine coupling states $|F, m_f\rangle = |1, 1\rangle \rightarrow |2, 2\rangle$ and $|F, m_f\rangle = |1, 1\rangle \rightarrow |2, 0\rangle$. $|F, m_f\rangle = |1, 1\rangle \rightarrow |2, 1\rangle$ is too weak to see. (B) OD of the Rb doped Ne crystal used for the magnetic field sweep. Crystal is approximately $100\ \mu\text{m}$ thick.

Similarly, we measured the coupling of ^{87}Rb to the cavity. In Figure 7.4 (A), we observe two distinct crossings at 225 G and 515 G, corresponding to the transitions $|F, m_f\rangle = |1, 1\rangle \rightarrow |2, 2\rangle$ and $|F, m_f\rangle = |1, 1\rangle \rightarrow |2, 0\rangle$, respectively. It is unclear why we do not see the $|F, m_f\rangle = |1, 1\rangle \rightarrow |2, 1\rangle$ transition at 319 G. Relative to their free-atom transition frequencies at these fields, these transitions exhibit frequency shifts of -0.107% and -0.02%. Compared to ^{85}Rb , ^{87}Rb shows a smaller shift in the opposite direction.

Unfortunately, we did not measure both ^{85}Rb and ^{87}Rb within the same crystal, as evidenced by the differing optical depths in Figure 7.3 (A) and Figure 7.4 (B). This was an unfortunate oversight. On the positive side, though we did not achieve strong coupling, we successfully coupled both isotopes of Rb to a superconducting resonator nonetheless.

7.4.3 Broadening of the spin ensemble

To try and understand our system better, I examine the dipole-dipole interaction within the spin system, focusing on Rb-Rb interactions. To simulate this interaction, I model a single Rb atom interacting with a "bath" of additional Rb atoms, where the

interaction is mediated by the dipole-dipole force. The corresponding Hamiltonian is given by:

$$\begin{aligned} H &= -\frac{\mu_0}{4\pi} \cdot \bar{\mu}_1 \bar{\mu}_2 \cdot \frac{1}{r^3} (3\cos^2(\theta) - 1) \\ &= -\frac{\mu_0 \gamma_1 \gamma_2 \hbar^2}{4\pi |\mathbf{r}|^3} [3(\mathbf{S}_1 \cdot \mathbf{r})(\mathbf{S}_2 \cdot \mathbf{r}) - \mathbf{S}_1 \cdot \mathbf{S}_2]. \end{aligned} \quad (7.10)$$

where γ_i is the gyromagnetic ratio of the individual particle i , and \mathbf{S}_i represents the spin of particle i .

To simulate this interaction, I construct a 3D model of an FCC crystal lattice, consisting of 200 unit cells in each spatial direction (x, y, z), using the lattice spacing and structure of solid Ne. A single Rb atom is placed at the center, surrounded by additional Rb atoms that are randomly distributed while preserving the host-to-impurity ratio dictated by the optical density (OD). Given that the Zeeman splitting is much larger than the dipolar interaction energy, I treat the spins as fixed dipoles aligned with the applied magnetic field. Figure 7.5,(A) illustrates the central Rb atom embedded within the spin bath in this 3D lattice.

Next, I compute the interaction strength (frequency shift) between the central Rb atom and each surrounding Rb atom, repeating the process 200 times. The resulting average shifts strength between the spin bath and the central Rb atom is presented in the histogram in Figure 7.5 (B). From these calculations, we estimate a spin bath linewidth following a Gaussian profile with a FWHM of 7 MHz, denoted as γ_s , which corresponds to a cooperativity of $C \sim 7$, assuming a best-case coupling of 4 MHz. This should place the system in the strong coupling regime, yet the expected coupling is not achieved. The discrepancy could be due to several factors, including a lower-than-expected atomic density, difficulties in growing a uniformly doped crystal, or a broader-than-expected linewidth, potentially caused by additional impurities in the system, such as molecular clusters.

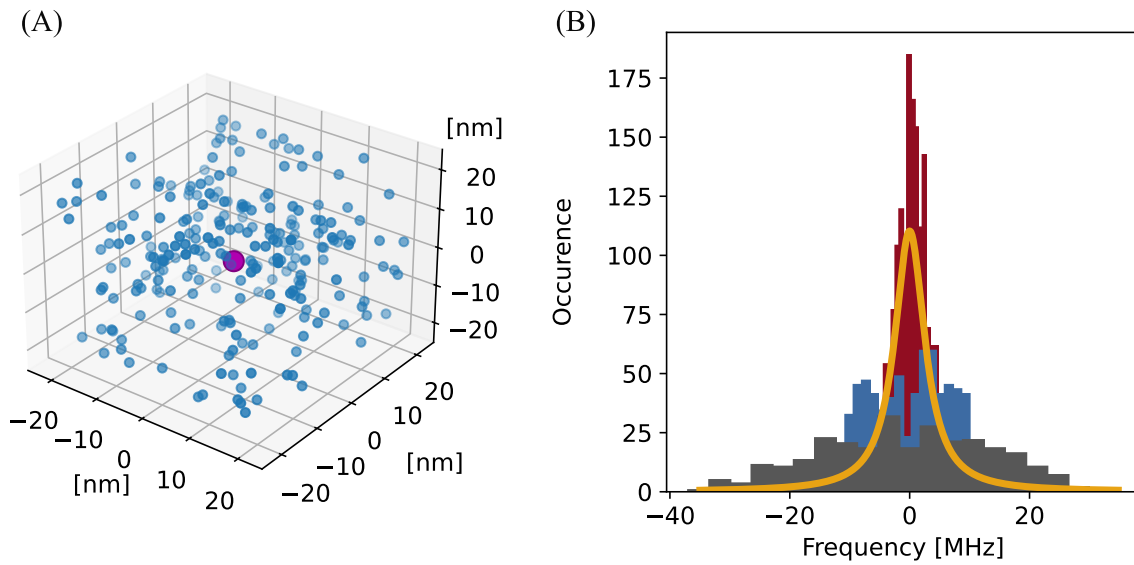


Figure 7.5 (A) Simulation of a centered Rb atom and the surrounding spins used to calculate the dipole-dipole interaction in 3D. Process was performed 200 times. (B) Selected runs (red, blue, and grey bar graphs) to demonstrate the differences between simulation. Occurrence is the number of times spins had a particular coupling. The average fit of the 200 total simulations (gold). The linewidth of ^{85}Rb - ^{85}Rb is 7 MHz from a density $6 \times 10^{17} \text{cm}^{-3}$

7.4.4 Coupling of sodium

In this section, we provide a more detailed analysis than in the Rb case, as we successfully achieved the strong coupling regime with Na. The primary motivation for transitioning to Na-based impurities was twofold: first, Na has fewer hyperfine levels compared to ^{85}Rb , reducing state distribution; second, it has a single stable isotope, effectively increasing the number of "identical" emitters available for coupling.

After growing a Na-doped solid neon crystal, we followed the same microwave measurement procedure outlined in microwave step procedure (5) as for the Rb-doped crystals. The resulting microwave spectrum demonstrates a significant improvement compared to the Rb-based measurements, confirming the advantages of Na for achieving strong coupling. The work below was using the crystal from Figure 6.5.

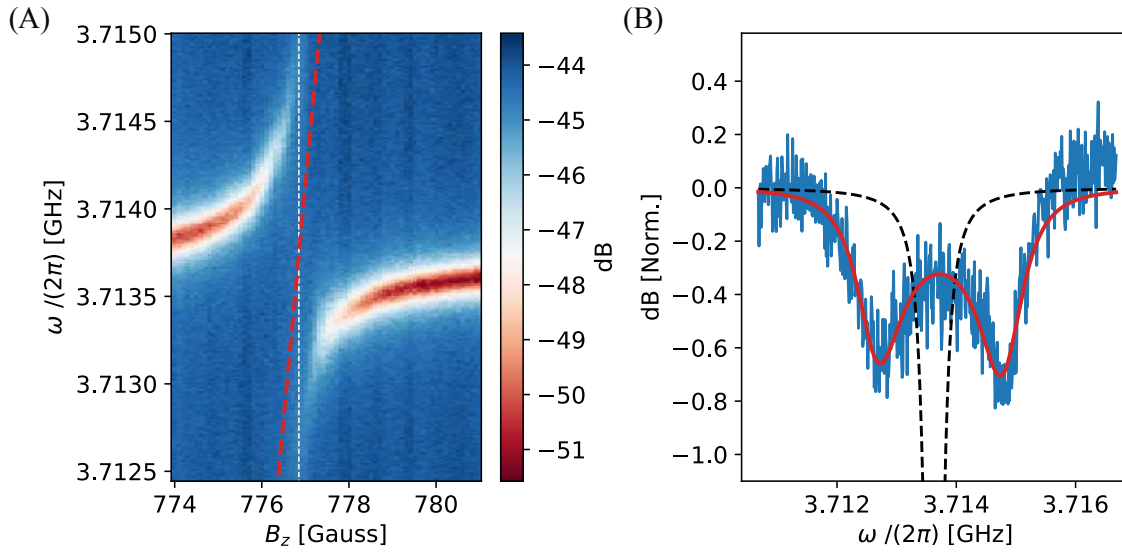


Figure 7.6 (A) Magnetic field sweep of a Na doped Ne crystal. Dashed red line is the atomic transition as it is Zeeman tuned across the resonator. Horizontal dashed white line is when the atom's frequency and cavity's frequency are on resonance. (B) Single trace at the dashed white line. Normalized data (blue) is fitted (red) using equation 5.17. Black dashed line is the transmission of the bare resonator. The collective coupling and atomic linewidth $(g_{\text{eff}}, \gamma) = 2\pi \times (1.15 \text{ MHz}, 0.832 \text{ MHz})$.

Here, we present the first instance of strong coupling between the ensemble and the superconducting resonator. In Figure 7.6 (A), the transmission spectrum clearly shows a more pronounced atom-cavity interaction compared to the Rb-doped crystal, with a distinct splitting between the $|+\rangle$ and $|-\rangle$ states. Figure 7.6 (B) shows a single trace when the atoms and cavity are on resonance. This allows us to quantify the enhanced coupling, g_{eff} , and estimate the ensemble linewidth, γ_s .

Fitting the transmission spectrum to Equation 5.17, we obtain the following parameters: $g_{\text{eff}} = 1.15 \text{ MHz}$, $\gamma_s = 0.832 \text{ MHz}$, at an atomic transition frequency of $\omega_s = 3.7137 \text{ GHz}$. A cooperativity can be estimated to be $C \sim 10$. These values confirm that we are in the strong coupling regime, where $g_{\text{eff}} > \kappa, \gamma$. Additionally, the shift in the free Na atom's expected hyperfine transition is approximately -1.6%.

A quick estimation allows us to compare our optical and microwave spectroscopy. The number of participating spins within the resonator mode can be estimated as

$$N = \sqrt{\rho \cdot V_{\text{mode}} \cdot P_{\text{thermal}} \cdot f}, \quad (7.11)$$

where ρ is the atomic density (in atoms per m^3), V_{mode} is the mode volume of the resonator (in m^3), P_{thermal} represents the fraction of atoms in the hyperfine ground state, and the parameter f accounts for the polarization percentage in the $|F, m_f\rangle = |1, 1\rangle$ state.

By substituting the values $\rho = 3 \times 10^{22} \text{ m}^{-3}$, $V_{\text{mode}} = 700 \times 10^{-6} \times (400 \times 10^{-6} \times 150 \times 10^{-6}) \text{ m}^3$, $P_{\text{thermal}} = 0.98$, and $f = 0.37$ we obtain

$$N = \sqrt{(3 \times 10^{22}) \cdot (700 \times 10^{-6} \times 400 \times 10^{-6} \times 150 \times 10^{-6}) \cdot 0.98 \cdot 0.37},$$

which evaluates to approximately 675,000 spins within the mode volume. Given an average single-spin coupling strength of $g \approx 5 \text{ Hz}$, this corresponds to an expected collective coupling of approximately 3.3 MHz. That is a factor of 3 difference, which may suggest that the OD is off by almost an order of magnitude. It is also possible that the density of the crystal is not uniform, causing an inaccuracy in coupling strength. Furthermore, this estimate assumes an average coupling strength throughout the crystal, which is not strictly the case. Using finite-element simulations in COMSOL, incorporating the spatial variation of the resonator's magnetic field (Figure 5.9 (C)), we obtain a more refined prediction. For an optical density of $\rho = 3 \times 10^{22} \text{ m}^{-3}$, the expected total coupling is approximately 1.7 MHz, which is in good agreement with the measured value of 1.15 MHz.

7.5 Na atomic linewidth

Now that we are able to reach the strong coupling regime, we have a method to directly measure the atomic linewidth, requiring only an additional microwave source. The measurement begins by detuning the spin ensemble magnetically from the cavity resonance ($\Delta \gg \gamma$). It is important to note that even though the atoms are detuned from the cavity, there remains a nonzero interaction between the cavity and the spins, resulting in a small shift in the cavity's frequency. This shift can be calculated using equation 4.40.

With our second microwave source, we can produce a sharp (in frequency space) microwave tone that spectrally pierces the spin ensemble. With sufficient power in the microwave tone, a sub-ensemble of spins will thermalize out of equilibrium, which reduces the total effective coupling, g_{eff} , to the cavity. By sweeping the sharp microwave tone across the entire ensemble, we can measure the shift as a function of frequency,

with the largest shift occurring at the maximum of the spin distribution. This is illustrated in the figure below.

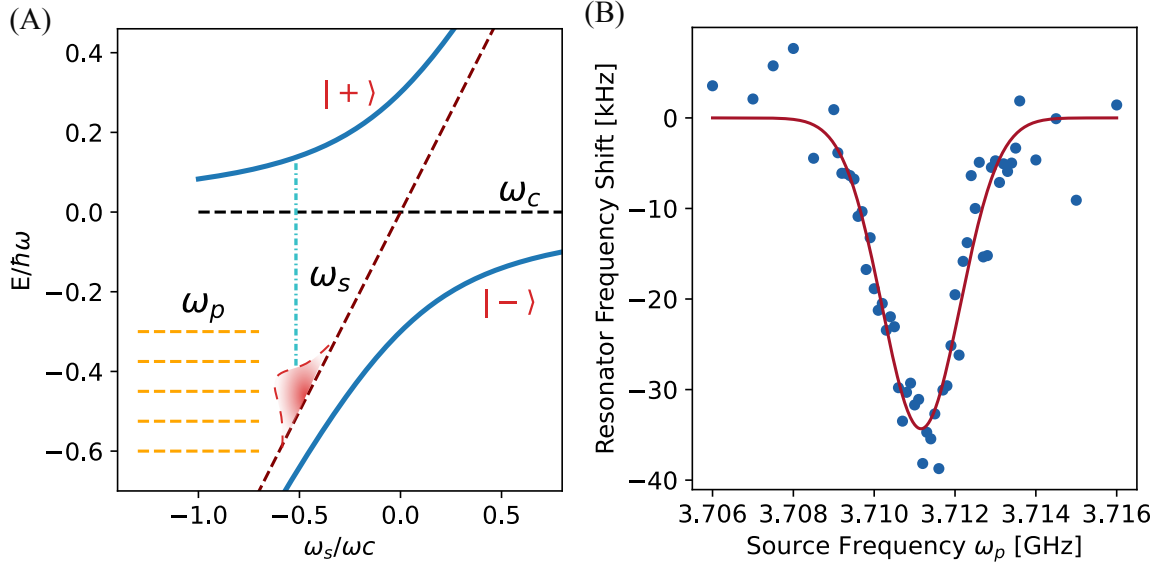


Figure 7.7 (A) Pictorial representation of the spin distribution measurement. The atomic ensemble (shaded red) is pierced with narrow microwave pulses ω_p . As the spins are thermalized, a difference in coupling is measured. (B) Shift in resonator frequency as sharp microwave pulses are applied over the spin ensemble. The atomic linewidth is fitted to a Gaussian and results in a linewidth $\gamma = 0.98$ MHz.

From this data, we fit the ensemble to a Gaussian distribution and obtain an atomic linewidth of 0.98 MHz, the single trace in Figure 7.6 (B).

Similar to the Rb case, we modeled the spin-spin interaction of Na in a Ne crystal. Assuming a density of $\rho = 3 \times 10^{16}$ atoms/cm⁻³, we expect a linewidth, $\gamma_s = 0.2$ MHz. This linewidth is of the same order of magnitude as the measured linewidth. This discrepancy suggests that the dominant source of line broadening is likely due to additional impurities in the crystal or inhomogeneous broadening from the polycrystalline structure.

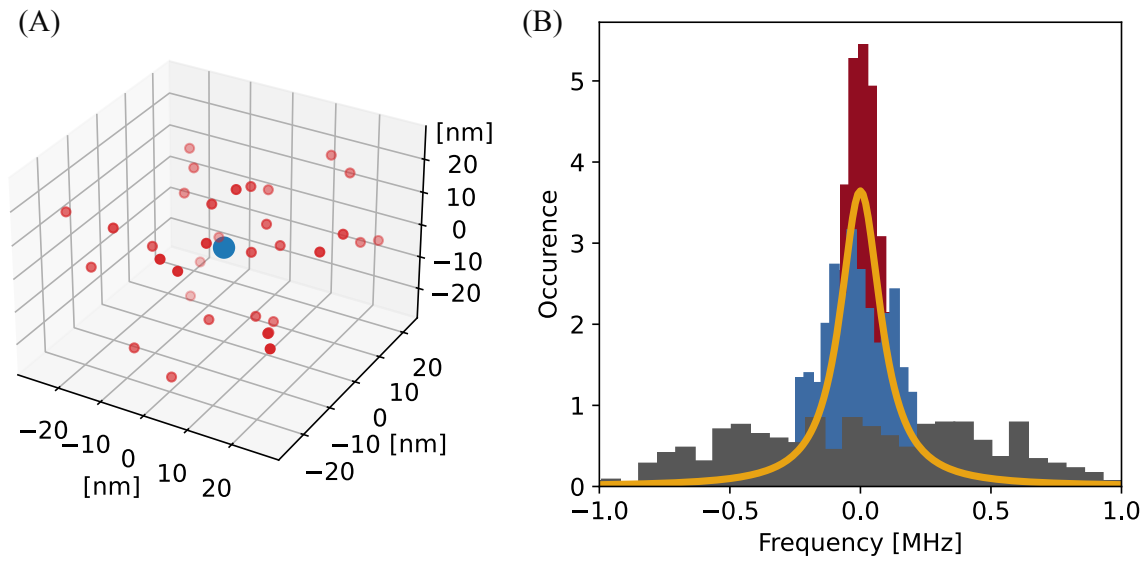


Figure 7.8 (A) Simulation of a centered Na atom and the surrounding spins used to calculate the dipole-dipole interaction in 3D. The process was performed 200 times. (B) Selected runs (red, blue, and grey bar graphs) show the differences between individual simulations. Occurrence is the number of times spins had a particular coupling. The average of the 200 total simulations is shown in gold. The linewidth of ^{23}Na - ^{23}Na is 0.2 MHz with a density $\rho = 3 \times 10^{16}$ atoms/cm $^{-3}$.

Dipole-dipole interactions between Na atoms are not the only source of line broadening. As noted in Table 2.1, natural neon contains 0.2% of the non-zero spin isotope, ^{21}Ne . To assess the contribution of additional broadening caused by nuclear spin interactions, we ran a similar simulation to the Rb and Na dipole calculations. We found that even with the higher percentage of ^{21}Ne , the additional broadening would be only 4 kHz, which is relatively small. This is simulated in Figure 7.9.

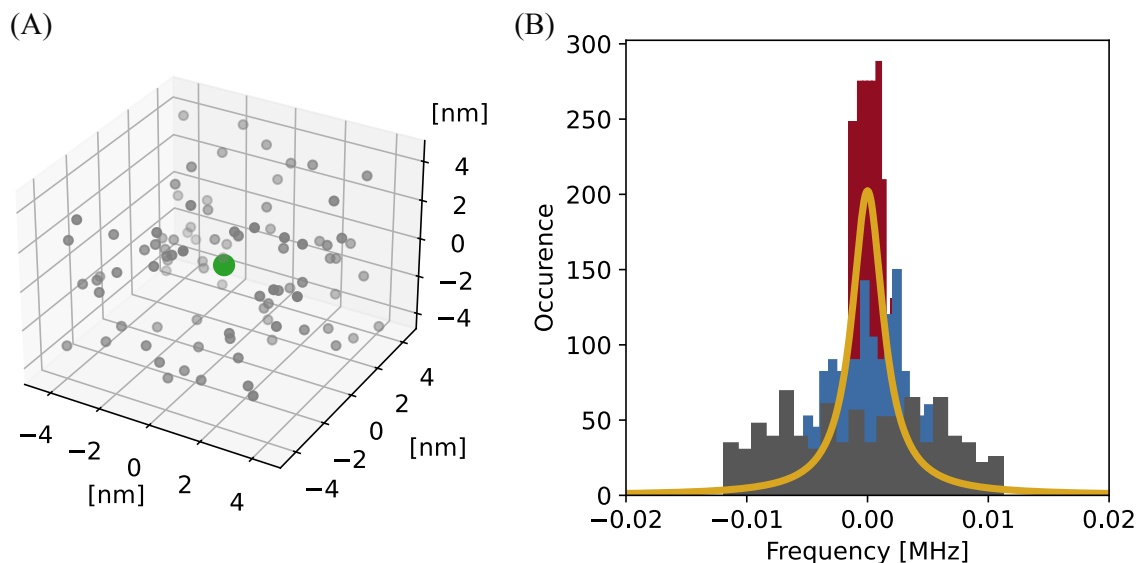


Figure 7.9 (A) Simulation of a centered Na atom and the surrounding nuclear spins used to calculate the dipole-dipole interaction in 3D. Process was performed 200 times. (B) Selected runs (red, blue, and grey bar graphs) to demonstrate the differences between each simulation. Occurrence is the number of times spins had a particular coupling. The average fit of the 200 total simulations (gold). The linewidth of ^{23}Na - ^{21}Ne is 4 kHz with a density $\rho = 5.7 \times 10^{18} \text{ atoms/cm}^{-3}$ or $\sim 0.02\%$ of the total neon.

7.6 Longitudinal and spin relaxation

In quantum mechanics and in particular magnetic resonance, the relaxation times T_1 and T_2 are fundamental parameters that describe the dynamics of spin ensembles, which offer us insights into their interactions with the surrounding environment [82, 83]. These time constants are essential for applications such as quantum computing and magnetic resonance imaging (MRI). The T_1 time, or spin-lattice relaxation time, characterizes the exponential recovery of the system's longitudinal magnetization toward its thermal equilibrium value along the external magnetic field. This process involves energy exchange between the spins and their environment, making T_1 highly sensitive to local conditions, i.e. between the cryogenic crystals and the spins.

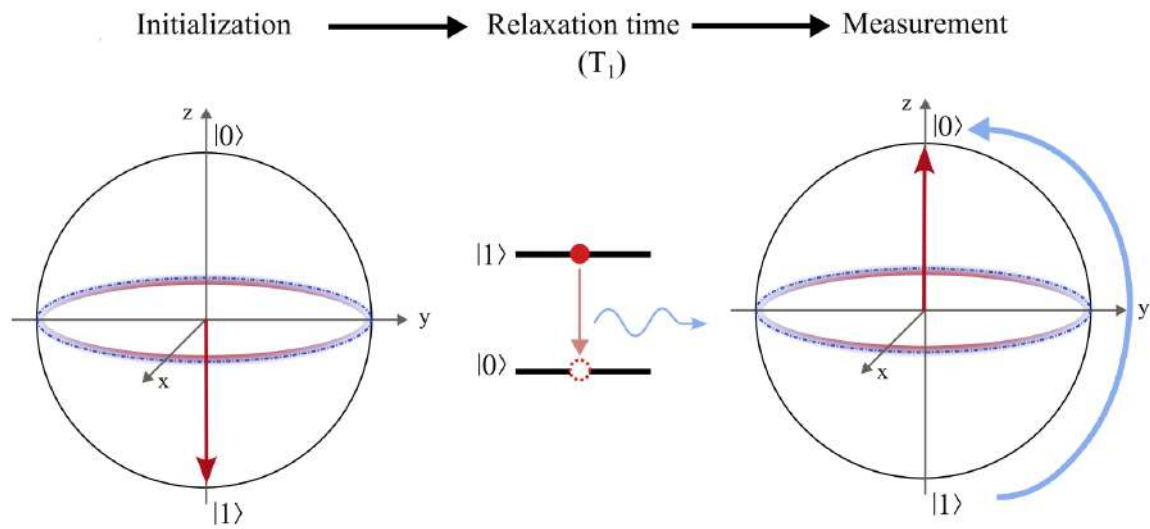


Figure 7.10 Pictorial representation of a Bloch sphere prepared in the $|1\rangle$ state, which after some time decays to the $|0\rangle$ state. The time in which it decays is known as the T_1 time. The $|1\rangle$ state represents the excited, or out-of-equilibrium state, in our system, which relaxes to the ground state $|0\rangle$ over time.

In contrast, the T_2 time, or spin-spin relaxation time, characterizes the decay of the off-diagonal elements of the density matrix, such as $|0\rangle\langle 1|$ and $|1\rangle\langle 0|$, which correspond to quantum coherence. Unlike T_1 , T_2 arises from interactions such as dipole-dipole coupling or magnetic field gradients and does not involve energy dissipation.

Accurate measurements of both T_1 and T_2 are crucial for characterizing spin systems and optimizing their performance in various technologies, and in particular, our hybrid quantum system. Common methods include the inversion recovery technique for T_1 , where a sequence of inversion pulses and variable delay times tracks the recovery of M_z . For T_2 , spin echo (Hahn echo) [84] and CPMG sequences [85, 86] are widely used, as they counteract inhomogeneous broadening effects to isolate the intrinsic dephasing rates. Understanding these relaxation times forms the foundation for advancing spin-based technologies and achieving precise control over quantum systems. Here, we will describe our methods of measuring both T_1 and T_2 .

Spin-lattice relaxation

To determine the T_1 relaxation time of our spin ensemble, we first prepare the spins in a 50/50 mixture between the upper and lower hyperfine levels and then cool them

down, inducing a population polarization. The T_1 time corresponds to the duration required for the spins to thermalize to the ground state.

As the spins relax, the effective coupling strength g_{eff} increases, causing a shift in the cavity frequency. By tracking this frequency shift over time, we extract the T_1 . Importantly, we measure with the atomic ensemble detuned from the resonator's frequency due to the enhanced Purcell effect which increases the spontaneous decay rate of spins to the cavity which can be calculated using the following equation

$$\Gamma_P = \kappa \frac{g^2}{\kappa^2/4 + \delta^2} \quad (7.12)$$

where $\delta = \omega_c - \omega_{\text{eg}}$ is the spin-cavity detuning, and κ is the decay rate of the cavity (~ 200 kHz in our system). A more in-depth understanding of this technique can be found in References [87–89].

We begin our measurement by reducing the temperature and bleaching the spins to ensure strong coupling to the resonator. Immediately afterwards, we detune our spins from the cavity, approximately 10 G below, or roughly 10 times the atomic linewidth from the cavity. The difference in frequency, δ , between the spins and the resonator results in a suppression of the Purcell enhanced spontaneous decay rate by approximately 3000. Then we begin warming the temperature of the ADR to 500 mK, which results in a thermal mixture with approximately 55% of the spins in the ground state, and 45% in the excited. We wait 30 min, and then we begin ramping the spin ensemble down to the base temperature of the ADR at a rate of 0.100 mK/min. Once the spins are cold, we begin taking frequency traces of the cavity with the VNA and measure the shift in the center frequency of the cavity. As the spins cool, the shift of the cavity will increase, as seen in Figure 7.11. Note that the 5 minutes it takes to cool the spins are not recorded.

In the dispersive regime, the expected total frequency shift can be approximated to be calculated by

$$E_{\text{disp}}/\hbar \approx \left(\omega_c \pm \frac{g^2}{\Delta} \right). \quad (7.13)$$

With a $\Delta = 28$ MHz, $g = g_{\text{eff}} = 1.1$ MHz, a shift of approximately 43 kHz from the bare cavity is expected. In Figure 7.11 we measure the time it takes the entire spin ensemble to relax to be 10 minutes. This is fitted with a stretched exponential of the form

$$\Delta f = e^{\left(\frac{t}{T_1} \right)^\beta}. \quad (7.14)$$

Where Δf is the total shift in the cavity's frequency, t is the time beginning from the cool down, T_1 is the longitudinal relaxation time, and β is a dimensionless factor which accounts for some of the different T_1 times the spin ensemble has [90]. The spins closest to the boundaries, i.e. the superconductor and the surface of the crystal, can decay at a rate different from that of the spins in the bulk. The surface can have radicals, spare electrons, or other impurities which can open an avenue for spins to diffuse. The stretched exponential resulted with a fitted β of 0.51, which seems to be close to the expected 0.5 fitted β of other spin ensembles [90]. We have a fitted total frequency shift of 60 kHz, which is close to the expected 43 kHz. Fitting the curve to a single exponential ($\beta = 1$) results in T_1 of approximately 20 min.

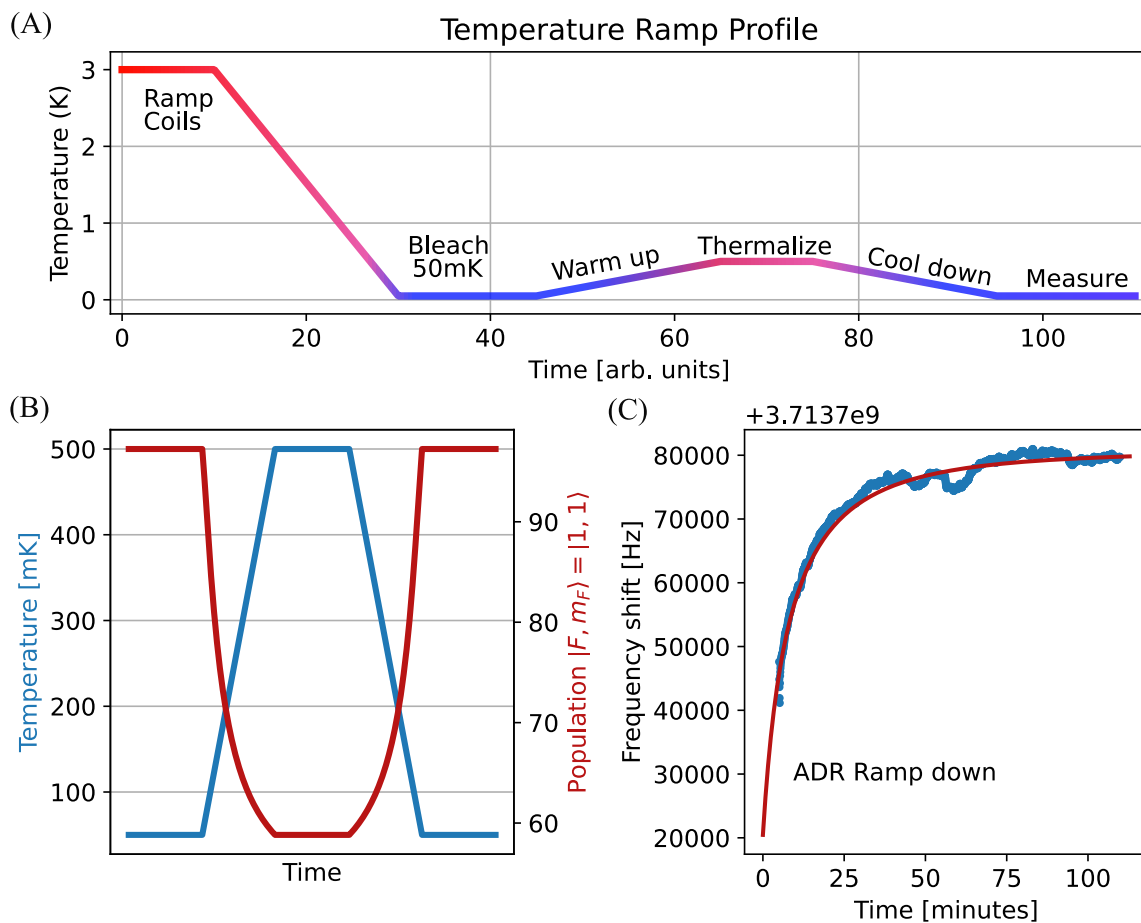


Figure 7.11 (A) Diagram of the crystal temperature as a function of time and the associated actions. (B) (LHS) Temperature of the crystal after bleaching which is then thermalized to 500 mK, and then dropped back to 55 mK. (RHS) Population of the $|1, 1\rangle$ state as a function of temperature. At low temperatures the population is high, and vice versa. (C) Shift in resonator frequency as the ensemble thermalizes from 500 mK to 55 mK. The shift in frequency is fitted to a stretched exponential with a $T_1 = 10$ minutes and a $\beta = 0.51$.

Spin-decoherence

With the measurement of T_1 complete, we shift our attention to T_2 , the spin-spin relaxation time, which provides complementary insights into the dynamics of a spin system. While T_1 reflects the recovery of longitudinal magnetization through energy exchange with the environment, T_2 describes the decay of transverse magnetization caused by dephasing of individual spins in the ensemble. This dephasing is influenced by both intrinsic interactions, such as spin-spin coupling, and extrinsic factors, including

inhomogeneities in the local magnetic field. To accurately measure T_2 and distinguish intrinsic spin-spin relaxation from extrinsic dephasing effects, we rely on specialized pulse sequences designed to refocus dephased spins and isolate the true coherence decay.

The Hahn echo sequence is a foundational pulse sequence used to measure spin-spin relaxation (T_2) and to mitigate the effects of inhomogeneous broadening in magnetic fields. It begins with a 90° pulse that tips the spins into the transverse plane, followed by a delay period during which the spins dephase due to local field inhomogeneities. A subsequent 180° pulse flips the spins, causing them to rephase, or "echo," at a time equal to twice the delay. The intensity of this echo reveals the effects of intrinsic dephasing processes while canceling out static field inhomogeneities. Originally conceived by Erwin Hahn in the 1950's as a method to describe ensemble of spins in a solid, it has since found its way into the fields of biology, medicine, material science, quantum physics, and many others. Interestingly, the Nobel committee did not deem his discovery worth of a Nobel prize. The beauty of the Hahn echo is that it is simple and effective for isolating intrinsic relaxation effects in systems with minimal time-dependent field fluctuations. With respects to our system, a Hahn echo would be able to echo out the static inhomogeneous broadening caused by the clusters and dipole-dipole interactions between identical species.

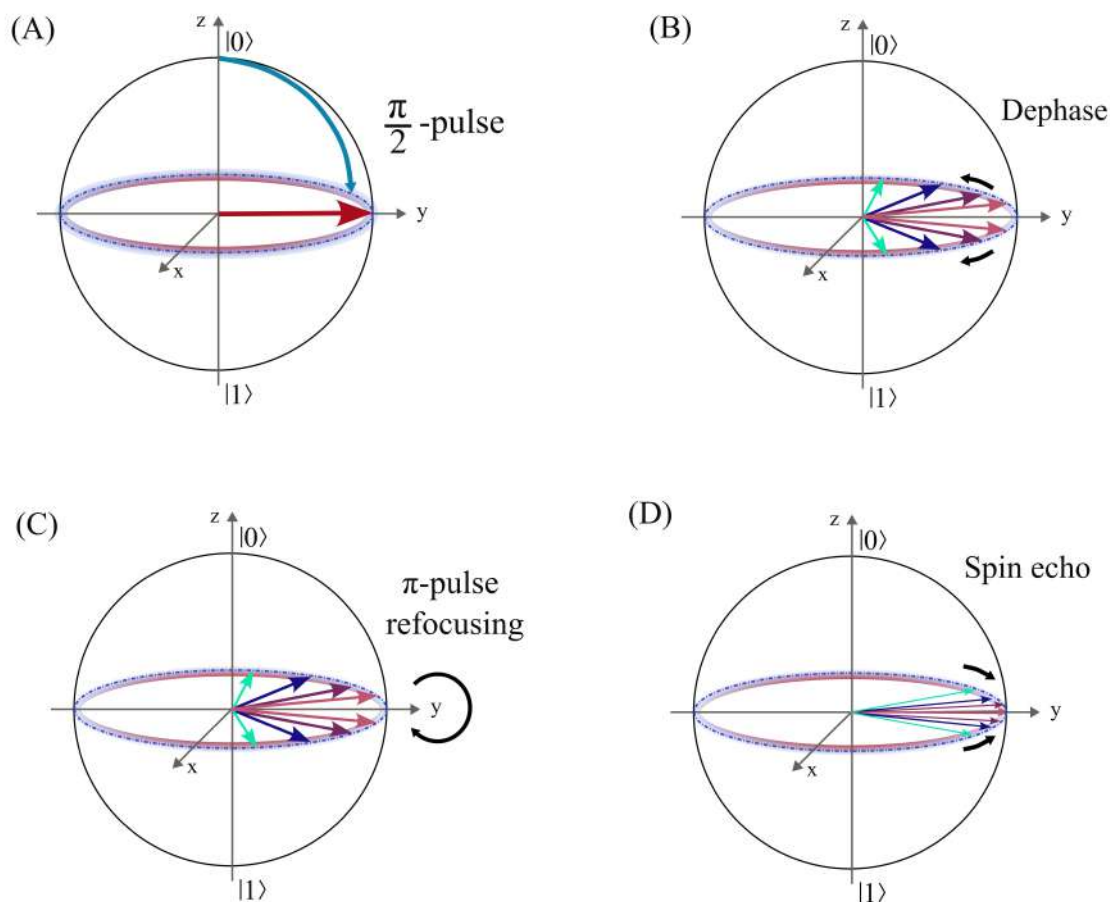


Figure 7.12 Visualization of a Hahn echo. (A) the prepared state is displaced to the equator with a $\frac{\pi}{2}$ -pulse. The large red vector represents many spins. (B) As each spin Larmor processes at slightly different frequencies, they begin to spread over the equator. (C) A π rotation on the y axis is applied to the spins, causing the spins which initially dephases at some rate ($-\omega't$) to rephase in the opposite direction ($\omega't$). (D) The spins now refocus and produce an echo, which we see as a burst of light from our resonator.

Building on the Hahn echo, the Carr-Purcell-Meiboom-Gill (CPMG) sequence extends its capabilities by introducing a train of evenly spaced 180° pulses after the initial 90° pulse. This series of refocusing pulses maintains spin coherence over longer periods, allowing the measurement of T_2 even in systems with more significant time-dependent field variations. The key difference lies in the repetitive nature of the 180° pulses in CPMG, which provides superior resilience to noise and dynamic dephasing effects compared to the single refocusing pulse in Hahn echo. This can be understood as repeating the refocusing pulse in Figure 7.12 (C). Additionally, the CPMG sequence

can enhance signal-to-noise ratios by summing multiple echoes, making it especially advantageous in noisy environments or systems with low spin concentrations.

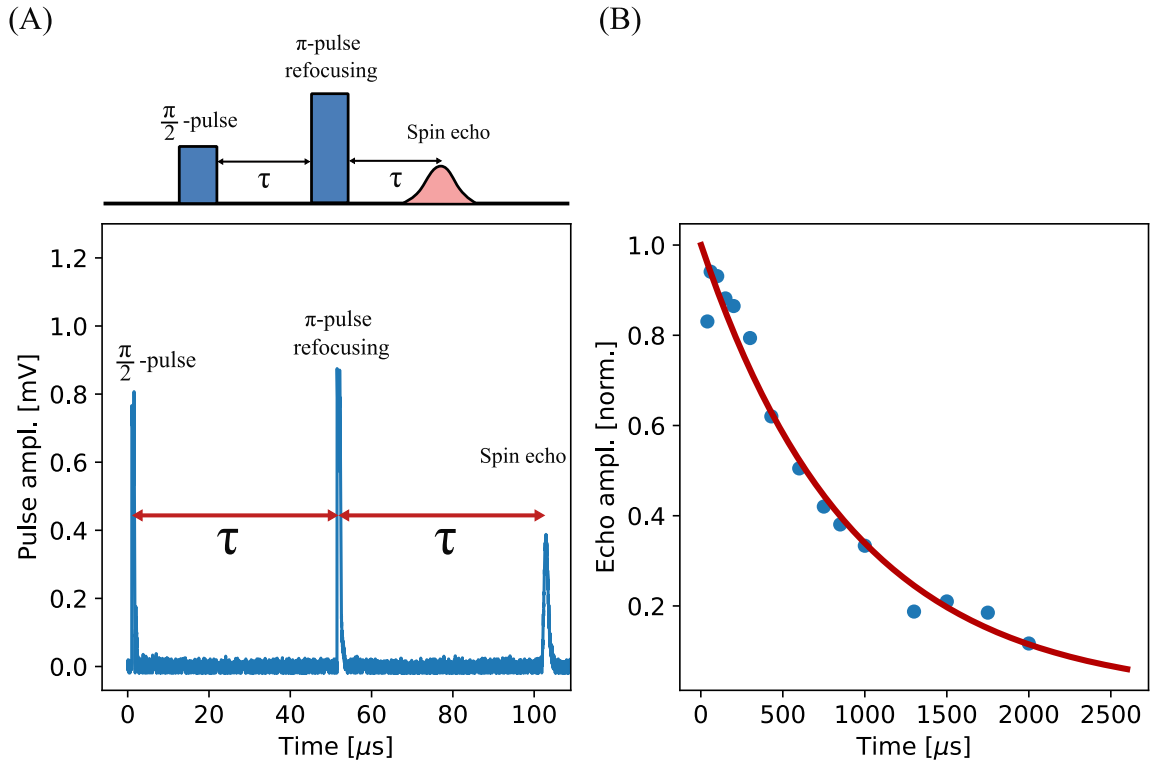


Figure 7.13 (A) (Top) representation of a Hahn echo. (Bottom) Single Hahn echo experiment with a τ of $50 \mu\text{s}$. After applying a π pulse, we see a clear echo $50 \mu\text{s}$ afterwards. The amplitude of the $\pi/2$ and π pulse are 0.5-1 respectively and a pulse width of $1 \mu\text{s}$. Our amplifier saturated at a voltage of 0.86 mV which is why they have similar heights. (B) Plotted amplitude vs time of the spin echo. Fitted to a single exponential, we obtain a $T_{2,\text{Hahn}} = 0.93 \text{ ms}$.

For our Hahn echo measurements, we construct a rectangular pulse with a pulse amplitude ratio of 0.5 for the $\pi/2/\pi$ sequence (our amplifier was saturated causing our readout to have similar heights as seen in Figure 7.13). Both the $\pi/2$ and π pulses have a duration of $1 \mu\text{s}$. A single echo measurement is shown in Figure 7.13 (A).

The peak amplitudes of the spin echoes are normalized and plotted as a function of time (2τ) and fitted to a single exponential decay in Figure 7.13 (B) with the form,

$$A = A_0 e^{-t/T_2} \quad (7.15)$$

where A_0 is the max amplitude of a short echo, and T_2 is the coherence time. From this fit, we determine a Hahn echo coherence time of $T_{2,\text{Hahn}} = 0.93 \text{ ms}$, which represents a significant improvement over the expected coherence time estimated from the atomic linewidth of $T_{2,\gamma} \approx \frac{1}{0.9 \text{ MHz}} \approx 1.1 \mu\text{s}$.

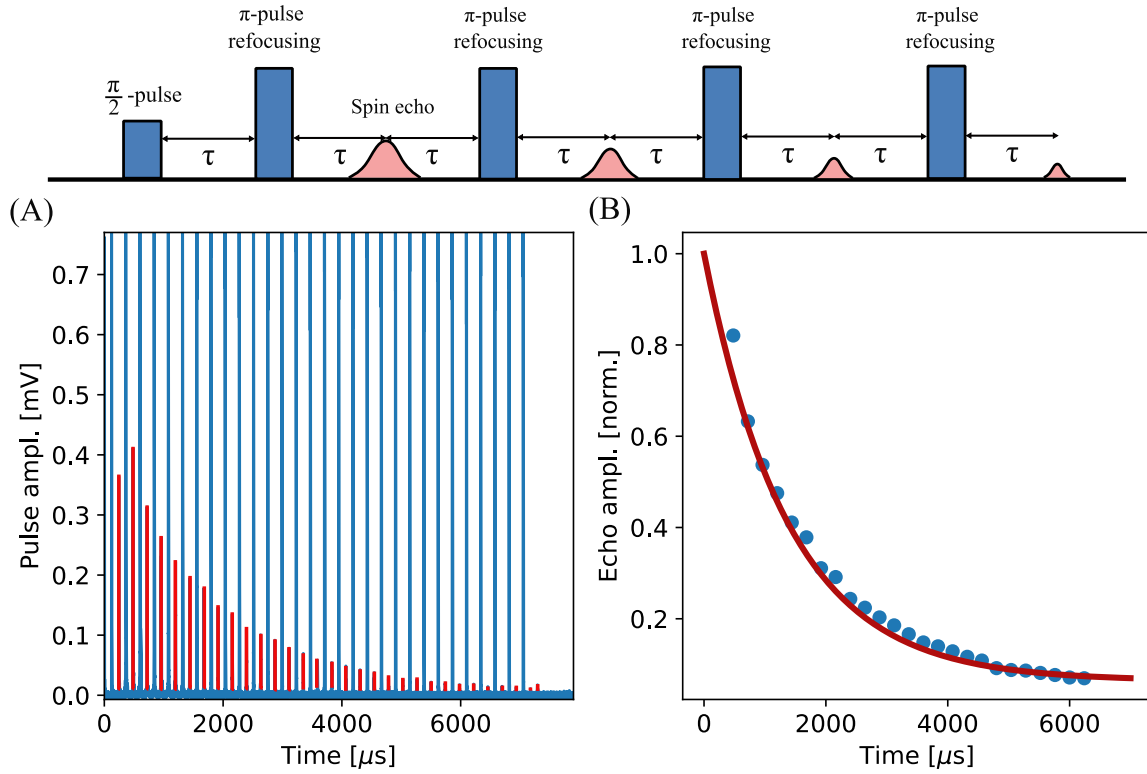


Figure 7.14 (Top) Pictorial representation of a CPMG sequence. (A) Blue lines are a single $\frac{\pi}{2}$ pulse and 30- π pulses ($\tau = 120 \mu\text{s}$). Between the π pulses are the spin echoes (red). Plot is of 20 averaged scans. (B) Fitted to a single exponential, the echo amplitude as a function of time results in a $T_{2,\text{CPMG}} = 1383.8 \mu\text{s}$.

Our CPMG sequence utilized a pulse amplitude ratio, shape, and duration similar to that of the Hahn echo, with a repeated τ of $120 \mu\text{s}$. The echo peaks are plotted as a function of time and fitted to Equation 7.15 (as shown in Figure 7.14 (B)). From this fit, similar to the Hahn echo, we extract a coherence time of $T_{2,\text{CPMG}} = 1.383 \text{ ms}$. This represents only a slight improvement over $T_{2,\text{Hahn}}$, suggesting that our system may be limited by low-frequency noise that cannot be refocused by the pulse sequence, or more likely, by pulse imperfections.

Chapter 8

Cryocrystals and the superconducting interface

In science, unexpected results often lead to new insights. This was the case in my work. When designing the experiment, I was unsure whether the cryogenic crystal would properly adhere to the superconductor or potentially have a detrimental effect on the system. However, it turns out that not only does the cryogenic crystal stick to the resonator, but it can also enhance the internal quality factor, Q_{int} [91]. This study was conducted in collaboration with Professor Ioan Pop's group at the Karlsruhe Institute of Technology (KIT), particularly with, now doctor, Francesco Valenti, during the COVID-19 lockdown.

My initial measurements of p-H₂ crystals deposited on a niobium strip-line resonator indicated that the total quality factor, Q_{tot} , increased after the crystal was on top. The total quality factor, Q_{tot} , is given by extending Equation 5.16 as

$$Q_{\text{tot}} = \frac{\omega}{\kappa_{\text{tot}}} \quad (8.1)$$

An increase in Q_{tot} upon adding a dielectric material is unusual, as such materials typically increase photon scattering, thereby reducing Q_{tot} . This is because Q_{tot} is related to both the internal quality factor Q_{int} , which accounts for energy losses within the resonator, and the external quality factor Q_{ext} , which is linked to energy losses through the coupling to the external environment. Specifically, the total quality factor Q_{tot} is given by the following relationship between the internal and external quality factors:

$$\frac{1}{Q_{\text{tot}}} = \frac{1}{Q_{\text{int}}} + \frac{1}{Q_{\text{ext}}} \quad (8.2)$$

Typically, adding a dielectric material increases κ_{tot} , which leads to an overall reduction in Q_{tot} . However, it is unclear whether the loss is due to an increase in κ_{int} or κ_{ext} , or alternatively, a decrease in Q_{int} or Q_{ext} . Our goal was to determine whether one or both of these factors were contributing to the observed increase in Q_{tot} .

In this section, I will discuss the interaction between the host matrix, specifically p-H₂, and the superconducting resonator made of granular aluminum (grAl). Our hypothesis is that the cryogenic crystal interacts with the superconducting surface in a way that reduces dissipation, likely stemming from an increase in Q_{int} , which in turn lowers κ_{tot} and increases Q_{tot} .

One of the main sources of dissipation in superconducting circuits is the presence of broken Cooper pairs, or quasiparticles (QPs). While operating superconducting circuits at millikelvin temperatures ensures the absence of thermal QPs, athermal QPs—stemming from high-energy particles and stray terahertz radiation (or BBR)—can still contribute to energy losses. We expect that while the cryogenic crystal may introduce some additional loss, the overall effect is an increase in Q_{int} , as the reduction in dissipation from the cryocrystal outweighs any losses it might introduce.

To test our hypothesis, we measured the resonators' response to the cryogenic crystal and observed a significant decrease in quasiparticle losses when the crystal was exposed to pair-breaking terahertz radiation. These results suggest that the cryocrystal contributes to reducing dissipation, likely through a combination of shielding from terahertz radiation and mitigation of other loss mechanisms. Our measurements indicate that the crystal does not significantly increase dielectric loss in the resonators, and we provide a model to explain the observed reduction in quasiparticle losses, highlighting a nontrivial surface effect.

8.0.1 Experimental modifications

To begin, there were slight modifications to our experimental setup inside the cryostat. Specifically, we added a circulator to the microwave up line, applied aluminum tape to shield the resonators from THz radiation while selectively introducing holes to control THz exposure, and changed the resonators. These changes in the experimental setup can be seen in Figure 8.1 (A-E).

A microwave circulator is a device that directs microwave signals in one direction, ensuring that signals move from one port to the next without returning to the source. This prevents noise from the up-line from entering the superconducting device. The change of superconducting resonators, provided by the KIT group, enabled the measurement of both Q_{int} and Q_{ext} , which can be done by a dip resonator. At the time

of these measurements, we did not have the niobium chip resonators described above. Furthermore, working with grAl resonators offers the unique advantage of investigating the interactions of quasiparticles (QPs), given their distinct material properties.

A composite material consisting of aluminum nanocrystals embedded in an amorphous aluminum oxide matrix is commonly referred to as granular aluminum, or grAl for short. This material is of particular interest in the fabrication of superconducting resonators due to its tunable properties, including resistivity and kinetic inductance. By adjusting the oxygen flow during the deposition process, the resistivity and kinetic inductance of grAl can be tuned from aluminum-like values to up to three orders of magnitude larger.

Kinetic inductance arises from the motion of Cooper pairs (the paired electrons responsible for superconductivity) rather than the movement of charge carriers, as is the case in standard inductance. In conventional inductance, current flow generates a magnetic field that opposes changes in current. In contrast, kinetic inductance involves the inertia of Cooper pairs, which results in an effective inductance that is sensitive to the supercurrent flow in the material. This makes the inductance in grAl larger than that of conventional superconductors. By controlling the oxygen content during deposition, the kinetic inductance fraction can approach unity, thereby maximizing the participation ratio of quasiparticle losses while maintaining high Q factors in resonators—on the order of 10^5 in the single-photon regime and exceeding 10^6 when strongly driven. These properties make grAl an ideal material to explore the interaction between the cryocrystal and the loss mechanisms in superconducting circuits

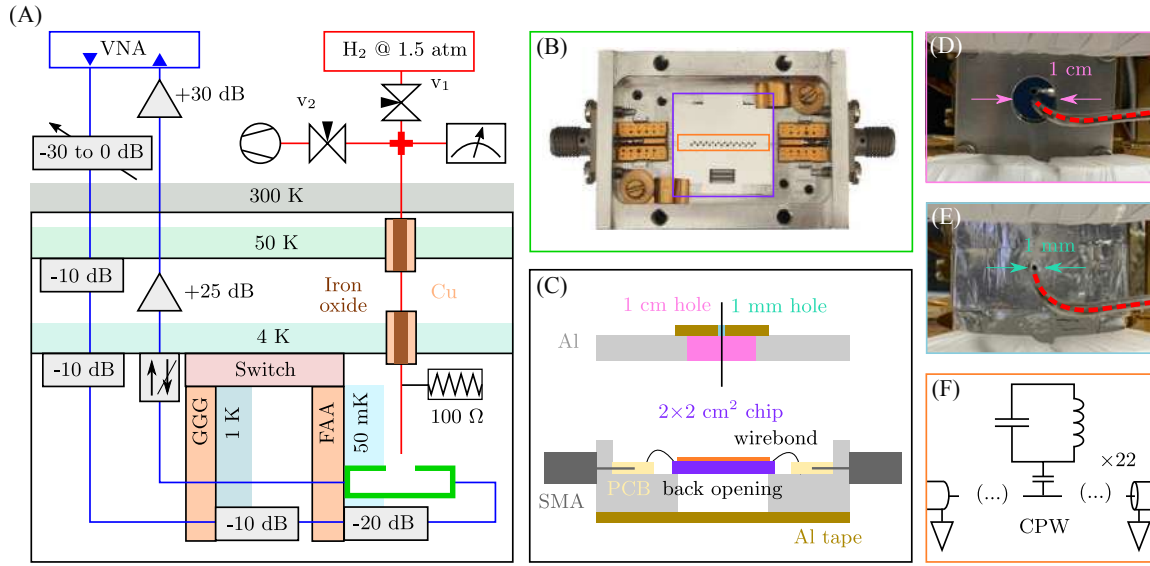


Figure 8.1 (A) Experimental setup: similar to 5.1, however a microwave circulator (up/down arrow block) is added to the upline and a different resonator is added. Fiber optics, ovens, shutter, and superconducting coils are not present. (B) Photograph of the solid aluminum transmission sample holder showing the two SMA ports and printed circuit boards. (C) schematic half-section of the sample holder and its lid. Note the $1.5 \times 1.5 \text{ cm}^2$ opening on the backside of the sapphire chip (sealed with aluminum tape) and the circular hole in the lid, 1 cm in diameter. (D) Photograph of the 1 cm hole setup. (E) Photograph of the 1 mm hole setup. (F) Schematics of the circuits used.

In order to compare the participation, we use two $2 \times 2 \text{ cm}$ sapphire chips, each hosting 22 grAl resonators as seen in Figure 8.1 (B,F). The two different films on the chips are referred to as samples S and L (see Figure 8.2 (A)), exhibit normal-state sheet resistances of $R_{\square} = 800 \, \Omega$ and $20 \, \Omega$, respectively. Sheet resistance, R_{\square} , is a measure of resistivity for thin films of material, expressed in ohms per square (Ω/\square). It quantifies how resistive a film is to electric current flow, independent of its physical dimensions, making it particularly useful for characterizing conductive coatings, superconducting films, and semiconductor layers.

The resonators are designed as lumped-element circuits, featuring a four-finger interdigitated capacitor and an inductive meander in the form of a Hilbert curve [92] as seen in Figure 8.2 (A). The capacitance is adjusted by varying the finger length between 40 and 60 fF. The Hilbert fractal design is chosen for its space-filling properties and its balanced distribution of vertical and horizontal segments, allowing the device to respond to two orthogonal light polarizations simultaneously [93]. The grAl layer, 20 nm thick, is patterned onto a $330 \, \mu\text{m}$ thick *c*-plane sapphire substrate using electron-beam

lithography and lift-off techniques. Subsequently, a 50 nm thick aluminum feedline and ground plane are deposited via optical lithography and lift-off. The structures are wirebonded with aluminum threads to the sample holder PCBs (see Fig. 8.1B and C).

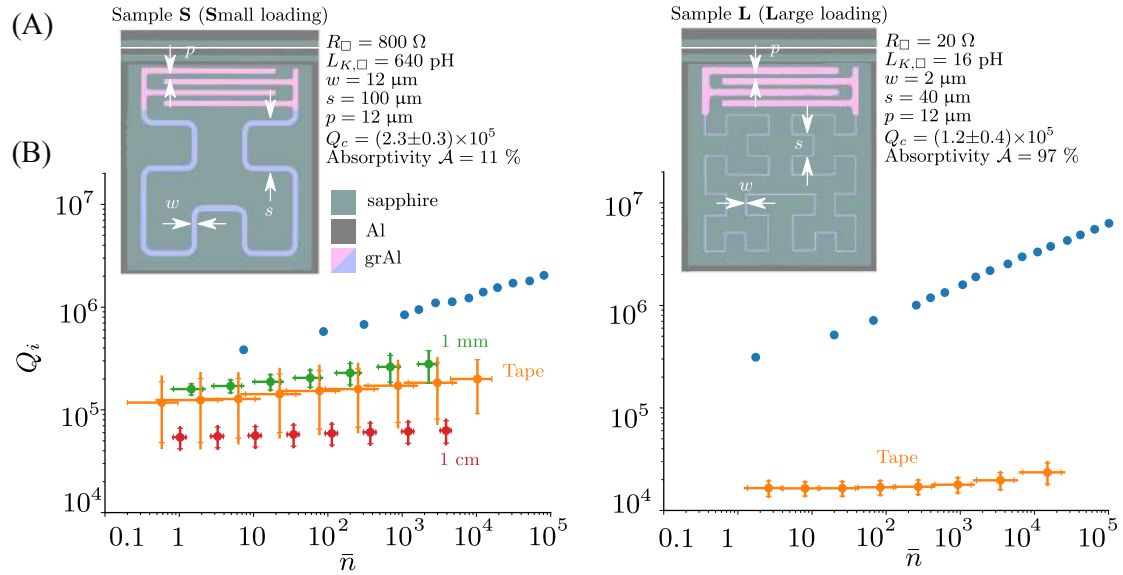


Figure 8.2 (A) False-colored micrographs of the two types of granular aluminum (grAl) resonators used in the measured samples, labeled “S” and “L” for Small and Large coupling to the vacuum impedance, respectively. The grAl resonators (pink/violet), patterned on sapphire (sage), are coupled to a CPW feedline with an aluminum pin and ground plane (gray). Both resonators share an interdigitated capacitor design (pink) with variable finger lengths, covering a capacitance range of 40–60 fF. The grAl inductors (violet) are Hilbert curves of degree 2 and 3, with different widths to ensure a comparable total inductance despite the 40-fold difference in resistivity. (B) Internal quality factor, Q_i , as a function of the average number of drive photons in the resonator. The traces are averaged over all visible resonators, with error bars representing one standard deviation along both axes. As the optical loading on the sample is progressively increased—by enlarging the aperture and enhancing coupling to the vacuum—the internal quality factor decreases due to terahertz radiation inducing Cooper pair breaking.

To systematically investigate the impact of terahertz (THz) radiation on the resonators, we implemented a controlled variation of blackbody radiation (BBR) using aluminum tape shielding. A pictorial representation is seen in Figure 8.1 (C). The THz radiation in our setup originates from a combination of the second-stage copper plate and the BBR emitted by the second-stage radiation shield. We performed four distinct measurements to assess the effect of shielding: (1) a fully sealed configuration (screwed

down aluminum sheet metal), referred to as the "dark measurement", conducted at KIT in a dilution refrigerator; (2) a measurement with the resonators completely covered in aluminum tape, minimizing exposure to external radiation; (3) a configuration with a 1 mm hole in the tape, allowing a small, controlled amount of THz radiation to reach the resonators; and (4) a measurement with a 1 cm hole, significantly increasing the exposure. By incrementally varying the THz load, we were able to probe the sensitivity of the system to radiation-induced dissipation and evaluate the role of the cryogenic crystal in mitigating these losses.

We aim to assess how much blackbody radiation from the gas tube is absorbed by the resonator. Following Ref. [94], the absorptivity is determined by the impedance matching between the device and vacuum, with an optimal sheet resistance per square given by

$$R_{\square, \text{match}} \approx \frac{w}{s} Z_0, \quad (8.3)$$

where w is the meander width, s is the zeroth-order fractal size, and $Z_0 \approx 377 \Omega$ is the vacuum impedance. The absorptivity for a given sheet resistance R_{\square} is

$$\mathcal{A} = 1 - \frac{|R_{\square, \text{match}} - R_{\square}|}{R_{\square, \text{match}} + R_{\square}}. \quad (8.4)$$

This gives us two independent tuning parameters for coupling superconducting films to stray pair-breaking radiation: the absorptivity \mathcal{A} , which depends on film resistivity and resonator geometry, and the lid aperture (1 cm or 1 mm). We designate the two fabricated samples as "S" ($\mathcal{A} = 11\%$) and "L" ($\mathcal{A} = 97\%$), corresponding to small and large absorptivity, respectively.

8.0.2 Experimental results

To characterize the samples, we conduct transmission microwave spectroscopy, similar to the techniques used in Chapter 5. The scattering parameters are analyzed using the Qkit [95] circle fitting routine, based on the method described in Ref. [96]. This approach allows us to extract the internal and coupling quality factors of the resonators, as well as estimate the average number of circulating photons at resonance for a given drive power (\bar{n}). The internal quality factor, Q_i , is plotted as a function of the average photon number, \bar{n} , in Figure 8.2 (B). We observe that Q_i increases with increasing resonator drive for all shieldings, which can be attributed to either the saturation of dielectric loss [97, 98] or the activation of quasiparticle diffusion [99].

By increasing the terahertz load—either by enhancing the absorptivity (from sample S to sample L) or by enlarging the aperture size (colored markers)—we observe two key effects. First, the average Q_i decreases, indicating a higher quasiparticle background. This is to be expected as the aluminum tape has a small possibility to leak light. Second, the dependence of Q_i on drive power diminishes, as evidenced by a reduction in the positive slope of Q_i versus \bar{n} . This suggests that a constant background of quasiparticles becomes the dominant loss mechanism under increased terahertz exposure.

Furthermore, we observe a significant decrease in Q_i between samples S and L even when only the aluminum tape was used for shielding. This reduction can be attributed to the higher absorptivity of sample L. Unfortunately, when additional terahertz radiation was introduced by creating an aperture, the Q_i of sample L deteriorated even further, making the fitting process increasingly challenging. In contrast, sample S maintained relatively high Q_i values with both the 1 cm and 1 mm apertures.

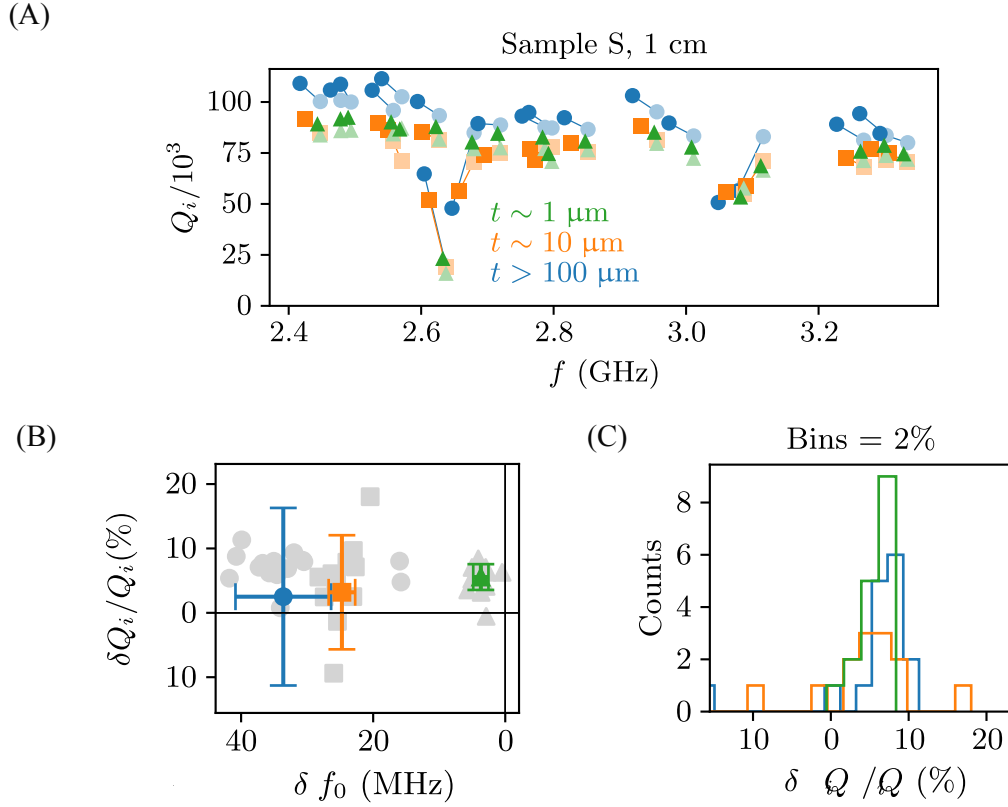


Figure 8.3 (A) Internal quality factors, Q_i , for all visible resonances in the sample for various crystal thicknesses. Shaded and solid colors represent measurements taken before and after crystal deposition, respectively. (B) Relative Q_i variation as a function of the frequency shift induced by the dielectric change. To enhance clarity, the value (colored markers) is averaged over all values (solid gray markers), excluding the largest and smallest values (empty gray markers, when visible). The y -axis is bounded by two standard deviations calculated for all measurements corresponding to the three crystal thicknesses. (C) Distribution of the relative Q_i shifts, with the x -axis bounded by two standard deviations calculated for all measurements.

We now turn our attention to the impact of hydrogen crystal deposition. We grow films of varying thicknesses, approximately 1, 10, and over 100 m. The thicknesses were determined using the same technique in Chapter 5. Figure 8.3(A) presents the internal quality factor measured at an average photon number of $\bar{n} \sim 10^4 \lesssim n_c$, where n_c is the critical photon number at bifurcation [94, 100]. The measurements focus on sample S with the 1 cm aperture, as this configuration allows us to systematically track the effect of crystal growth. The 1 mm aperture, in contrast, restricts gas flow, preventing significant crystal formation (as indicated by the absence of a measurable frequency

shift). Meanwhile, for sample L with the 1 cm aperture, the quasiparticle background is too high, obscuring the resonances due to excessive dissipation. To isolate quasiparticle losses as the dominant dissipation channel, we conduct measurements at the highest available power, effectively saturating dielectric loss.

The data in Figure 8.3 presented were collected across three separate cooldowns, with a new crystal grown in each cycle. The sample was characterized both before and after crystal deposition. Several notable trends emerge from the measurements. The baseline Q_i (prior to deposition) remains largely consistent, aside from a slight downward trend at higher frequencies. The two outliers with reduced Q_i may result from fabrication imperfections, a dielectric shift that moves the resonator frequency closer to a more lossy microwave environment, or increased radiative decay for resonators positioned directly beneath the aperture. However, we are unable to verify the latter hypothesis, as not all 22 fabricated resonators are visible in each sample, potentially due to fabrication-related inconsistencies.

The addition of cryogenic crystals leads to a decrease in resonant frequency, which is expected as vacuum is replaced by a dielectric medium. This frequency shift, in combination with FEM simulations, allows us to estimate the crystal thickness. Surprisingly, the internal quality factor Q_i increases following crystal deposition. From a materials science perspective, replacing vacuum with any dielectric would typically introduce additional losses rather than reduce them. As shown in Figure 8.3 (B), the enhancement of Q_i does not appear to be correlated with the frequency shift, meaning it is independent of crystal thickness. This suggests that the improvement in Q_i originates purely from a surface effect. Furthermore, Figure 8.3 (C) indicates that the most significant increase in Q_i occurs with the thinnest crystals. While the enhancement is on the order of $\lesssim 8\%$, comparable to thicker crystals, the distribution is notably sharper. This suggests that as crystal thickness increases, additional losses—likely stemming from structural defects—begin to offset the beneficial effects.

8.0.3 Theoretical model

In the context of explaining the observed improvements in the internal quality factor (Q_i) after hydrogen crystal deposition, we refer to a model that was developed and discussed in our earlier work [91]. While this model was not part of my own research for this thesis, it provides a crucial theoretical framework for understanding the mechanism behind the observed experimental results. This model, based on density functional theory (DFT) simulations, was used to investigate the microscopic interactions at the

interface between the para-hydrogen crystal and the resonators, which is thought to be the primary cause of the quality factor improvement.

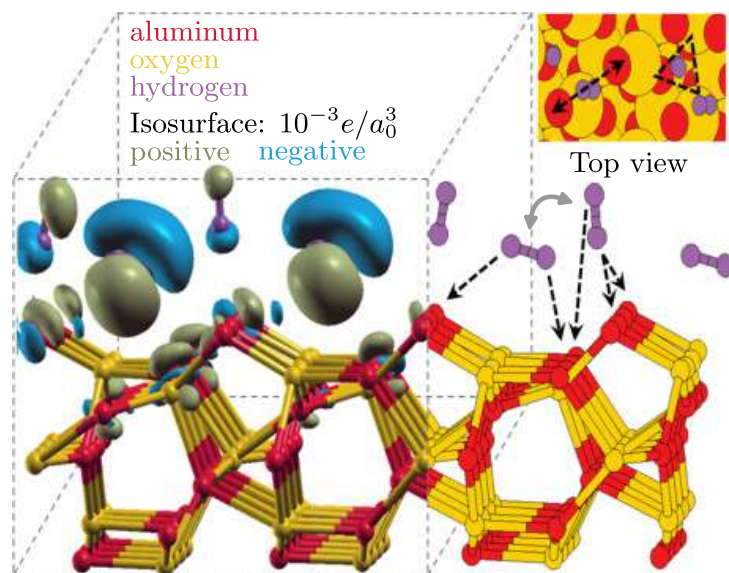


Figure 8.4 A depiction of the supercell used in the density functional theory (DFT) simulations is shown. The supercell consists of aluminum (red) and oxygen (yellow) atoms, with eight hydrogen molecules (purple) initially in a charge-neutral state. These hydrogen molecules adhere to the surface through a site-specific physisorption mechanism, which leads to either a charging or discharging effect, depending on their orientation (as indicated by the isosurface showing the charge density). The H_2 molecules adopt one of two configurations: they can be *nearly perpendicular* to the surface, with an approximate angle of 80° , or *nearly parallel*, with a roughly 15° angle to the surface. The grey double-headed arrow illustrates the ability of the hydrogen molecules to switch between these parallel and perpendicular configurations, which in turn results in a change in the dipole moment. The black dashed arrows highlight the coordination partners of hydrogen and oxygen, with the hydrogen atom at the bottom of the perpendicular configuration having two oxygen partners.

In this model, DFT simulations were performed on a simplified alumina supercell, with eight H_2 molecules interacting with the oxide surface. These molecules, being charge neutral in their para-spin isomer state, adhere to the surface in one of two configurations: perpendicular (leading to charging) or parallel (resulting in discharge). This behavior leads to a surface enriched with loosely bound dipoles, which are dynamic (flipping between parallel and perpendicular). A model can be seen in Figure 8.0.3 (A).

The enhanced dipole density at the interface increases the coupling of electromagnetic energy, especially in the low THz region, which overlaps with the spectral gap of

the resonators. This coupling primarily affects the hydrogen molecules, with energy being dissipated via rotational, translational, or vibrational motion. The latter has the potential to couple to phonons in the underlying film. The model suggests that the mechanical coupling between the hydrogen crystal, alumina, and the granular film may limit some of the energy transfer, resulting in decreased quasiparticle losses, which is crucial for the improvement in the resonator's quality factor.

While this model provides valuable insight into the mechanism at play, it is acknowledged as speculative, and further work is necessary to fully understand the mechanical coupling between the layers involved, as well as to explore other potential mechanisms for performance improvement.

Chapter 9

Outlook

9.1 Realization of a new type of hybrid quantum system

Strongly coupling alkali atoms to a superconducting resonator is a critical milestone toward integrating this technology into broader quantum systems. In addition to achieving strong coupling, we have demonstrated that depositing layers of cryogenic gas matrices onto superconducting resonators does not significantly degrade the quality factor. This finding suggests that this platform is a viable alternative to conventional host materials, potentially expanding the range of materials suitable for hybrid quantum systems.

The impurities embedded within the crystal exhibit only slight frequency shifts in the microwave regime, indicating that there is considerable room for optimization—particularly in increasing spin ensemble density (N) and reducing inhomogeneous broadening (γ). By refining these parameters, the coherence properties of the system could be further enhanced, improving its overall utility for quantum applications.

Moreover, the modular design of our experimental setup, as demonstrated by our ability to explore multiple host matrices and impurity species with relative ease, highlights the platform's adaptability. This flexibility makes it a powerful tool for investigating various quantum phenomena, from spin physics to cavity quantum electrodynamics, and suggests its potential for applications beyond those explored in this work.

9.2 Cryogenic system upgrade

If one intends to further explore cavity QED experiments or, more generally, integrate this technology with state-of-the-art superconducting qubit experiments, it would be advantageous to redesign this experiment to operate in a dilution refrigerator. As demonstrated throughout this thesis, the ADR has a limited operational lifetime at 50 mK, whereas a dilution refrigerator can maintain much lower temperatures for years in principle. The difference between working at 10 mK versus 50 mK is particularly significant for sodium, as it increases the population of the $|F, m_f\rangle = |2, 2\rangle$ state from 39% to 80%.

Furthermore, the ability to sustain 10 mK for extended periods allows for more precise single-photon measurements. If one of the primary goals of this platform is to serve as a quantum memory, then the ability to operate at the single-photon level becomes essential. The reduction in thermal noise and the ability to perform long integration times can only benefit the system.

However, utilizing a dilution refrigerator presents two primary challenges. The first is ensuring that the stage on which the crystal is grown can handle the heat load (unless the crystal is sufficiently thin) and remain at a low temperature during both the mixing and cool down phases. If the crystal warms up, impurity migration may occur, or worse, the crystal may melt. While this issue could be mitigated by using alternative host materials such as argon or krypton, it remains a nontrivial challenge.

The second challenge is the cycle time between growing a crystal, performing measurements, melting it off, and making any necessary modifications to the fridge. In contrast to the ADR, where this process takes less than 36 hours, a dilution refrigerator significantly increases turnaround time. That said, if one considers PhD students' time to be an expendable resource, this challenge becomes more of an inconvenience than a fundamental limitation.

9.3 Impurities

9.3.1 Atoms

As discussed in Chapter 3, alkali atoms provide transition frequencies that are well-suited for microwave technologies. However, further optimizing their integration could enhance the system's performance. One method is to use a single isotope, such as pure ^{87}Rb for deposition which would increase N . Another challenge is reducing clustering which would ultimately improve γ .

Other potential improvements involves optical pumping, which could further refine system performance. However, implementing circularly polarized light introduces additional experimental challenges, though it remains a viable option.

Alternatively, selecting an atom with a more favorable hyperfine structure—similar to hydrogen—could offer distinct advantages. Hydrogen’s single hyperfine ground state naturally results in an almost fully polarized ground state at 50 mK. As seen in Figure 9.1, we believe we are already coupling to atomic hydrogen. Other atoms, such as silver, exhibit comparable hyperfine properties and may provide similar benefits.

Another approach is to implant highly magnetic atoms, such as dysprosium or erbium. While alkali atoms have a magnetic moment of just one Bohr magneton, dysprosium, for example, possesses a moment of $10 \mu_B$ as well as hyperfine transitions in the GHz range for addressability. As a result, these atoms embedded in the crystal can achieve dipole-dipole couplings that are inherently 100 times stronger than those of alkali atoms. Of course this comes with its own challenges, but it is an interesting system nonetheless.

9.3.2 Sensing and metrology

Quantum sensing using nitrogen-vacancy (NV) centers in diamond has revolutionized the field by enabling exquisite sensitivity to local magnetic and electric fields [101], as well as individual nuclear spins. In experiments led by Tim Taminiau [102–104], individual nuclear spins have been addressed with remarkable precision, yet these experiments remain confined to the diamond lattice, inherently limiting their scope to intra-diamond phenomena. Moreover, NV centers must be positioned within approximately 5 nm of the diamond surface to effectively probe external signals, and the diamond surface itself is often contaminated, introducing substantial noise that further degrades sensing performance. Additionally, fabricating shallow NV centers with consistent properties remains a significant challenge, as their reproducibility is not yet at the desired level.

In contrast, Patrice Bertet and Emmanuel Flurin’s work [105–107] has demonstrated nuclear spin sensing with microwaves in bulk solids. However, as is the case for almost all sensing platforms, it might have a hard time integrating reactive foreign molecules because depositing them directly on the resonator will lead to degradation of its performance. This challenge highlights a crucial gap: while NV centers excel in highly controlled diamond environments and Bertet’s and Flurin’s resonator-based approach offers excellent sensitivity in bulk, neither platform readily accommodates the incorporation of diverse impurity species.

I propose a crystal platform that aims to overcome these limitations by providing a versatile host capable of accommodating almost any type of impurity. By implanting sensors surrounding the impurity of choice within our crystal, we can achieve significantly shorter distances between the sensor and the target, potentially enhancing sensitivity and reducing noise. In particular, using polar molecules—whose intrinsic dipole moments offer additional degrees of freedom—could enable sensor configurations analogous to Taminiau’s NV center experiments, but with the added advantage of probing external environments beyond the constraints of diamond. Our experiment has already demonstrated coupling of atomic Rb, Na, and potentially hydrogen and electrons outside of the bulk material in the cryogenic solid. As seen the Figure below, we believe we are already coupling to large ensembles of atomic hydrogen as well as electrons on the surface, or potentially lodged in the bulk.

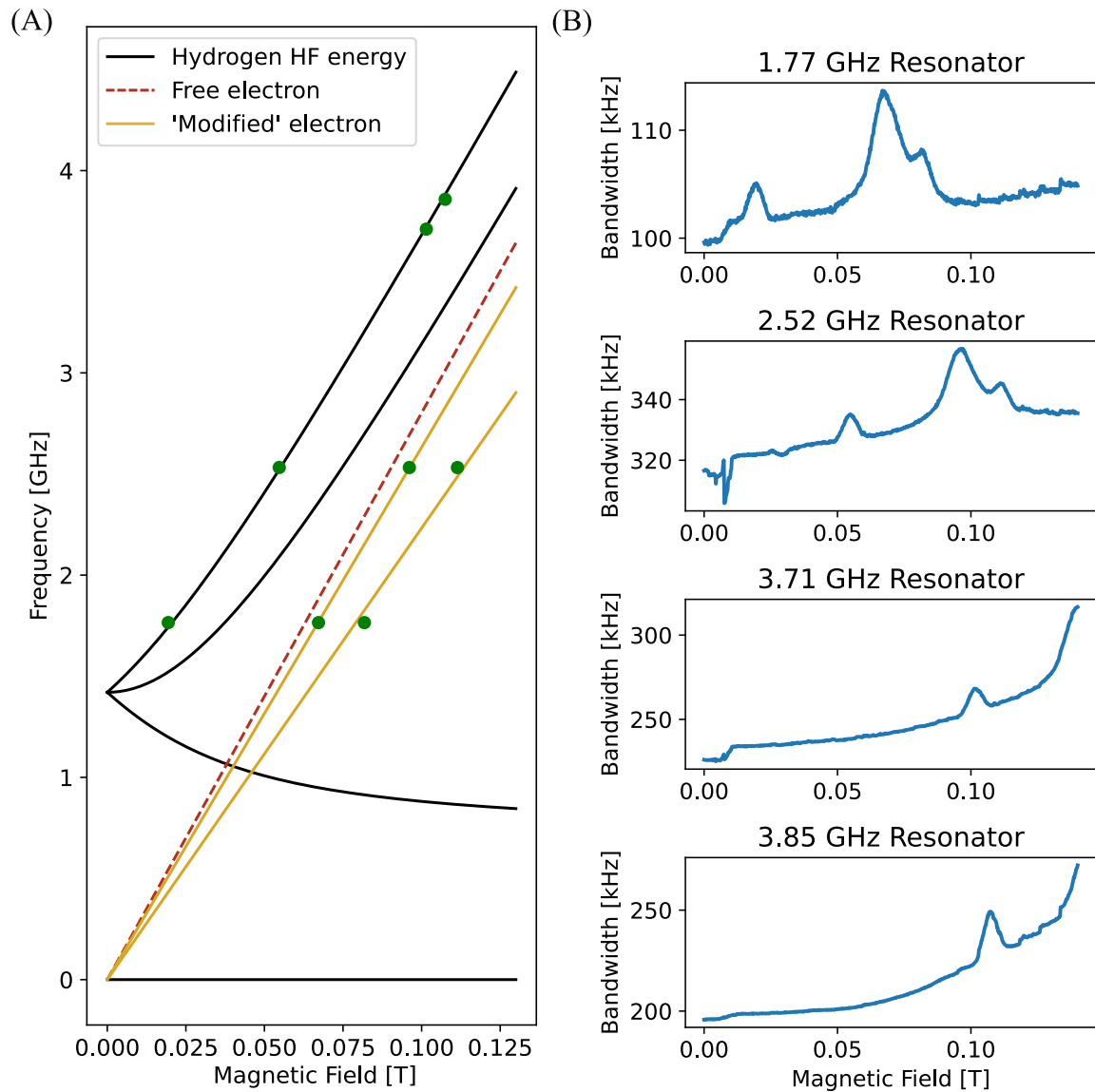


Figure 9.1 (A) Plotting of hydrogen's hyperfine transition normalized to the ground state in black. The green spots are the measured couplings from four different resonators on the same chip. We see a clear signature that atomic hydrogen exists on top or within the bulk. The gold lines indicate a linear line with no zero field splitting. The top line would have a gyromagnetic ratio $\gamma/2\pi = 26.32$ GHz/T and the lower one $\gamma/2\pi = 22.32$ GHz/T. The red dashed is the Zeeman transition energy of a free electron, where $\gamma/2\pi = 28.024$ GHz/T. (B) Fitted bandwidth of four resonators as a function of magnetic field. Peaks are green dots in LHS figure.

In this way, our approach represents a compelling synthesis of the strengths observed in both Taminiau's, Bertet's, and Flurin's experiments, paving the way for advanced quantum sensing applications.

Furthermore, one could imagine performing single spin NMR, similar to Bertet and Flurin in the microwave regime by embedding the important molecule in the cryogenic solid and reading out the nuclear spins with our superconducting resonators as seen in Figure 9.2 (B).

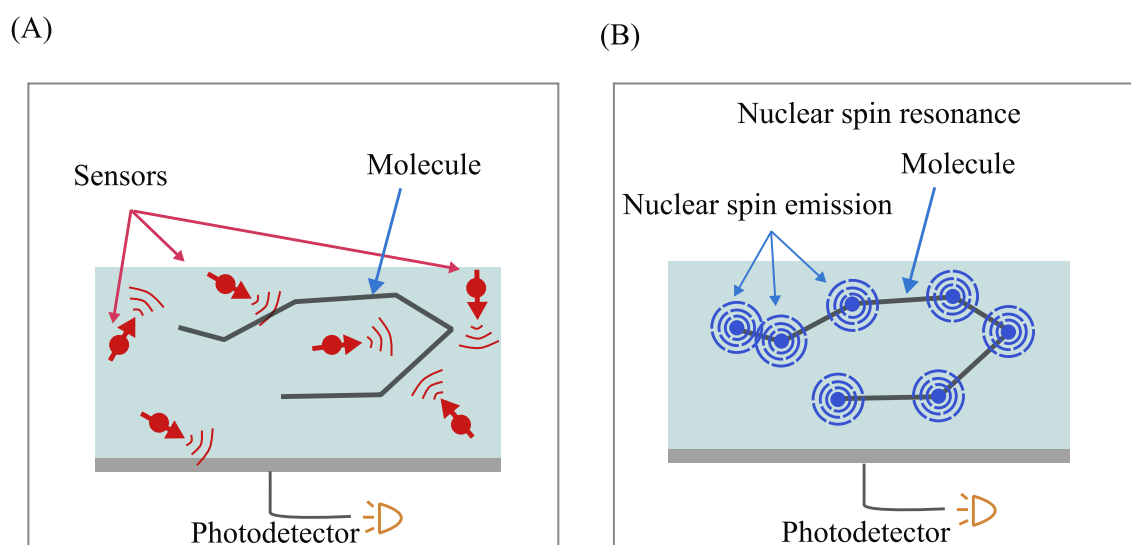


Figure 9.2 (A) Method for detecting foreign impurities: embedded atomic or molecular sensors surround the unknown species. Probing the properties of the individual sensors give insight to the local surrounds. (B) Molecule is embedded in the cryogenic matrix and nuclear spin resonance is performed.

9.3.3 Polar Molecules

In contrast to atomic impurities, molecular impurities have the potential to offer substantial technological advantages [8, 108]. One notable benefit is the ability to couple *electrically* rather than magnetically.

To highlight the difference in coupling strengths, we consider the interaction of a single dipole with a single photon in a coplanar waveguide resonator. The magnetic dipole coupling strength for a single $1/2$ spin is $\frac{28 \text{ MHz}}{\text{mT}}$. In comparison, the electric coupling strength for a single Debye is $\frac{47 \text{ kHz}}{\text{V/m}}$. For a single photon, this translates to an electrical coupling of approximately 4.7 kHz at 0.1 V/m, while the magnetic coupling

results in a much weaker 6 Hz at 2 μ G. As such, coupling electrically immediately offers a gain of nearly *one thousand times*.

In practical terms, generating high electric fields is relatively straightforward using current superconducting circuit fabrication techniques. By employing lumped-element resonators, it is possible to decrease capacitance (maximizing voltage) while increasing inductance, thereby preserving the desired resonant frequency. The relationship between energy, inductance, and capacitance is given by the equation:

$$E = \frac{1}{2}LI^2 = \frac{1}{2}CV^2$$

where $\omega = \frac{1}{\sqrt{LC}}$. The challenge lies in minimizing capacitance, which can be achieved geometrically by reducing the area of the capacitor's electrodes and the gap between them. However, this approach has limitations: as capacitance is reduced, the resonant frequency increases. To compensate for this, inductance must be increased, which can be accomplished by enlarging the footprint of the inductor or by using high kinetic inductance resonators. High kinetic inductance resonators take advantage of the properties of disordered superconductors to enhance kinetic inductance, rather than relying only on geometric inductance [109].

For a lumped-element resonator, a rough estimation suggests that a single molecule could result in a coupling of $E = 300$ V/m $\rightarrow g \sim 15$ MHz. Using kinetic inductance resonators should increase this coupling to potentially 50 MHz. Such a large coupling would be extraordinary for a single molecule and would most likely place it in the strong coupling regime, assuming the linewidth is relatively narrow.

Naturally, the question arises: which molecules and transitions can be addressed in a cryogenic solid at temperatures below 100 mK? At 100 mK, vibrational states are typically in their ground state, as these states are in the THz regime. While rotational states seem plausible, it has been shown that molecules with rotational constants below 40 GHz do not rotate in these matrices. However, there is a transition that is fundamentally quantum mechanical, regardless of temperature: the *inversion transition*.

The inversion transition, particularly in ammonia (NH₃) [110], was used in the creation of the first maser. In 1954, Charles Townes, James Gordon, and H.J. Zeiger passed a beam of energetically excited ammonia molecules into a high-Q resonant cavity at 24 GHz, causing photon emission [111]. These photons then triggered stimulated emission to the incoming molecules. This transition, or similar ones, is an ideal candidate for coupling to superconducting resonators. In the case of NH₃, the nitrogen

atom tunnels between hydrogen planes, and the energy difference between the symmetric and antisymmetric tunneling states is 23 GHz.

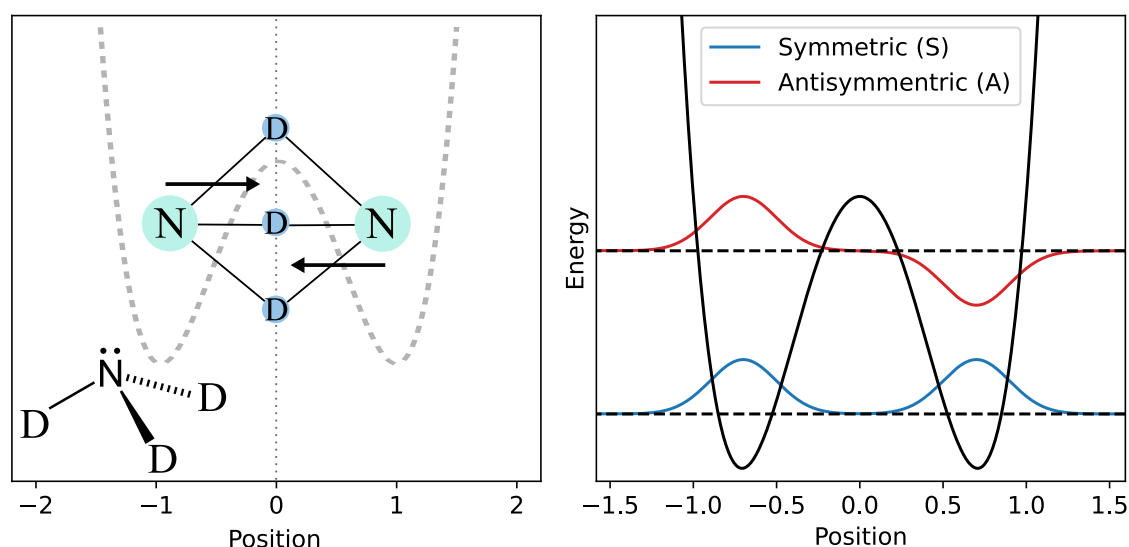


Figure 9.3 Left: Figure shows the double well potential as well as the molecular orientation of deuterated ammonia. Right: Inversion transition wavefunction, both symmetric (S) and antisymmetric (A).

Unfortunately, the transition frequency of NH_3 is higher than most microwave technologies can support. However, deuterated ammonia (ND_3) has an inversion transition at 1.6 GHz [112], and mixtures of hydrogen and deuterium fall between these two values. Furthermore, the inversion transition has been shown to exist in solid para-hydrogen, though this does not guarantee that the transition will occur. Both ammonia isotopes possess rich hyperfine structure, offering potential states for quantum memory. This enables the possibility of electrically coupling to the molecule while decoupling it magnetically—something difficult to achieve with atoms and superconducting resonators.

That said, one should remain cautiously optimistic when working with molecules, as they present additional complications. However, this represents an important first step toward single-molecule coupling to superconducting resonators.

9.4 Concluding remarks

The demonstration of strong coupling between alkali atoms embedded in a quantum solid and a microwave resonator provides compelling evidence that this platform holds great promise in quantum physics. The vast number of impurities that can be incorporated into the host matrix opens the door to a wide range of experiments, offering new insights into cavity QED, atomic–molecular–optical physics, and likely many other fields yet to be explored. Until now, impurities have primarily been addressed using optical and microwave techniques, but there remain many unexplored frequency regimes.

On a personal note, I have worked with these crystals for longer than I care to admit, and time after time I find myself brainstorming potential experiments—even though there is never enough time to perform them all. When I began my undergraduate project, only one or two groups were using these crystals as a quantum platform. Today, more than ten groups are actively engaged in this research, and I am optimistic that many more will join in the future. I hope I helped contribute, even if it was a small part.

To the next curious scientist who chooses to work with these crystals: I wish you the very best of luck and happy crystal growing! May the knowledge accumulated through my bachelor’s, master’s, and PhD work serve as a solid foundation for you to build your own experiments and to approach unexpected challenges with confidence, or at least the knowledge that you’re not the only one who struggled. And in those inevitable moments of frustration, remember to take a break—grab a cold beer, sit outside, surround yourself with good friends, and let your curiosity guide you. It worked for me, so why not you?

Ois hoib so wüd

Appendix A

Appendix

p-H₂ purity

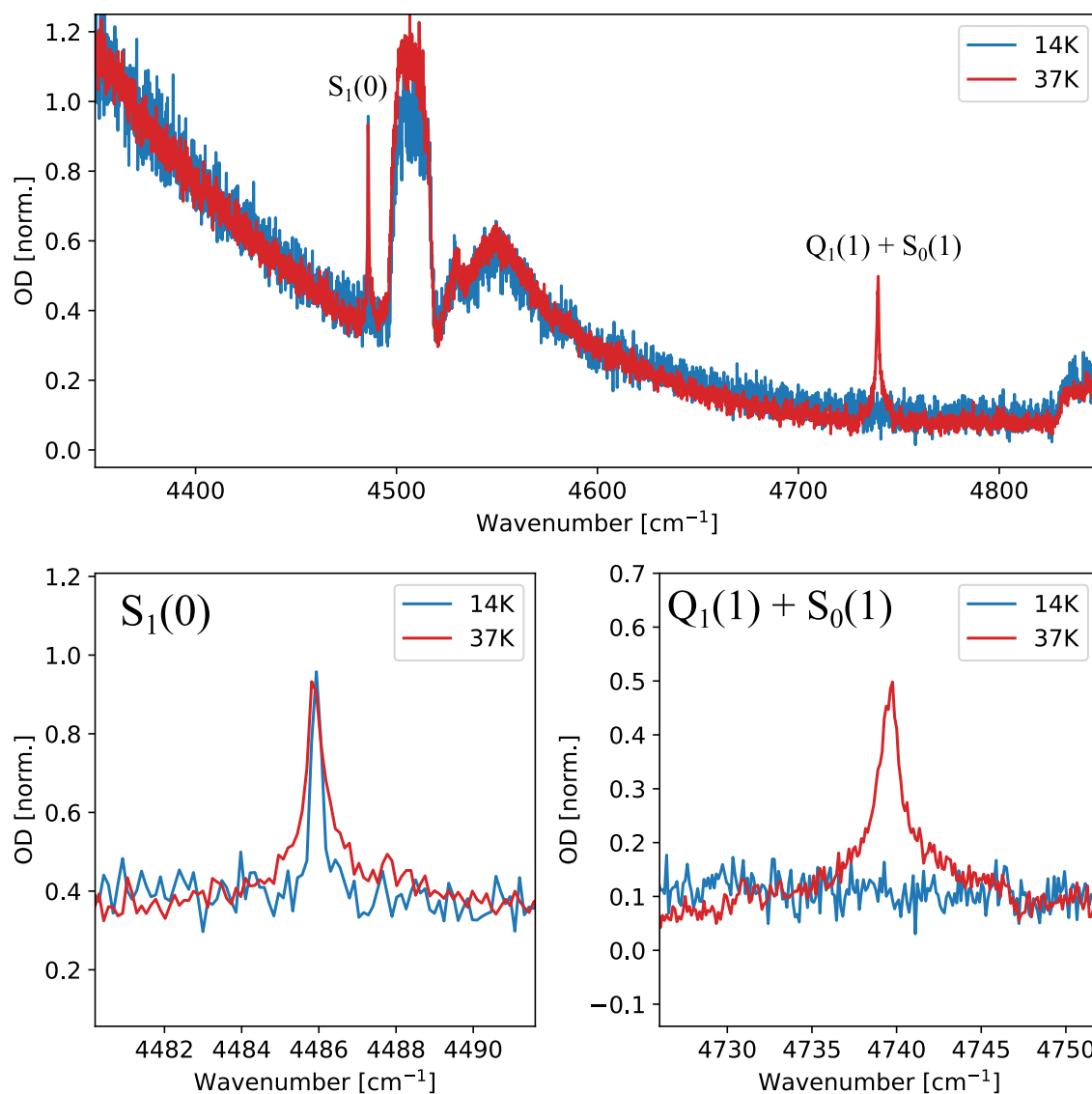


Figure 1 (Top) FTIR spectrum of solid hydrogen crystals at different catalyst temperatures. (Bottom Left) Zoomed in plot of the S₁(0) vibration transition. (Bottom Right) Zoomed in plot of the Q₁(1) + S₀(1) vibration transition. From [66], it is estimated that the 14 K para-hydrogen crystal is of purity 99.9%

Annealing

A common technique in solid-state systems is annealing, where a crystal is heated to an elevated temperature to allow atomic migration toward a lower-energy configuration. This process generally improves crystal quality. Additionally, annealing doped crystals has been shown to improve homogeneous broadening in electric and optical transitions. To this extent, one would naturally be curious about the effects of annealing on these crystals.

In Figure 2, we annealed a sodium-doped crystal at 4.8 K for one hour before gradually cooling it back to 3 K. If an increased optical density (OD) around free sodium's D1 and D2 lines indicates improved trapping sites, our results suggest the opposite. Figure 2 compares the OD of a "normal" crystal with that of the annealed sample, measured at 3 K. We further cooled the sample to 100 mK and recorded an optical spectrum. Notably, OD decreased significantly between 415–475 nm and at 587 nm, which are assumed to correspond to favorable trapping sites. Additionally, peaks in the 600–740 nm range weakened, while OD around 505 nm increased.

A microwave scan revealed minimal coupling. The reason why annealing at such a low temperature degrades both the optical and microwave spectra remains unclear. One possible explanation is that sodium atoms migrate and form clusters. Perhaps vacancies in the crystal are advantageous in maintaining the atomic properties of the impurities.

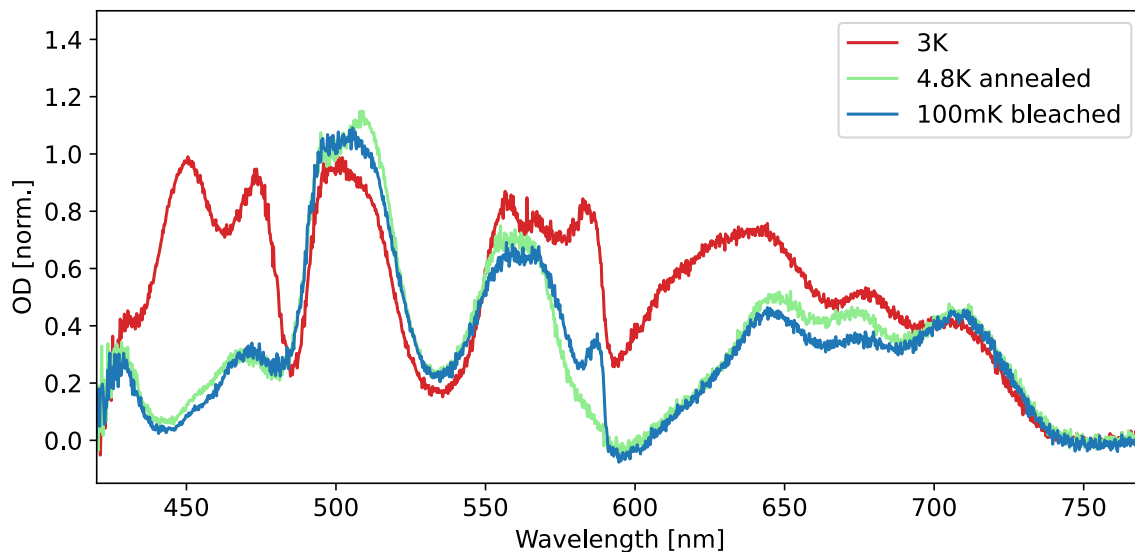


Figure 2 Three optical spectras showcasing the change in spectra over temperature and optical bleaching.

Optical bleaching at mK temperatures

Bleaching at mK temperatures has a drastic effect on the coupling between the spin ensemble and the cavity. The coupling strength of an unbleached ensemble is only $g_{UB}/(2\pi) = 428 \text{ kHz}$, which is almost 3 times lower than the coupling we achieved for the fully bleached Na ensemble ($g_{eff}/(2\pi) = 1.19 \text{ MHz}$). Hence, there is a correlation between the number of Na atoms observed in the absorption and microwave spectroscopies. This can be seen in Figure 3

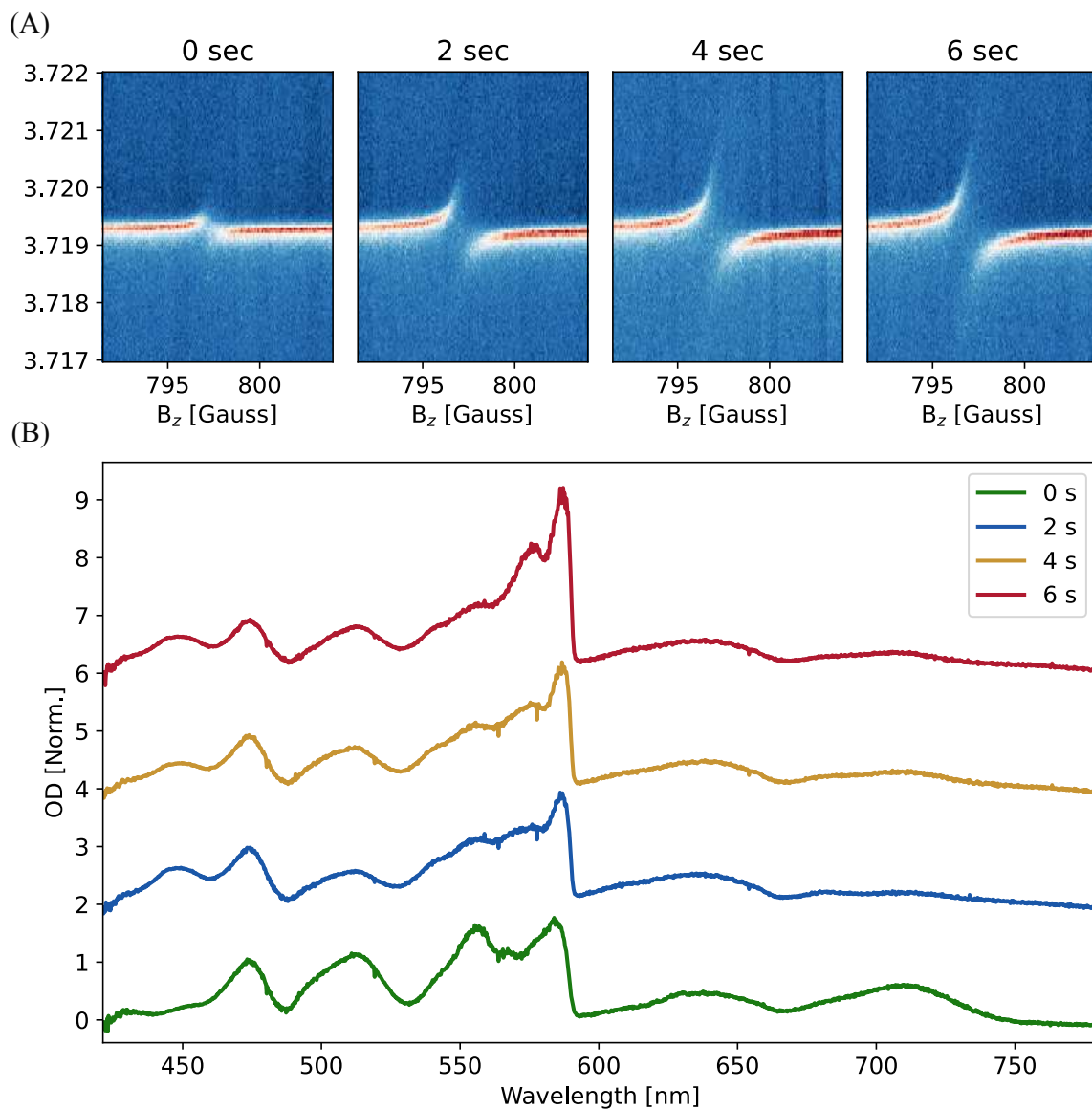


Figure 3 The crystal has two predominate trapping sites. One being a "good" trapping site which results in atoms in the optical spectrum closest to the D1/D2 line. The second are in the "bad" trapping site. When light is shined onto the atoms, they have a probability of being put into either of the trapping sites. As we cool down the system to 50 mK, the probability to end up in the "good" trapping site after optical excitation is larger. Possible explanations are due to pumping into the zero-phonon-line

We believe the increased OD between the 3 K and 50 mK is due to an increased absorption into the zero-phonon line. Similar effects have been witnessed in other solid-state systems with vacancies and impurities [34, 113]. A pictorial representation can be seen in the Figure below

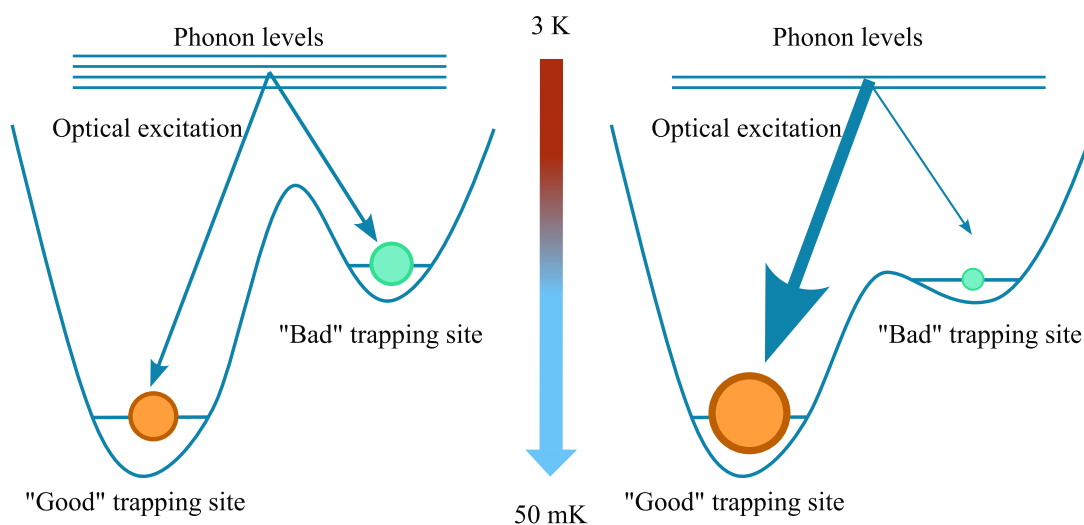


Figure 4 (A) Microwave spectroscopy as a function of integrated bleaching time. This was done using a different crystal than in Figure 7.6. As the total bleaching increases, the coupling increases. (B) OD of the bleached crystal at different integrated times. The ODs are shifted by an offset to help with visibility. As the OD at 587 nm increases, the larger the coupling is measured.

References

- [1] S. Haroche and J. M. Raimond, *Exploring the Quantum: Atoms, Cavities, and Photons*. Oxford: Oxford Univ. Press, 2006.
- [2] P. O. Schmidt, T. Rosenband, C. Langer, W. M. Itano, J. C. Bergquist, and D. J. Wineland, "Spectroscopy using quantum logic," *Science*, vol. 309, no. 5735, pp. 749–752, 2005.
- [3] A. Cao, W. J. Eckner, T. L. Yelin, A. W. Young, S. Jandura, L. Yan, K. Kim, G. Pupillo, J. Ye, N. D. Oppong, and A. M. Kaufman, "Multi-qubit gates and schrödinger cat states in an optical clock," *Nature*, vol. 634, pp. 315–320, 2024.
- [4] R. J. Thompson, G. Rempe, and H. J. Kimble, "Observation of normal-mode splitting for an atom in an optical cavity," *Physical Review Letters*, vol. 68, no. 8, pp. 1132–1135, 1992.
- [5] J. M. Raimond, M. Brune, and S. Haroche, "Strong purcell effect for a rydberg atom in a cavity," *Physical Review Letters*, vol. 49, no. 25, pp. 1924–1927, 1981.
- [6] A. Wallraff, D. I. Schuster, A. Blais, L. Frunzio, R.-S. Huang, J. Majer, S. Kumar, S. M. Girvin, and R. J. Schoelkopf, "Strong coupling of a single photon to a superconducting qubit using circuit quantum electrodynamics," *Nature*, vol. 431, pp. 162–167, 2004.
- [7] G. Kurizki, P. Bertet, Y. Kubo, K. Mølmer, D. Petrosyan, P. Rabl, and J. Schmiedmayer, "Quantum technologies with hybrid systems," *Proceedings of the National Academy of Sciences*, vol. 112, no. 13, pp. 3866–3873, 2015.
- [8] M. Wallquist, K. Hammerer, P. Rabl, M. Lukin, and P. Zoller, "Hybrid quantum devices and quantum engineering," *Physica Scripta*, vol. 137, p. 01400, 2009.
- [9] A. A. Clerk, K. W. Lehnert, P. Bertet, J. R. Petta, and Y. Nakamura, "Hybrid quantum systems with circuit quantum electrodynamics," *Nature Physics*, vol. 16, pp. 257–267, 2020.
- [10] M. Steger, K. Saeedi, M. L. W. Thewalt, J. J. L. Morton, H. Riemann, N. V. Abrosimov, P. Becker, and H.-J. Pohl, "Quantum information storage for over 180 s using donor spins in a ²⁸Si "semiconductor vacuum",", *Science*, vol. 336, no. 6086, pp. 1280–1283, 2012.
- [11] D. D. Awschalom, L. C. Bassett, A. S. Dzurak, E. L. Hu, and J. R. Petta, "Quantum spintronics: engineering and manipulating atom-like spins in semiconductors," *Science*, vol. 339, pp. 1174–1179, 2013.

- [12] N. Bar-Gill, L. M. Pham, A. Jarmola, D. Budker, and R. L. Walsworth, “Solid-state electronic spin coherence time approaching one second,” *Nature Communications*, vol. 4, 2013.
- [13] D. I. Schuster, A. P. Sears, E. Ginossar, L. DiCarlo, L. Frunzio, J. J. L. Morton, H. Wu, G. A. D. Briggs, B. B. Buckley, D. D. Awschalom, and R. J. Schoelkopf, “High-cooperativity coupling of electron-spin ensembles to superconducting cavities,” *Phys. Rev. Lett.*, vol. 105, p. 140501, Sep 2010.
- [14] S. Probst and et al., “Anisotropic rare-earth spin ensemble strongly coupled to a superconducting resonator,” *Physical Review Letters*, vol. 110, no. 15, p. 157001, 2013.
- [15] A. Imamoglu, “Cavity qed based on collective magnetic dipole coupling: Spin ensembles as hybrid two-level systems,” *Phys. Rev. Lett.*, vol. 102, p. 083602, Feb 2009.
- [16] J. Verdú, H. Zoubi, C. Koller, J. Majer, H. Ritsch, and J. Schmiedmayer, “Strong magnetic coupling of an ultracold gas to a superconducting waveguide cavity,” *Phys. Rev. Lett.*, vol. 103, p. 043603, Jul 2009.
- [17] J. V. Atanasoff, “The dielectric constant of helium,” *Phys. Rev.*, vol. 36, pp. 1232–1242, Oct 1930.
- [18] S. A. Lyon, “Spin-based quantum computing using electrons on liquid helium,” *Phys. Rev. A*, vol. 74, p. 052338, Nov 2006.
- [19] G. Koolstra, G. Yang, and D. I. Schuster, “Coupling a single electron on superfluid helium to a superconducting resonator,” *Nature Communications*, vol. 10, p. 5323, 2019.
- [20] D. E. Milligan and M. E. Jacox, “Matrix-isolation study of the reaction of atomic and molecular fluorine with carbon atoms. the infrared spectra of normal and ^{13}C -substituted CF_2 and CF_3 ,” *The Journal of Chemical Physics*, vol. 48, no. 5, pp. 2265–2271, 1968.
- [21] T. G. Carver and L. Andrews, “Matrix infrared spectrum and bonding in the dibromomethyl radical,” *The Journal of Chemical Physics*, vol. 50, no. 10, pp. 4223–4234, 1969.
- [22] C. K. Jen, V. A. Bowers, E. L. Cochran, and S. N. Foner, “Electron spin resonance of alkali atoms in inert-gas matrices,” *Physical Review*, vol. 126, no. 5, pp. 1749–1757, 1962.
- [23] C. K. Jen, S. N. Foner, E. L. Cochran, and V. A. Bowers, “Electron spin resonance of atomic and molecular free radicals trapped at liquid helium temperature,” *Physical Review*, vol. 112, no. 4, pp. 1169–1182, 1958.
- [24] S. I. Kanorsky, M. Arndt, R. Dziewior, A. Weis, and T. W. Hänsch, “Optical spectroscopy of atoms trapped in solid helium,” *Physical Review B*, vol. 49, no. 5, pp. 3645–3647, 1994.

- [25] S. I. Kanorsky, M. Arndt, R. Dziewior, A. Weis, and T. W. Hänsch, “Pressure shift and broadening of the resonance line of barium atoms in liquid helium,” *Physical Review B*, vol. 50, no. 9, pp. 6296–6302, 1994.
- [26] A. Weis, S. Kanorsky, M. Arndt, and T. W. Hänsch, “Spin physics in solid helium: Experimental results and applications,” *Zeitschrift für Physik B Condensed Matter*, vol. 98, no. 3, pp. 359–362, 1995.
- [27] A. Kanagin, S. Regmi, P. Pathak, and J. Weinstein, “Optical pumping of rubidium atoms frozen in solid argon,” *Physical Review A*, vol. 88, no. 6, p. 063404, 2013.
- [28] S. Upadhyay, U. Dargyte, R. P. Prater, V. D. Dergachev, S. A. Varganov, T. V. Tscherbul, D. Patterson, and J. D. Weinstein, “Enhanced spin coherence of rubidium atoms in solid parahydrogen,” *Physical Review B*, vol. 100, no. 2, p. 024106, 2019.
- [29] A. Rollings and J. Weinstein, “Progress towards measuring the nuclear spin coherence of molecules in solid parahydrogen,” *Bulletin of the American Physical Society*, vol. 68, 2023.
- [30] D. K. Wilson and G. Feher, “Electron spin resonance experiments on donors in silicon. iii. investigation of excited states by the application of uniaxial stress and their importance in relaxation processes,” *Phys. Rev.*, vol. 124, pp. 1068–1083, Nov 1961.
- [31] C. Tahan, M. Friesen, and R. Joynt, “Decoherence of electron spin qubits in si-based quantum computers,” *Phys. Rev. B*, vol. 66, p. 035314, Jul 2002.
- [32] E. Abe, A. M. Tyryshkin, S. Tojo, J. J. L. Morton, W. M. Witzel, A. Fujimoto, J. W. Ager, E. E. Haller, J. Isoya, S. A. Lyon, M. L. W. Thewalt, and K. M. Itoh, “Electron spin coherence of phosphorus donors in silicon: Effect of environmental nuclei,” *Physical Review B*, vol. 82, p. 121201, 2010.
- [33] M. Onizhuk, K. C. Miao, J. P. Blanton, H. Ma, C. P. Anderson, A. Bourassa, D. D. Awschalom, and G. Galli, “Probing the coherence of solid-state qubits at avoided crossings,” *PRX Quantum*, vol. 2, p. 010311, Jan 2021.
- [34] T. Iwasaki, Y. Miyamoto, T. Taniguchi, P. Siyushev, M. H. Metsch, F. Jelezko, and M. Hatano, “Tin-vacancy quantum emitters in diamond,” *Phys. Rev. Lett.*, vol. 119, p. 253601, Dec 2017.
- [35] W. Heitler and F. London, “Wechselwirkung neutraler atome und homöopolare bindung nach der quantenmechanik,” *Zeitschrift für Physik*, vol. 44, pp. 455–472, 1927.
- [36] R. Eisenschitz and F. London, “Über das verhältnis der van der waalsschen kräfte zu den homöopolaren bindungskräften,” *Z. Physik*, vol. 60, pp. 491–527, 1930.
- [37] F. London, “Zur theorie und systematik der molekularkräfte,” *Z. Physik*, vol. 63, pp. 245–279, 1930.

- [38] F. London, “The general theory of molecular forces,” *Transactions of the Faraday Society*, vol. 33, pp. 8–26, 1937.
- [39] J. D. van der Waals, *Over de continuïteit van den gas- en vloeistoestand (On the Continuity of the Gaseous and Liquid States)*. doctoral dissertation, Universiteit Leiden, 1873.
- [40] T. N. Foundation, “The nobel prize in physics 1910,” 1910. Retrieved October 9, 2008.
- [41] P. Kapitza, “Viscosity of liquid helium below the λ -point,” *Nature*, vol. 141, p. 74, 1938.
- [42] J. Allen and A. Misener, “Flow of liquid helium ii,” *Nature*, vol. 141, p. 75, 1938.
- [43] F. Pereira Dos Santos, J. Léonard, J. Wang, C. J. Barrelet, F. Perales, E. Rasel, C. S. Unnikrishnan, M. Leduc, and C. Cohen-Tannoudji, “Bose-einstein condensation of metastable helium,” *Phys. Rev. Lett.*, vol. 86, pp. 3459–3462, Apr 2001.
- [44] J. E. Lennard-Jones, “The electronic structure of some diatomic molecules,” *Transactions of the Faraday Society*, vol. 25, pp. 668–686, 1929.
- [45] P. Moroshkin, A. Hofer, S. Ulzega, and A. Weis, “Spectroscopy of atomic and molecular defects in solid ^4He using optical, microwave, radio frequency, and static magnetic and electric fields (review),” *Low Temperature Physics*, vol. 32, p. 981, nov 2006.
- [46] P. Moroshkin, A. Hofer, and A. Weis, “Atomic and molecular defects in solid ^4He ,” *Physics Reports*, vol. 469, pp. 1–57, nov 2008.
- [47] F. Stienkemeier and K. K. Lehmann, “Spectroscopy and dynamics in helium nanodroplets,” *Journal of Physics B: Atomic, Molecular and Optical Physics*, vol. 39, no. 8, p. R127, 2006.
- [48] P. Pathak, “Absorption spectrum of rubidium in a solid neon matrix,” Master’s thesis, University of Nevada, Reno, 2014.
- [49] C.-Y. Xu, S.-M. Hu, J. Singh, K. Bailey, Z.-T. Lu, P. Mueller, T. P. O’Connor, and U. Welp, “Optical excitation and decay dynamics of ytterbium atoms embedded in a solid neon matrix,” *Phys. Rev. Lett.*, vol. 107, p. 093001, Aug 2011.
- [50] D. M. Lancaster, U. Dargyte, S. Upadhyay, and J. D. Weinstein, “Radiative properties of rubidium atoms trapped in solid neon and parahydrogen,” *Physical Review A*, vol. 103, no. 5, p. 052614, 2021.
- [51] U. Dargyte, D. M. Lancaster, and J. D. Weinstein, “Optical and spin-coherence properties of rubidium atoms trapped in solid neon,” *Physical Review A*, vol. 104, no. 3, p. 032611, 2021.
- [52] D. M. Lancaster, U. Dargyte, and J. D. Weinstein, “Optical spin readout of single rubidium atoms trapped in solid neon,” *Physical Review Research*, vol. 6, no. 1, p. L012048, 2024.

- [53] T. Kanai, D. Jin, and W. Guo, “Single-electron qubits based on quantum ring states on solid neon surface,” *Phys. Rev. Lett.*, vol. 132, p. 250603, Jun 2024.
- [54] R. Lambo, C.-Y. Xu, S. T. Pratt, H. Xu, J. C. Zappala, K. G. Bailey, Z.-T. Lu, P. Mueller, T. P. O’Connor, B. B. Kamorzin, D. S. Bezrukov, Y.-Q. Xie, A. A. Buchachenko, and J. T. Singh, “High-resolution spectroscopy of neutral yb atoms in a solid ne matrix,” *Phys. Rev. A*, vol. 104, p. 062809, Dec 2021.
- [55] R. Lambo, G. Koyanagi, M. Horbatsch, R. Fournier, and E. Hessels, “Calculation of the local environment of a barium monofluoride molecule in a neon matrix,” *Molecular Physics*, vol. 121, no. 22, p. e2232051, 2023.
- [56] W. Weyhmann and F. M. Pipkin, “Optical absorption spectra of alkali atoms in rare-gas matrices,” *Physical Review*, vol. 137, no. 2A, pp. 74–79, 1965.
- [57] S. Kupferman and F. Pipkin, “Properties of rubidium atoms trapped in a solid argon matrix,” *Physical Review*, vol. 166, no. 2, pp. 207–218, 1968.
- [58] S. Upadhyay, A. N. Kanagin, C. Hartzell, T. Christy, W. P. Arnott, T. Momose, D. Patterson, and J. D. Weinstein, “Longitudinal spin relaxation of optically pumped rubidium atoms in solid parahydrogen,” *Physical Review Letters*, vol. 117, no. 17, p. 175301, 2016.
- [59] G. K. Koyanagi, R. L. Lambo, A. Ragyanszki, R. Fournier, M. Horbatsch, E. Hessels, and E. collaboration, “Accurate calculation of the interaction of a barium monofluoride molecule with an argon atom: A step towards using matrix isolation of baf for determining the electron electric dipole moment,” *Journal of Molecular Spectroscopy*, vol. 391, p. 111736, 2023.
- [60] M. Ryan, M. Collier, P. de Pujo, C. Crépin, and J. McCaffrey, “Investigations of the optical spectroscopy of atomic sodium isolated in solid argon and krypton: experiments and simulations,” *J Phys Chem A*, vol. 114, no. 9, pp. 3011–3024, 2010.
- [61] M. Guarise, “Particle detection in rare gas solid crystals: a feasibility experimental study—exploring new ways for dark matter searches,” *Eur. Phys. J. Plus*, vol. 137, 2022.
- [62] B. Mong *et al.*, “Spectroscopy of ba and ba+ deposits in solid xenon for barium tagging in nexo,” *Phys. Rev. A*, vol. 91, no. 2, p. 022505, 2015.
- [63] S. Al Kharusi and nEXO Collaboration, “nexo pre-conceptual design report,” *arXiv:1805.11142*, 2018.
- [64] nEXO Collaboration, “Imaging individual barium atoms in solid xenon for barium tagging in nexo,” *Nature*, vol. 569, pp. 203–207, 2019.
- [65] I. F. Silvera, “The solid molecular hydrogens in the condensed phase: Fundamentals and static properties,” *Reviews of Modern Physics*, vol. 52, pp. 393–452, Apr. 1980.
- [66] A. N. Kanagin, “Creation and analysis of para-hydrogen crystals,” 2015.

- [67] C. Cazorla and J. Boronat, “Simulation and understanding of atomic and molecular quantum crystals,” *Rev. Mod. Phys.*, vol. 89, p. 035003, Aug 2017.
- [68] J. Verdú and et al., “Strong magnetic coupling of an ultracold gas to a superconducting waveguide cavity,” *Physical Review Letters*, vol. 103, no. 4, p. 043603, 2009.
- [69] D. A. Steck, “Rubidium 85 d line data.” <http://steck.us/alkalidata>. Version 2.3.3, last revised 28 May 2024.
- [70] D. A. Steck, “Rubidium 87 d line data.” <http://steck.us/alkalidata>. Version 2.3.3, last revised 28 May 2024.
- [71] D. A. Steck, “Sodium d line data.” <http://steck.us/alkalidata>, 2024. Last revised 28 May 2024.
- [72] L. W. Anderson, F. M. Pipkin, and J. C. Baird, “Hyperfine structure of hydrogen, deuterium, and tritium,” *Phys. Rev.*, vol. 120, pp. 1279–1289, Nov 1960.
- [73] E. T. Jaynes and F. W. Cummings, “Comparison of quantum and semiclassical radiation theories with application to the beam maser,” *Proceedings of the IEEE*, vol. 51, no. 1, pp. 89–109, 1963.
- [74] A. N. Kanagin, “Design and modeling of a cryogenic system for circuit qed experiments,” Master’s thesis, 2018.
- [75] M. Kjaergaard, M. E. Schwartz, J. Braumüller, P. Krantz, J. I.-J. Wang, S. Gustavsson, and W. D. Oliver, “Superconducting qubits: Current state of play,” *Annual Review of Condensed Matter Physics*, vol. 11, pp. 369–395, 2020.
- [76] G. Q. AI and Collaborators, “Quantum error correction below the surface code threshold,” *Nature*, vol. 638, pp. 920–926, 2025.
- [77] A. V. Dixit, S. Chakram, K. He, A. Agrawal, R. K. Naik, D. I. Schuster, and A. Chou, “Searching for dark matter with a superconducting qubit,” *Phys. Rev. Lett.*, vol. 126, p. 141302, Apr 2021.
- [78] S. Weichselbaumer, P. Natzkin, C. W. Zollitsch, M. Weiler, R. Gross, and H. Huebl, “Quantitative modeling of superconducting planar resonators for electron spin resonance,” *Phys. Rev. Appl.*, vol. 12, p. 024021, Aug 2019.
- [79] J. H. Constable, C. F. Clark, and J. R. Gaines, “The dielectric constant of h_2 , d_2 , and hd in the condensed phases,” *Journal of Low Temperature Physics*, vol. 21, pp. 599–617, 1975.
- [80] M. W. Cole and M. H. Cohen, “Image-potential-induced surface bands in insulators,” *Phys. Rev. Lett.*, vol. 23, pp. 1238–1241, Nov 1969.
- [81] U. Dargyte, *Optical and spin coherence properties of Rb atoms in solid neon for magnetic field sensing*. PhD thesis, PhD Thesis, University of XYZ, aug 2023.
- [82] E. M. Purcell, H. C. Torrey, and R. V. Pound, “Resonance absorption by nuclear magnetic moments in a solid,” *Physical Review*, vol. 69, no. 1, pp. 37–38, 1946.

- [83] F. Bloch, “Nuclear induction,” *Physical Review*, vol. 70, no. 4, pp. 460–474, 1946.
- [84] E. L. Hahn, “Spin echoes,” *Phys. Rev.*, vol. 80, pp. 580–594, Nov 1950.
- [85] H. Y. Carr and E. M. Purcell, “Effects of diffusion on free precession in nuclear magnetic resonance experiments,” *Physical Review*, vol. 94, no. 3, pp. 630–638, 1954.
- [86] S. Meiboom and D. Gill, “Modified spin-echo method for measuring nuclear relaxation times,” *Review of Scientific Instruments*, vol. 29, no. 8, pp. 688–691, 1958.
- [87] T. Astner, *Spin physics and cavity-QED with nitrogen vacancy centres in diamond*. PhD thesis, Technische Universität Wien, 2019.
- [88] A. Bienfait, J. Pla, Y. Kubo, X. Zhou, M. Stern, C. Lo, C. Weis, T. Schenkel, D. Vion, D. Esteve, *et al.*, “Controlling spin relaxation with a cavity,” *Nature*, vol. 531, no. 7592, pp. 74–77, 2016.
- [89] V. Ranjan, S. Probst, B. Albanese, A. Doll, O. Jacquot, E. Flurin, R. Heeres, D. Vion, D. Esteve, J. Morton, *et al.*, “Pulsed electron spin resonance spectroscopy in the purcell regime,” *Journal of Magnetic Resonance*, vol. 310, p. 106662, 2020.
- [90] J. Choi, S. Choi, G. Kucsko, P. C. Maurer, B. J. Shields, H. Sumiya, S. Onoda, J. Isoya, E. Demler, F. Jelezko, N. Y. Yao, and M. D. Lukin, “Depolarization dynamics in a strongly interacting solid-state spin ensemble,” *Phys. Rev. Lett.*, vol. 118, p. 093601, Mar 2017.
- [91] F. Valenti, A. N. Kanagin, A. Angerer, L. Buimaga-Iarinca, C. Morari, J. Schmiedmayer, and I. M. Pop, “Hydrogen crystals reduce dissipation in superconducting resonators,” *Phys. Rev. B*, vol. 109, p. 054503, Feb 2024.
- [92] D. Hilbert, “Über die stetige Abbildung einer Linie auf ein Flächenstück,” *Mathematische Annalen*, vol. 38, no. 3, pp. 459–460, 1891.
- [93] M. Rösch, Development of lumped element kinetic inductance detectors for mm-wave astronomy at the IRAM 30 m telescope. PhD thesis, Karlsruhe Institute of Technology, Karlsruhe, Germany, 2014.
- [94] F. Valenti, F. Henriques, G. Catelani, N. Maleeva, L. Grünhaupt, U. von Lüpke, S. T. Skacel, P. Winkel, A. Bilmes, A. V. Ustinov, *et al.*, “Interplay between kinetic inductance, nonlinearity, and quasiparticle dynamics in granular aluminum microwave kinetic inductance detectors,” *Phys. Rev. Applied*, vol. 11, p. 054087, May 2019.
- [95] “Qkit: a quantum measurement suite in Python.” <https://github.com/qkitgroup/qkit>.
- [96] S. Probst, F. B. Song, P. A. Bushev, A. V. Ustinov, and M. Weides, “Efficient and robust analysis of complex scattering data under noise in microwave resonators,” *Review of Scientific Instruments*, vol. 86, no. 2, p. 024706, 2015.

- [97] S. Hunklinger, W. Arnold, S. Stein, R. Nava, and K. Dransfeld, “Saturation of the ultrasonic absorption in vitreous silica at low temperatures,” *Physics Letters A*, vol. 42, no. 3, pp. 253 – 255, 1972.
- [98] B. Golding, J. E. Graebner, B. I. Halperin, and R. J. Schutz, “Nonlinear phonon propagation in fused silica below 1 K,” *Physical Review Letters*, vol. 30, no. 6, p. 223, 1973.
- [99] L. Grünhaupt, N. Maleeva, S. T. Skacel, M. Calvo, F. Levy-Bertrand, A. V. Ustinov, H. Rotzinger, A. Monfardini, G. Catelani, and I. M. Pop, “Loss mechanisms and quasiparticle dynamics in superconducting microwave resonators made of thin-film granular aluminum,” *Phys. Rev. Lett.*, vol. 121, p. 117001, Sep 2018.
- [100] C. Eichler and A. Wallraff, “Controlling the dynamic range of a josephson parametric amplifier,” *EPJ Quantum Technology*, vol. 1, no. 1, p. 2, 2014.
- [101] C. L. Degen, F. Reinhard, and P. Cappellaro, “Quantum sensing,” *Rev. Mod. Phys.*, vol. 89, p. 035002, Jul 2017.
- [102] M. H. Abobeih, J. Randall, C. E. Bradley, H. P. Bartling, M. A. Bakker, M. J. Degen, M. Markham, D. J. Twitchen, and T. H. Taminiau, “Atomic-scale imaging of a 27-nuclear-spin cluster using a quantum sensor,” *Nature*, vol. 576, pp. 411–415, 2019.
- [103] C. E. Bradley, J. Randall, M. H. Abobeih, R. C. Berrevoets, M. J. Degen, M. A. Bakker, M. Markham, D. J. Twitchen, and T. H. Taminiau, “A ten-qubit solid-state spin register with quantum memory up to one minute,” *Phys. Rev. X*, vol. 9, p. 031045, Sep 2019.
- [104] G. L. van de Stolpe, D. P. Kwiatkowski, C. E. Bradley, J. Randall, M. H. Abobeih, S. A. Breitweiser, L. C. Bassett, M. Markham, D. J. Twitchen, and T. H. Taminiau, “Mapping a 50-spin-qubit network through correlated sensing,” *Nature Communications*, vol. 15, 2024.
- [105] E. Albertinale, L. Balembois, E. Billaud, V. Ranjan, D. Flanigan, T. Schenkel, D. Estève, D. Vion, P. Bertet, and E. Flurin, “Coherent manipulation of quantum bits in a superconducting circuit,” *Nature*, vol. 600, pp. 434–438, 2021.
- [106] J. O’Sullivan, J. Travesedo, L. Pallegoix, Z. W. Huang, A. May, B. Yavkin, P. Hogan, S. Lin, R. Liu, T. Chaneliere, S. Bertaina, P. Goldner, D. Esteve, D. Vion, P. Abgrall, P. Bertet, and E. Flurin, “Individual solid-state nuclear spin qubits with coherence exceeding seconds,” *arXiv preprint*, oct 2024. arXiv:2410.10432.
- [107] Z. Wang, L. Balembois, M. Rančić, E. Billaud, M. L. Dantec, A. Ferrier, P. Goldner, S. Bertaina, T. Chanelière, D. Esteve, D. Vion, P. Bertet, and E. Flurin, “Single-electron spin resonance detection by microwave photon counting,” *Nature*, vol. 619, pp. 276–281, 2023.
- [108] D. DeMille, “Quantum computation with trapped polar molecules,” *Phys. Rev. Lett.*, vol. 88, p. 067901, Jan 2002.

- [109] N. Samkharadze, A. Bruno, P. Scarlino, G. Zheng, D. P. DiVincenzo, L. DiCarlo, and L. M. K. Vandersypen, “High-kinetic-inductance superconducting nanowire resonators for circuit qed in a magnetic field,” *Phys. Rev. Appl.*, vol. 5, p. 044004, Apr 2016.
- [110] C. H. Townes, “The ammonia spectrum and line shapes near 1.25-cm wave-length,” *Phys. Rev.*, vol. 70, pp. 665–671, Nov 1946.
- [111] J. P. Gordon, H. J. Zeiger, and C. H. Townes, “Molecular microwave oscillator and new hyperfine structure in the microwave spectrum of nh_3 ,” *Phys. Rev.*, vol. 95, pp. 282–284, Jul 1954.
- [112] G. Erlandsson and W. Gordy, “Submillimeter wave spectroscopy: Rotation-inversion transitions in nd_3 ,” *Phys. Rev.*, vol. 106, pp. 513–515, May 1957.
- [113] Z. Zhang, H. F. Wen, Z. Gao, Y. Liu, B. Cao, H. Guo, Z. Li, Z. Ma, X. Li, J. Tang, and J. Liu, “Investigation of zero-phonon line characteristics in ensemble nitrogen-vacancy centers at 1.6 k–300 k,” *Optics Express*, vol. 32, no. 10, pp. 17336–17344, 2024.

Curriculum Vitae

Personal Data

Name: Andrew Niels Kanagin
Date of Birth: [REDACTED]
Place of Birth: [REDACTED]
E-mail: ankanagin@gmail.com

Academic Education

Technische Universität Wien

Doctoral Studies in Technical Physics

2018 – present *Hybrid Quantum Systems* — Prof. Jörg Schmiedmayer
 Atominstitut (Vienna, Austria)

University of Nevada, Reno

2018 Master of Science in Physics

2014 Bachelor of Science in Physics

Acknowledgements

I will take this opportunity to thank quite a few people who helped me throughout my life here in Vienna. If I happen to miss someone, it was not done intentionally, I promise.

There is no one I would like to thank more than Jörg Schmiedmayer. You took a chance on me, a student from the middle of the desert, and not only provided a wonderful work environment but also offered me the opportunity to work on a truly remarkable project. Your passion for science—beyond just physics—is truly infectious. I’ve experienced a full PhD journey here in Vienna. Beyond the academic and scientific realms, you shared with me your love for culture and the city of Vienna. Since arriving, I’ve attended over 20 operas and ballets, and visited the Musikverein more than 40 times. I have seen more works of art in museums over the past 6 years than I could have ever imagined. You not only suggested, but passionately embraced engaging in these type of places. From BBQing at your place to discussing politics, it was always a pleasure. Because of you, I have become a more well-rounded person, and I can’t express enough how deeply grateful I am.

Thank you Professor Fedor Jelezko for being on my committee. Over the past 6 years I have religiously scanned your papers, found you on the arXiv, and attended conferences where you and your students presented work. The spirit of your work is of course in my PhD.

Thank you Professor Andrew Briggs for being on my committee. I first met you during my first year in Europe in both Obergurgl and in Vienna. During this time, we had a conversation in the U Bahn where you told me that eventually students will become obsolete because AI will take care of the measurements. This stuck with me my entire PhD, and I am glad I was able to finish it before I become obsolete!

Thank you, Andreas Angerer—truly. From the moment I arrived in Vienna, it was clear that you and I would be working together on my project, and I couldn’t have asked for a better partner. Over the past four years, we designed, built, and carried out incredible experiments—from nothing to something. I wish there were some form of recognition for postdocs who excel in both experimental and theoretical physics because

you are more than deserving of it. You had the foresight to identify the most important problems and, more importantly, the ability to devise quick yet effective solutions. I deeply appreciated your honesty and lack of ego when discussing physics—it was always about the truth, and I never hesitated to ask you a question. Furthermore, with no hesitation, you shared your culture and passions outside of physics with me. I look back fondly on our time together, both in the lab and beyond. Besides Jörg, there's no one in our group I'd like to thank more than you. *Steirerblut ist kein Himbeersaft!*

Thomas Astner, you were the first person to greet me at ATI, my first introduction to the Schmiedmayer group. Thank you for all of the times we spent laughing and complaining about everything and nothing, keeping tabs on each other while we went our separate ways, and of course cooking together. *Keep up the flag!*

To Wenzel Kersten, thank you for all of the laughs and drinks over the years. It was you and I in the trenches of the cryogenic group for the longest time, my brother-in-arms. I think you have a creative and unique way of tackling problems, which certainly helped me from time to time in the lab. Whenever I think of something truly Viennese, I always think of you! *Wien bleibt Wien!*

Thank you Nikolaus de Zordo for all of the fun times we have had at ATI and outside. We could not have asked for a better student to enter the cryo group, a natural fit. I really enjoyed getting to know you when we went on our American road trip, from Chicago to San Francisco! It was my turn to show you my home. Thank you for attending my hockey games and for the many beers shared. I hope my playing wasn't too bad. Danke! I look forward to see what you do with the molecular setup and beyond. *Stay gold Niki!*

Thank you Elena Redchenko for your constant positivity in our group and your microwave expertise! You're now the proud guardian of Brunhilde—treat her well, whisper sweet calibrations to her, and may she reward you with beautiful data and minimal cooldown errors. She's been my trusty companion, and I know she's in the best hands. Wishing you many resonant successes and joyful cryogenic adventures ahead!

Thank you to Ioan Pop and Francesco Valenti, who over the course of my PhD helped bring back some normalcy as a result of COVID-19. We were able to still do science while being bunkered at home. And an additional thanks to Francesco for inviting me to his family's home and introducing me to his life. There are few people that call me Drew, and you are one!

Thank you Chen for all the laughs and taking me at 3 am to Neusiedlsee in order to complete a triathlon! Thank you Qi for all the laughs and discussions about our

countries. Thank you Igor for all of the optimistic discussions about life and the state of the world. The future looks bright, so best bring some sunglasses. Thank you Marine for including me into the Schmiedmayer group so quickly and always providing a good conversation. This goes double for the kind hearted and free spirited Fedé! Similarly, thank you Filippo for all of the laughs you brought to ATI! Welcome back to Europe.

Thank you Camille, my French comrade, for all of the times we spent together, whether with a beer or out in the Prater. The day is always better when I see you. I hope to one day read Elio's thesis. Thanks for all the good times Tian Tian, Pra, Rugway, and Philipp. To my office mate Sebastian, thank you for all of the times we spoke, laughed, and just listened to music. You are an incredible person. Both you and Jeanne feel like family away from home.

To my BBQing partner in crime, Stephan Schneider. Thank you for making ATI a home, and I mean that quite endearingly. You and I have cooked, cleaned, laughed, and drank countless times at ATI that it made being there feel like a home, rather than a work place. You will always be welcome at my table, no matter the place or situation.

A special thanks to Frederik. We came in at the exact same time and have always been connected as such. You and I have gone on so many adventures together that I could not have imagined a better friend to do it with.

A very personal thank you to Mohammadamin Tajik and João Sabino. You two are my closest friends here in Europe and I can't thank you enough for helping me get through my hard days and enjoying my good ones. Both of you have introduced me into your lives, including family and home, so that I never felt too far from mine. We went on plenty of adventures together both in Europe and in the US. I am forever better because of you two. Thank you. To Barbara, Britta, and Evgeniya, thank you for every single time you got me out of trouble, whether it be with MA35 or any other Austrian bureaucracy that is beyond me. You three are the heart and core of ATI and it would not be the same without you.

As an experimentalist, you quickly learn that it is best to have the machine shop on your side. I thank them for all of their efforts towards the success of my experiment. Brunhilde was built by us!

To the portiers, thank you for always welcoming me with a smile on your face. I know I am a big, bearded, loud, American and that would not typically vibe with the Austrian mindset, but I am glad it did with you. Thank you for being part of the ATI family.

I would like to thank the Atominstitut (ATI). This is a magical place and I would like for people to know how special it is. There are close to 200 people working at the institute, I think, and yet I feel like I know them all. Being far away from downtown Vienna gives us a unique place where we were able to BBQ, host parties, perform spectacular research, and make friends. I have been to many physics departments, and there never seems to be one that has the charm, warmth, and uniqueness of ATI. It was my home.

Danke Brunhilde, my cryostat. Without any hiccups, you produced wonderful results. You were my creation and, in my opinion, you over-achieved.

Thank you Tim Taminiau for allowing me to work in your group for 3 months as part of my PhD. I absolutely love your research, as well as the wonderful environment you provided me. Additionally, thank you to Benjamain and Kai for helping throughout my time in Delft. An additional thank you to Hans who I had many discussions with!

To my dice rolling crew, thank you Kjeld, Sam, Daniel, Thomas, Frederik, and Marion. Whether it is hanging out, traveling to God who knows where, I am blessed that I am included in your group. You made the time here wonderful. I am looking to many more adventures, real and on the table.

Outside of physics, I would like to thank my hockey team. Danke Bruddas! Getting convinced to get back into playing hockey, which was easily done by George Arnold, was one of the best things that I have done, and it is with no small part because of you. I know I will always have a place in the locker room so long as you are there. Totonka!

To someone who was an important part of my life, thank for the lessons, support, and moments that helped shape who I am today.

I would like to thank my best friends Carlo and James for always supporting me from high school to the end of my PhD. I love you guys. Thank you to Bruce, Sam, Ryan, and James as well. I too love you all!

Finally, I would like to thank my family. I can't begin to express just how important the support you provided me with was. Completing a PhD has a lot of ups and downs, but it never seemed to matter as long as you are in my life. I love you Alexander, Louie, Celena, Iroh, Cammie, and the ones coming up. Not a single day goes by where I do not think about all of you.

Ma and Pa, I dedicate this to you. Words cannot express how deeply I appreciate you two. Your love and support have been the one constant throughout my life. It has been the foundation of everything I have achieved and will achieve.

I love you, always.